SAND REPORT

SAND2003-3651
Unlimited Release
Printed October 2003

Hydrostatic, Uniaxial, and Triaxial Compression Tests on Unpoled "Chem-prep" PZT 95/5-2Nb Ceramic Within Temperature Range of –55 to 75°C

Moo Y. Lee, Stephen T. Montgomery, John H. Hofer, David H. Zeuch

Prepared by
Sandia National Laboratories
Albuquerque, New Mexico 87185 and Livermore, California 94550

Sandia is a multiprogram laboratory operated by Sandia Corporation, a Lockheed Martin Company, for the United States Department of Energy under Contract DE-AC04-94AL85000.

Issued by Sandia National Laboratories, operated for the United States Department of Energy by Sandia Corporation.

Available to DOE and DOE contractors from
U.S. Department of Energy
Office of Scientific and Technical Information
P.O. Box 62
Oak Ridge, TN 37831

Telephone: (865)576-8401
Facsimile: (865)576-5728
E-Mail: reports@adonis.osti.gov
Online ordering: http://www.doe.gov/bridge

Available to the public from
U.S. Department of Commerce
National Technical Information Service
5285 Port Royal Rd
Springfield, VA 22161

Telephone: (800)553-6847
Facsimile: (703)605-6900
E-Mail: orders@ntis.fedworld.gov
Online order: http://www.ntis.gov/ordering.htm

SAND 2003-3651
Unlimited Release
Printed October 2003

Hydrostatic, Uniaxial, and Triaxial Compression Tests on Unpoled "Chem-prep" PZT 95/5-2Nb Ceramic Within Temperature Range of –55 to 75°C

Moo Y. Lee
Geomechanics Department

Stephen T. Montgomery
Neutron Generator Department

John H. Hofer
Geomechanics Department

David H. Zeuch
Systems Analysis I Department

Sandia National Laboratories
P.O. Box 5800
Albuquerque, NM 87185-0751

ABSTRACT

Sandia is currently developing a lead-zirconate-titanate ceramic 95/5-2Nb (or PNZT) from chemically prepared ("chem-prep") precursor powders. Previous PNZT ceramic was fabricated from the powders prepared using a "mixed-oxide" process. The specimens of unpoled PNZT ceramic from batch HF803 were tested under hydrostatic, uniaxial, and constant stress difference loading conditions within the temperature range of -55 to 75°C and pressures to 500 MPa. The objective of this experimental study was to obtain mechanical properties and phase relationships so that the grain-scale modeling effort can develop and test its models and codes using realistic parameters. The stress-strain behavior of "chem-prep"

PNZT under different loading paths was found to be similar to that of "mixed-oxide" PNZT. The phase transformation from ferroelectric to antiferroelectric occurs in unpoled ceramic with abrupt increase in volumetric strain of about 0.7 % when the maximum compressive stress, regardless of loading paths, equals the hydrostatic pressure at which the transformation otherwise takes place. The stress-volumetric strain relationship of the ceramic undergoing a phase transformation was analyzed quantitatively using a linear regression analysis. The pressure (P_{T1}^{H}) required for the onset of phase transformation with respect to temperature is represented by the best-fit line, P_{T1}^{H} (MPa) = 227 + 0.76 T (°C). We also confirmed that increasing shear stress lowers the mean stress and the volumetric strain required to trigger phase transformation. At the lower bound (-55°C) of the tested temperature range, the phase transformation is permanent and irreversible. However, at the upper bound (75°C), the phase transformation is completely reversible as the stress causing phase transformation is removed.

ACKNOWLEDGEMENTS

The authors would like to acknowledge Rebecca Brannon and David Holcomb for their critical review of this report. The authors also thank Jeffrey Keck for overseeing fabrication of the PNZT specimens. Diane Meier assisted in the preparation of the specimens and Robert Hardy provided advice in setting up the control system for the loading machine. The managerial support received from Jaime L. Moya, Justine E. Johannes and Laurence S. Costin is also gratefully appreciated.

Table of Contents

Figures

Tables

1. Introduction

Sandia is currently developing a new PNZT ceramic sintered from a chemically precipitated, calcined and agglomerated powder (Voigt *et al*. 1998; Voigt *et al*. 1999). Lead-zirconate-titanate 95/5-2Nb ceramic (PZT 95/5-2Nb, or, simply, "PNZT") is the active electrical element in ferroelectric explosive power supplies (Lysne and Percival, 1975; Bauer *et al*., 1989). Under explosive loading, poled ferroelectric (FE) PNZT transforms to an antiferroelectric (AFE) polymorph, rapidly releasing its bound surface charge and producing very large voltages and currents (Fritz and Keck, 1978). Thus, the electromechanical response of PNZT must be understood and modeled under complex, dynamic loading conditions.

The ASCI (Advanced Simulation and Computing Program) Project "Grain-Scale Shock Response of PZT 95/5-2Nb Ceramic" is developing microstructural-scale models and codes (Brannon *et al*., 2001) to accomplish this goal. Currently, the grain-scale modeling effort is working almost exclusively with phase relationships and electromechanical properties that have been measured for PNZT fabricated using a "mixed-oxide" process, in which lead, zirconium, titanium and niobium oxide powders were mixed, calcined, milled and agglomerated; the resulting PNZT powder was dry-pressed and sintered. However, to date there has also been no systematic characterization of the electromechanical properties and phase relationships for a single formulation of the "chem-prep" ceramic even within the limited temperature and pressure range over which some ferroelectric power supplies must reliably function.

The objective of this project is to obtain those properties and phase relationships so that the grain-scale modeling effort can develop and test its models and codes using realistic parameters obtained from a single formulation of the "chem-prep" PNZT within the temperature range of -55 to 75°C, and pressures to 500 MPa. The laboratory hydrostatic compression (HC) experiments were conducted on specimens instrumented to acquire data on transformation strains, strain anisotropy, and quasistatic bulk modulus as functions of temperature, pressure and phase (FE *vs.* AFE). The hydrostatic compression tests were supplemented with uniaxial compression (UC) experiments within the specified pressure and temperature ranges to quantify the interaction of transformation and dipole reorientation strains as a function of temperature. These interactions profoundly affect strain anisotropy under non-hydrostatic loading, which has been only superficially examined thus far. Constant-Stress-Difference (CSD) experiments were also conducted to determine the effects of non-hydrostatic compression on the mean stress for transformation.

Task 1. A series of HC experiments across the FE-AFE boundary was conducted on unpoled PNZT specimens in 10°C increments from -55 to 75°C. This density of experiments was necessary to investigate the curved structure of the boundary determined by Fritz and Keck (1978) for "mixed-oxide" ceramic. Strain measurements were performed on all experiments, which yielded a quasistatic bulk modulus and transformation strains.

Task 2. A series of UC experiments was conducted on unpoled ceramic at -55, 20 and 75°C. Acoustic velocity and strain measurements were used to measure changes in elastic properties and strains associated with stress induced dipole reorientation (Fritz and Keck, 1978; Fritz, 1979), the results of which can be used to test and calibrate models for stress-induced dipole reorientation. These experiments were carried to failure to observe the effect of a change of temperature (Zeuch *et al*., 1999b) on the manner in which dipole switching strains interact with transformation strains**.**

Task 3. A series of CSD experiments were conducted at four stress differences ($\sigma_d = \sigma_1 - \sigma_3$ = 50, 100, 150, and 200 MPa) at each of three different temperatures (-55, 25, and 75°C). These experiments characterized the effects of nonhydrostatic loading on phase transformation of the unpoled "chem-prep" ceramic. Nonhydrostatic loading has been shown to lower the mean stress for onset of the transformation in "mixed-oxide" ceramic.

2. Sample Preparation and Characterization

2.1 Sample materials

The PNZT ceramic specimens were produced based on Sandia National Laboratories TSP (Transferred Sandia Process). This is an upscaled SP (Sandia Process) chemical preparation process for the synthesis of PNZT powder (U.S. Patent No. 5,908,802 by Voigt *et al*., 1999). Figure 1 shows the flow diagram for key steps in solution synthesis of PNZT.

Our specimens came from sintering Lot HF803. The calcinated TSP38 powder was mixed with 0.9 w% of Lucite poreformer. The average density of the material from Lot HF803 was 7.358 g/cm^3. The general electromechanical characteristics of the ceramic from HF803 are shown in Table 1. The average depoling pressure of the ceramic from Lot HF803 is approximately 303 (±2) MPa and falls in the upper range of the depoling pressure. The average charge release of the ceramic from Lot HF803 was 31.9 (±0.2) μC/cm^2.

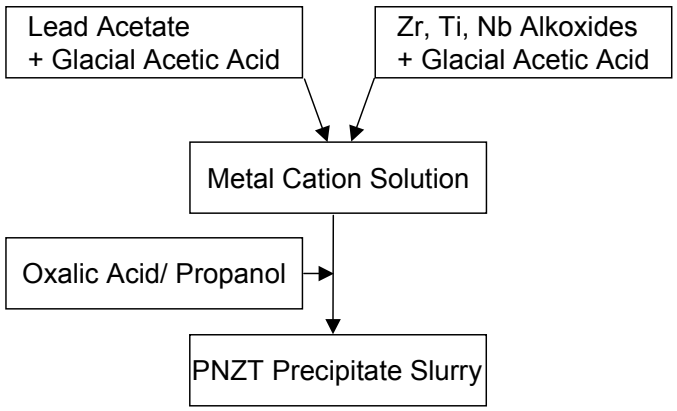

Figure 1. Overview of powder synthesis processing of PNZT (after Voigt *et al*., 1999, U.S. Patent #5,908,802).

Table 1. Electromechanical characteristics of "chem.-prep" PNZT-HF803. (from Pin Yang, 2003)

Serial no.	Depoling pressure (MPa)	Charge release ($\mu C/cm^2$)
X10774	304	32.1
X10825	302	31.7
X10827	303	31.8
X10837	306	32.1
X10845	303	31.9
X10865	301	31.8
X10927	301	32.0
X10939	299	31.5
X10942	305	32.3
X10978	306	32.2
Average:	303	31.9
Standard Deviation:	2	0.2
High:	306	32.3
Low:	299	31.5

2.2 Sample preparations

The unpoled PNZT test specimens were instrumented to acquire data on the strains due to phase transformation as a function of temperature during quasistatic loading. We fabricated rectangular parallelpeds of PNZT. The specimens have nominal dimensions of $10.8 \times 10.8 \times 25.4$ mm. The dimensions fall within the range of nominal length-to-diameter ratio (2 to 2.5). The ends of the specimen were ground flat within 0.003 mm tolerance. Samples were visually inspected for significant flaws and general straightness of the surfaces. The physical dimensions of each specimen are listed in Table 2 with assigned test type and conditions.

Two pairs of orthogonal sets of axial and lateral strain gages were mounted on opposite sides of the specimen (180° apart) at mid-height of the specimen. The axial and lateral gages were oriented to be parallel and perpendicular to the axis of the specimen, respectively. The axial (ε_a) and lateral (ε_l) strains were measured as the average strain from two respective strain gages. The volumetric strain, ε_v, was calculated as $\varepsilon_v = \varepsilon_a + 2\varepsilon_l$.

The instrumented specimen was placed between the upper and lower tungsten carbide end-caps. The strain-gaged specimen with two end-caps was coated with an approximately 1 mm thick impervious polyurethane membrane. To maintain uniform thickness of the membrane during curing, the specimen assembly was turned on a lathe along the axial centerline of the assembly. The flexible membrane allowed the confining pressure to be applied uniformly on the specimen and at the same time prevented the confining fluid from infiltrating into the specimen. In UC tests, a pair of acoustic wave velocity transducer is mounted on the opposite side of the specimen to measure the compressive (or P) wave velocity across the

specimen perpendicular to the loading axis. A typical PNZT specimen, ready to be tested, is shown in Figure 2.

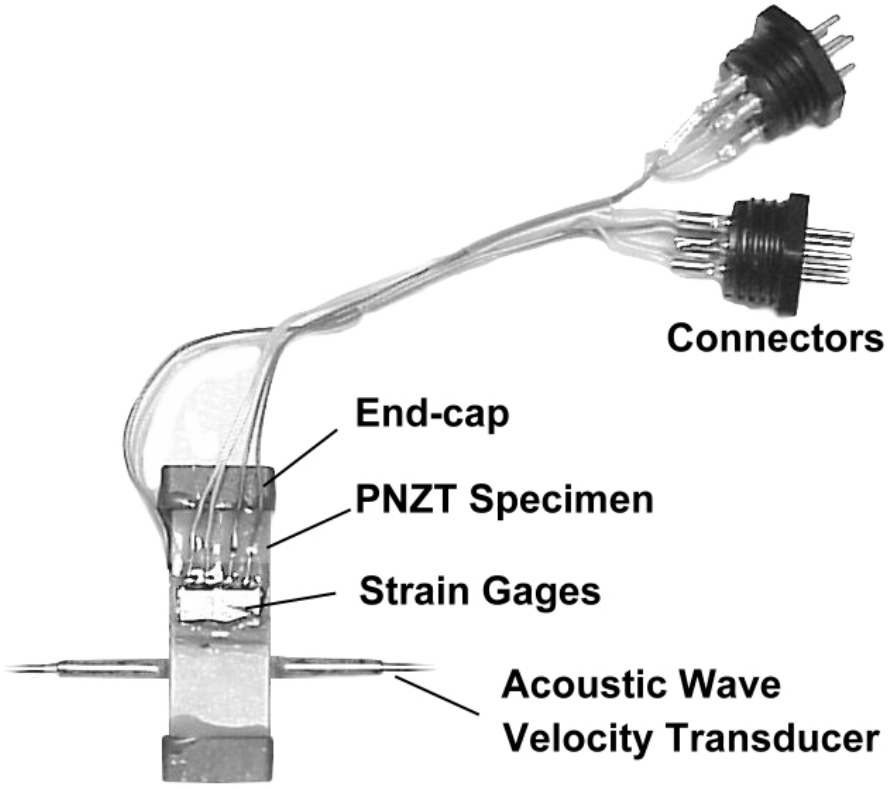

Figure 2. A typical PNZT specimen instrumented with two pairs of axial and lateral strain gages and piezoelectric crystals for measuring wave velocities. The specimen is placed between two tungsten carbide end-caps and the assembly is coated with polyurethane membrane to prevent the confining fluid from infiltrating into the specimen.

Table 2. List of mechanical tests conducted for "chem-prep" PNZT-HF803 specimens.

Specimen no.	Test type	Temperature (° C)	σ_1-σ_3 (MPa)	Length (cm)	Width (cm)	Height (cm)	Weight (g)	Density (g/cm^3)	Note
PNZT-01	UC	25	σ_1	1.077	1.080	2.540	21.75	7.365	
PNZT-02	UC	25	σ_1	1.080	1.080	2.540	21.74	7.345	
PNZT-03				1.080	1.080	2.540	21.76	7.352	
PNZT-04	UC	-55	σ_1	1.080	1.080	2.540	21.71	7.335	
PNZT-05				1.080	1.080	2.540	21.78	7.358	
PNZT-06	UC	77	σ_1	1.080	1.080	2.540	21.72	7.338	
PNZT-07	CSD	25	150	1.080	1.080	2.540	21.73	7.341	
PNZT-08	CSD	-55	100	1.080	1.080	2.540	21.71	7.335	
PNZT-09				1.077	1.080	2.543	21.75	7.358	Damaged
PNZT-10	CSD	25	50	1.080	1.080	2.543	21.73	7.334	
PNZT-11	CSD	25	200	1.080	1.080	2.540	21.74	7.345	
PNZT-12				1.080	1.080	2.543	21.78	7.351	
PNZT-13	CSD	25	50	1.080	1.080	2.543	21.75	7.341	
PNZT-14	CSD	25	150	1.082	1.080	2.540	21.75	7.331	
PNZT-15	CSD	25	100	1.080	1.082	2.540	21.75	7.331	
PNZT-16				1.080	1.080	2.543	21.67	7.314	Rejected
PNZT-17	CSD	25	50	1.080	1.080	2.543	21.73	7.334	
PNZT-18	CSD	25	100	1.080	1.080	2.540	21.73	7.341	
PNZT-19	CSD	25	150	1.080	1.080	2.543	21.76	7.344	
PNZT-20				1.080	1.080	2.540	21.73	7.341	
PNZT-21				1.080	1.080	2.543	21.78	7.351	
PNZT-22	CSD	-55	50	1.082	1.080	2.543	21.75	7.324	
PNZT-23	CSD	-55	200	1.080	1.080	2.543	21.71	7.327	
PNZT-24	CSD	-55	100	1.080	1.080	2.543	21.75	7.341	
PNZT-25	CSD	-55	100	1.080	1.080	2.543	21.78	7.351	
PNZT-26	CSD	-55	150	1.080	1.082	2.543	21.76	7.327	
PNZT-27	CSD	-55	150	1.082	1.080	2.540	21.79	7.345	
PNZT-28	CSD	-55	150	1.080	1.080	2.540	21.76	7.352	
PNZT-29				1.082	1.080	2.540	21.78	7.341	
PNZT-30	CSD	75	50	1.080	1.082	2.543	21.77	7.331	
PNZT-31	CSD	75	100	1.080	1.080	2.543	21.76	7.344	
PNZT-32	CSD	75	150	1.080	1.080	2.540	21.80	7.365	
PNZT-33	CSD	75	200	1.080	1.080	2.540	21.76	7.352	
PNZT-34	HC	25	0	1.080	1.080	2.540	21.75	7.348	
PNZT-35	CSD	75	50	1.080	1.080	2.540	21.68	7.325	
PNZT-36	CSD	75	150	1.080	1.080	2.543	21.74	7.338	
PNZT-37	HC	75	0	1.077	1.077	2.540	21.70	7.365	
PNZT-38				1.080	1.080	2.540	21.77	7.355	
PNZT-39				1.080	1.080	2.543	21.74	7.338	
PNZT-40				1.080	1.080	2.540	21.74	7.345	
PNZT-41				1.080	1.080	2.540	21.78	7.358	
PNZT-42				1.080	1.080	2.543	21.74	7.338	
PNZT-43				1.080	1.080	2.540	21.76	7.352	
PNZT-44	HC	58	0	1.080	1.080	2.540	21.78	7.358	
PNZT-45	HC	41	0	1.080	1.080	2.540	21.74	7.345	
PNZT-46				1.080	1.080	2.540	21.62	7.304	Rejected

PNZT-47				1.080	1.080	2.540	21.72	7.338	
PNZT-48				1.080	1.080	2.543	21.74	7.338	
PNZT-49	HC	15	0	1.080	1.080	2.540	21.74	7.345	
PNZT-50				1.077	1.080	2.538	21.77	7.379	Rejected
PNZT-51				1.080	1.080	2.540	21.76	7.352	
PNZT-52	HC	-55	0	1.077	1.080	2.540	21.76	7.369	Rejected
PNZT-53	HC	-25	0	1.080	1.080	2.540	21.70	7.331	
PNZT-54				1.080	1.080	2.543	21.77	7.348	
PNZT-55	HC	5	0	1.080	1.080	2.540	21.71	7.335	
PNZT-56	HC	-5	0	1.080	1.080	2.540	21.73	7.341	
PNZT-57	HC	-15	0	1.080	1.080	2.540	21.79	7.362	
PNZT-58	HC	-10	0	1.080	1.080	2.540	21.78	7.358	
PNZT-59	HC	-5	0	1.080	1.080	2.540	21.73	7.341	
PNZT-60	HC	75	0	1.080	1.077	2.540	21.66	7.335	
PNZT-61	HC	58	0	1.080	1.077	2.540	21.75	7.365	
PNZT-62				1.080	1.080	2.540	21.81	7.368	Rejected
PNZT-63	HC	-35	0	1.080	1.080	2.540	21.70	7.331	
PNZT-64	HC	-45	0	1.080	1.080	2.543	21.75	7.341	
PNZT-65	HC	15	0	1.080	1.080	2.540	21.73	7.341	
PNZT-66				1.080	1.080	2.540	21.79	7.362	
PNZT-67				1.080	1.080	2.540	21.78	7.358	
PNZT-68				1.080	1.080	2.540	21.76	7.352	
PNZT-69				1.080	1.080	2.540	21.79	7.362	
PNZT-70				1.080	1.080	2.540	21.66	7.318	Rejected
PNZT-71	UC	-55	σ_1	1.080	1.080	2.540	21.75	7.348	

UC-Uniaxial Compression; CSD-Constant Stress Difference; HC-Hydrostatic Compression
σ_1-major principal stress; σ_3-minor principal stress

The following figure shows that six PNZT-HF803 specimens fell in the <5% or >95% "tail" regions of the density distribution plot. These specimens were considered as "outliers" and rejected for further experimental analyses.

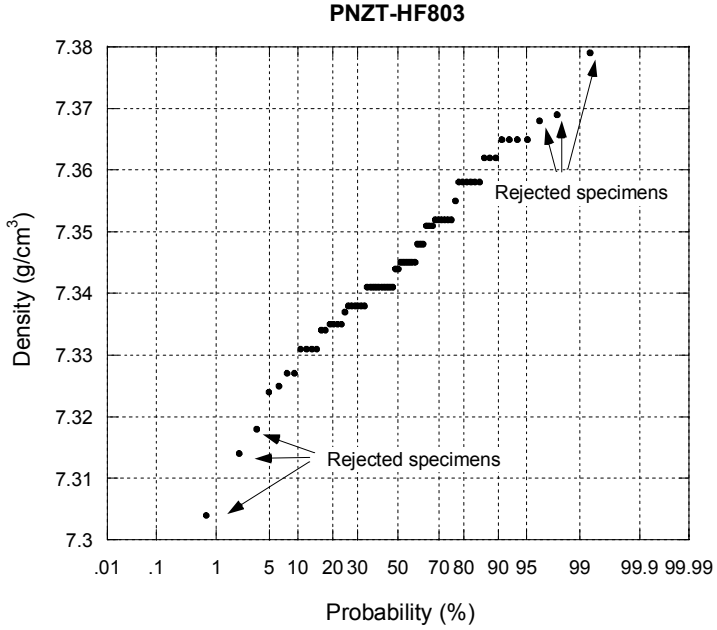

2.3 Experimental set-up

A High-Pressure Low-Temperature (HPLT) triaxial cell (Zeuch *et al*., 1999d) was designed and built to characterize the electromechanical properties of PNZT and other materials such as ALOX (Alumina Loaded Epoxy) and frozen soil (Lee *et al*., 2002). It is capable of operating at temperature ranges from –65 to 150°C and confining pressures up to 500 MPa. The HPLT triaxial cell has a bore diameter of 82 mm and length of 200 mm. The cell is able to accept specimens, in the form of cylinder or rectangular parallelepiped, having diameters (or face diagonals) up to 25 mm and lengths up to 50 mm. Figure 3 shows the schematic of the load frame and instrumented PNZT specimen integrated with the HPLT triaxial cell. In addition to the fundamental operating conditions of temperature, pressure and large specimen size required for the test cell, additional requirements and restrictions imposed serious constraints upon the design. These additional requirements included, for example, the necessity to: (1) fit in an existing, 1.9 MN servo-controlled load frame; (2) operate within an otherwise normal laboratory setting (*i.e.,* not in a cold room); and (3) use a liquid confining medium for safety and system controllability. Owing to the extreme operating conditions and the likelihood of high piston-seal friction, we also decided that internal load and strain measurements, and hence, numerous high-pressure feed-throughs, would be necessary. Nevertheless, despite these and other restrictions, it was deemed feasible to use an externally cooled pressure vessel composed of HP9-4-20 alloy steel and equipped with twelve coaxial feed-throughs. Two specially designed load cells have been built for internal force measurements. Strains were measured using the strain gages mounted on the specimen.

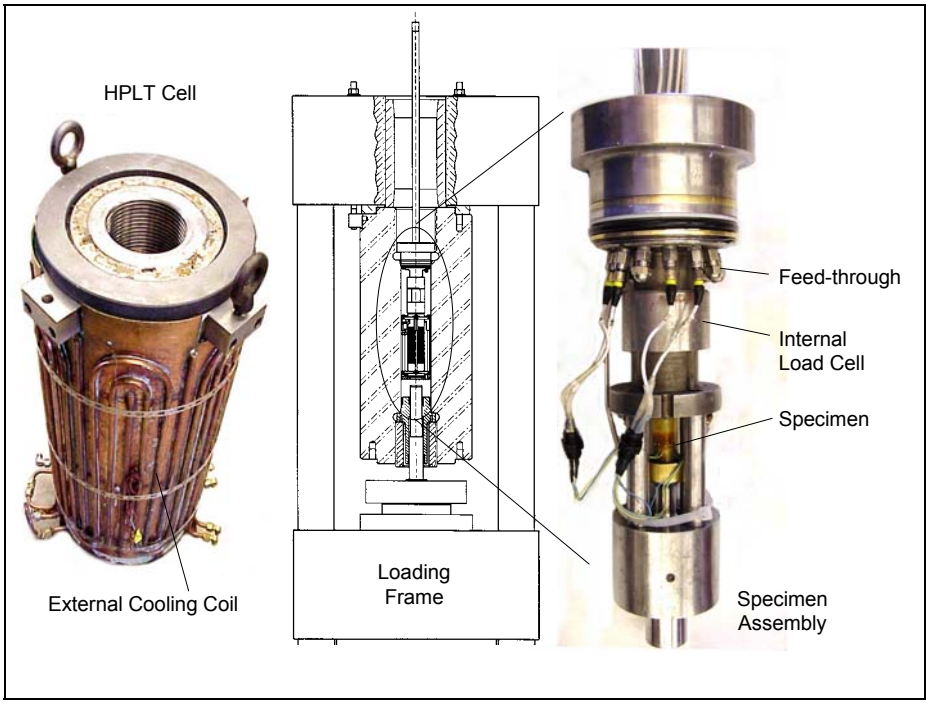

Figure 3. Externally cooled High-Pressure-Low-Temperature (HPLT) cell and an assembly of PNZT specimen.

2.4 Experimental procedure

Three different loading paths were used for uniaxial compression, hydrostatic compression, and constant stress difference testing. Appropriate loading paths are shown in Figures 4 and 5.

For hydrostatic compression, the piston, used for applying the axial load to the specimen, was pulled back so as not to apply any deviatoric stress to the specimen. The confining pressure, P, was increased at the rate of 0.69 MPa/s all around the specimen to apply all three principal stresses $\sigma_1=\sigma_2=\sigma_3=P$ to the specimen past the hydrostatic pressure for transformation, P_T^{HC}. The loading history of the hydrostatic compression is represented by the dotted straight line in Figure 4.

For uniaxial compression, the axial load was applied without confining pressure ($\sigma_2 = \sigma_3 = P = 0$). The piston was moved at a constant rate of 2.54×10^{-4} mm/s which corresponds to the strain rate of 10^{-5}/s. The loading history of the uniaxial compression is shown as the thick vertical line UC in Figure 4.

For constant stress difference testing, the specimen was hydrostatically compressed at about 69 MPa which is below the expected pressure for transformation, P_T^{HC}. At that pressure the piston was moved to make a contact with the specimen. Then additional load was applied to the specimen creating the stress difference ($\sigma_1-\sigma_3=\sigma_d$). The axial stress ($\sigma_1$) and the confining pressure ($P=\sigma_3$) were increased simultaneously at the same rate to maintain the stress difference (σ_d) constant. This loading path created a constant increase of the mean stress while maintaining the stress difference constant. The loading path of the constant stress difference testing is shown as CSD in Figure 4.

Figure 5 shows three stress paths plotted in domain of stress invariants: $I_1=(\sigma_1+\sigma_2+\sigma_3)$ and $J_2=\frac{(\sigma_1-\sigma_2)^2+(\sigma_2-\sigma_3)^2+(\sigma_3-\sigma_1)^2}{6}$. During HC and CSD testing, the deviatoric component of stresses shown in terms of J_2 was kept constant throughout the test except for the stress difference σ_d set for CSD. For UC testing, deviatoric component of stresses increased linearly with hydrostatic component of stresses.

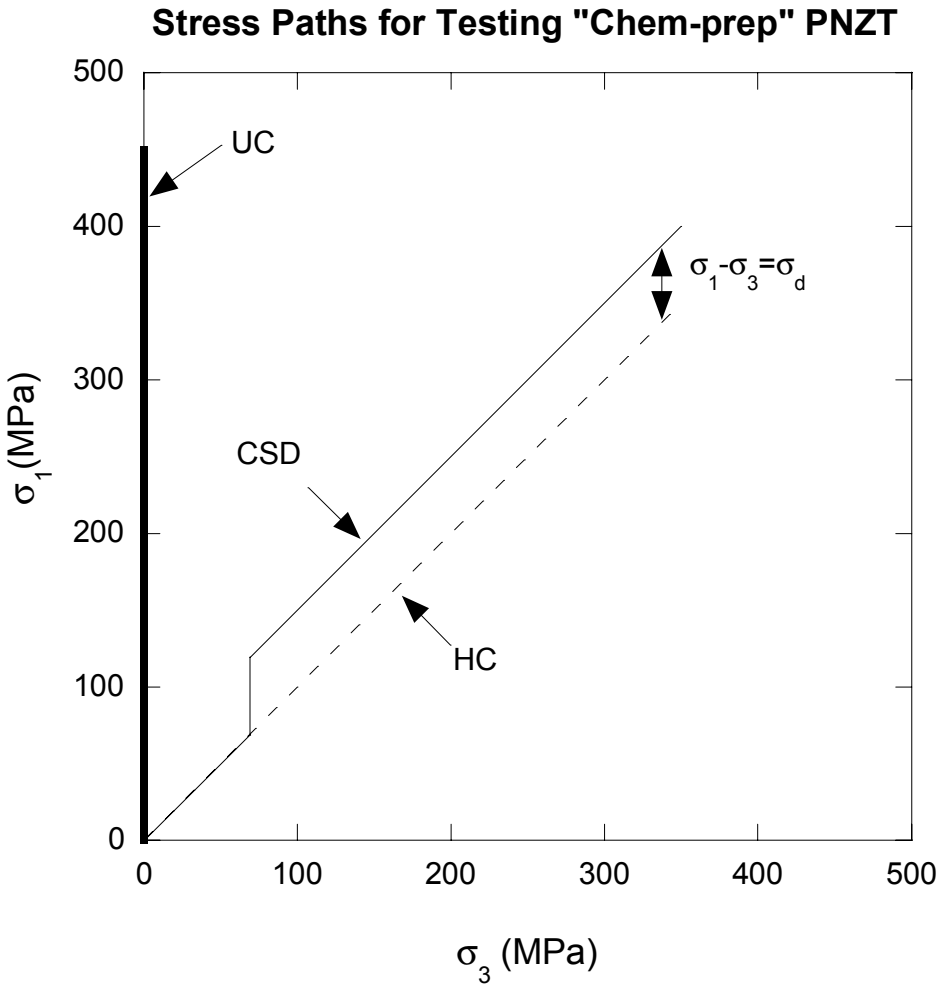

Figure 4. Three different loading paths are shown in the principal stress domain (σ_1-σ_3): UC for Uniaxial Compression, HC for Hydrostatic Compression, and CSD for Constant Stress Difference. The stress difference, σ_1-σ_3, is shown as σ_d .

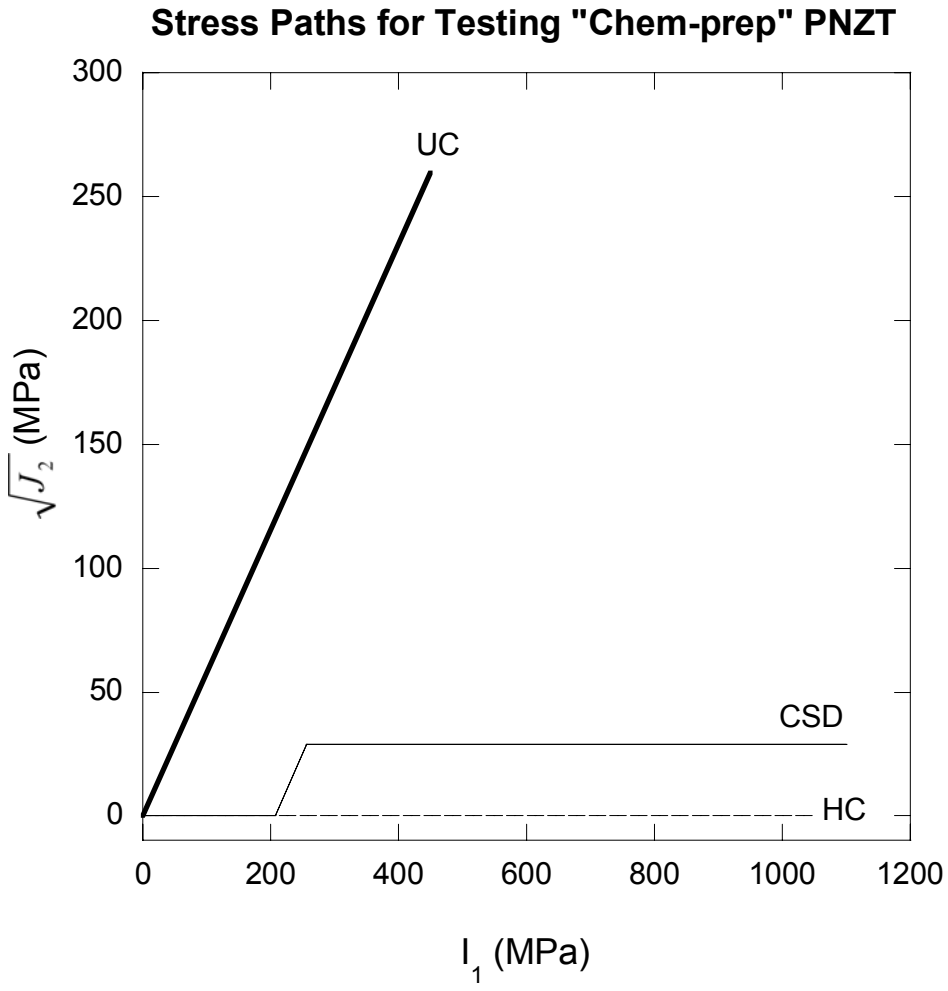

Figure 5. Three different loading paths are shown in the stress invariant domain of $(I_1, \sqrt{J_2})$: UC for Uniaxial Compression, HC for Hydrostatic Compression, and CSD for Constant Stress Difference. $I_1=(\sigma_1+\sigma_2+\sigma_3)$ is the first invariant of stress and $J_2=\frac{(\sigma_1-\sigma_2)^2+(\sigma_2-\sigma_3)^2+(\sigma_3-\sigma_1)^2}{6}$ is the second invariant of stress.

3. Material Testing

3.1 Hydrostatic compression tests

The mechanical behavior of "chem-prep" PNZT under hydrostatic loading was studied using a pressure (P)-volumetric strain (ε_v) plot. Figure 6 shows a typical record obtained from specimen PNZT-65 at 15°C. At a hydrostatic pressure of approximately 236 MPa, the unpoled PNZT underwent a phase transformation from a ferroelectric rhombohedral perovskite structure (F_{R1} or FE) to an antiferroelectric orthorhombic (A_o or AFE) structure. In order to characterize the phase transformation quantitatively, the P-ε_v plot was divided into three segments represented by three straight lines.

$$\begin{aligned} P_F &= a_1 + K_F \varepsilon_v \quad (\text{where} \quad 0 < \varepsilon_v < \varepsilon_{v1}) \\ P_{FA} &= a_2 + K_{FA} \varepsilon_v \quad (\text{where} \quad \varepsilon_{v1} \le \varepsilon_v < \varepsilon_{v2}) \\ P_A &= a_3 + K_A \varepsilon_v \quad (\text{where} \quad \varepsilon_{v2} \le \varepsilon_v) \end{aligned} \qquad (1)$$

The first segment, defined by a straight line with bulk modulus K_F as a slope, represents the mechanical behavior of PNZT in a FE phase. This linear increase of ε_v as a function of P continues until the hydrostatic pressure reaches the phase transformation pressure P_{T1}^H at P_1. The volumetric strain at that pressure is represented by ε_{v1}. The phase transformation is marked by a sudden increase in volumetric strain (or reduction in volume) shown as a nearly horizontal line with a slope of K_{FA}. The completion of phase transformation is shown as the abrupt increase of the slope at P_2. The volumetric strain and hydrostatic pressure at this point is represented as ε_{v2} and P_{T2}^H, respectively. The remaining segment represents an AFE phase showing the higher bulk modulus K_A.

The unknown parameters of the three straight lines were obtained using a linear regression analysis applied to the linear portion of the segments (0 to 150 MPa for $P_F = a_1 + K_F$; the arbitrarily selected linear portion for $P_{FA} = a_2 + K_{FA}\varepsilon_v$; and the unloading portion of the data from the maximum pressure to 200 MPa for $P_A = a_3 + K_A\varepsilon_v$). The linear representation of the transitional segment, $P_{FA} = a_2 + K_{FA}\varepsilon_v$, is subjective and is largely dependent on the selection of data to be analyzed.

Hydrostatic compression experiments were performed on large test specimens ($10.8 \times 10.8 \times 25.4$ mm) across the FE-AFE boundary in 10°C increments within the temperature range of -55 to 75°C, and pressures up to 500 MPa. A total of thirteen specimens were tested mostly at 10°C increment. Each pressure (P)-volumetric strain (ε_v) plot is shown in Appendix A. Effects of temperature on the behavior of P-ε_v during phase transformation are shown in Figure 7. A detailed quantitative description of phase transformation in PNZT-HF803 under hydrostatic loading is summarized in Table 3.

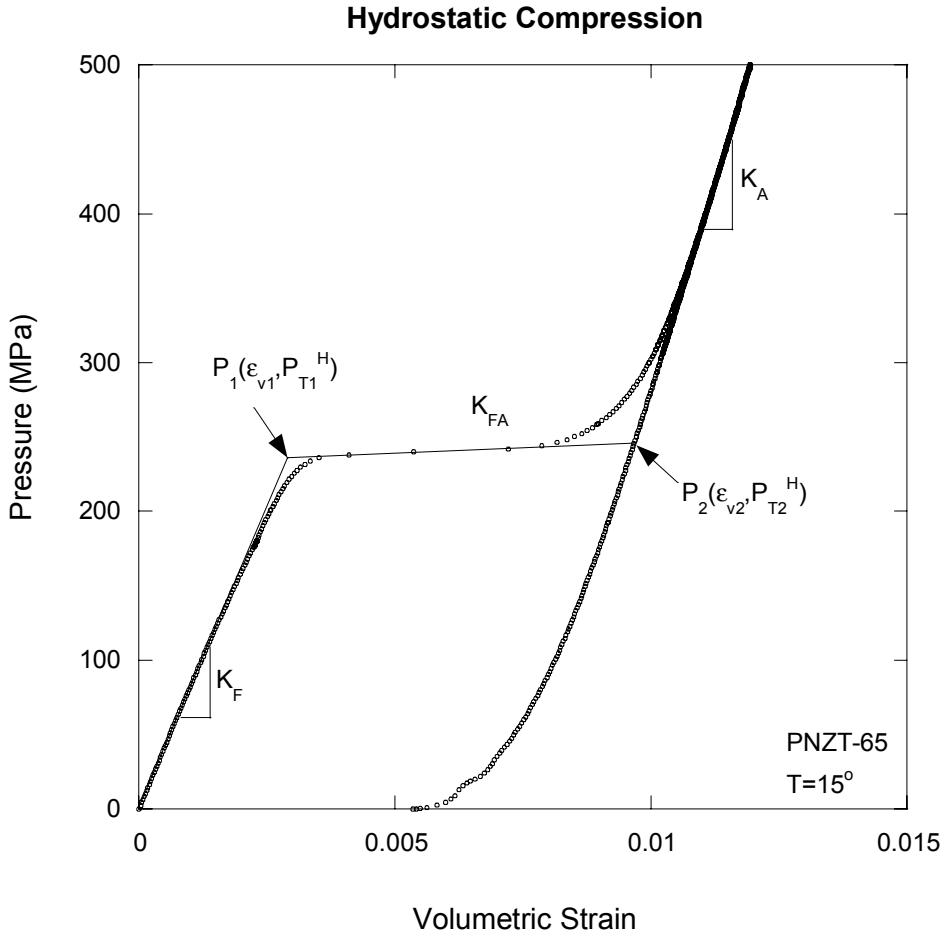

Figure 6. Quantitative description of phase transformation in "chem-prep" PNZT under hydrostatic loading. The initiation of phase transformation is represented by P_1. The volumetric strain and hydrostatic pressure at P_1 is ε_{v1} and P_{T1}^H, respectively. K_F represents the bulk modulus of the ceramic in FE phase. The completion of phase transformation is represented by P_2. The volumetric strain and hydrostatic pressure at P_2 is ε_{v2} and P_{T2}^H, respectively. K_A represent the bulk modulus of the ceramic in AFE phase. The phase transformation is represented by a straight line connecting P_1 and P_2 with slope K_{FA} ($=\frac{P_{T2}^H - P_{T1}^H}{\varepsilon_{v2} - \varepsilon_{v1}}$).

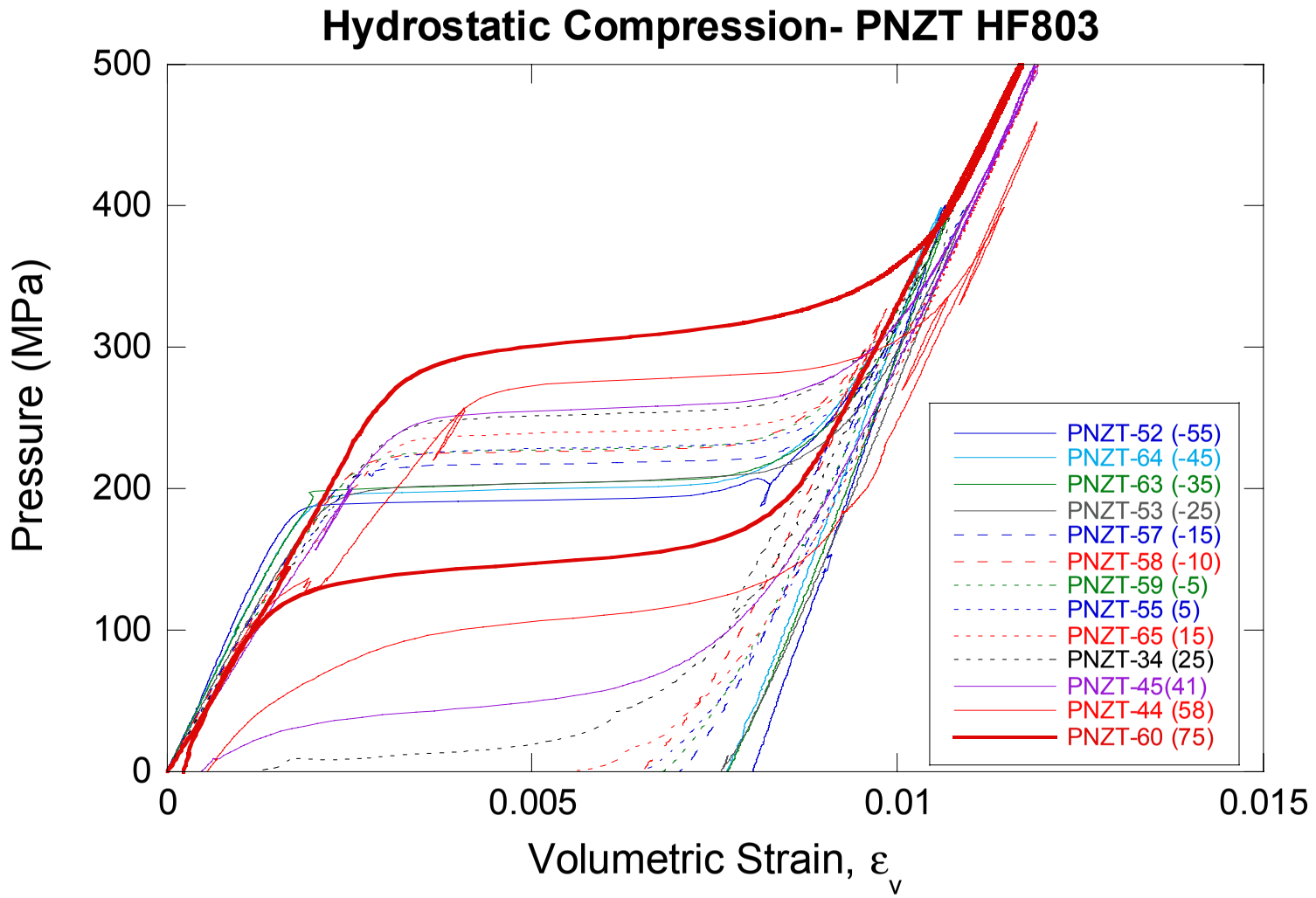

Figure 7. Pressure-Volumetric strain plot for hydrostatic compression tests on PNZT-HF803 specimens under different temperature conditions ranging from -55 to 75ºC.

Table 3. Summary of phase transformation in "chem-prep" PNZT-HF803 under hydrostatic compression (HC).

Specimen no.	Temperature (° C)	a_1 (MPa)	K_F (GPa)	a_2 (MPa)	K_{FA} (GPa)	a_3 (MPa)	K_A (GPa)	ε_{v1}	P_{T1}^H (MPa)	ε_{v2}	P_{T2}^H (MPa)	$\varepsilon_{v2} - \varepsilon_{v1}^*$	$P_{T2}^H - P_{T1}^{H**}$ (MPa)
PNZT-52	-55	-1.0	115.3	187.2	1.0	-1220.4	151.7	0.0016	189	0.0093	196	0.0077	7.6
PNZT-64	-45	0.8	104.2	193.5	1.3	-1107.8	142.2	0.0019	196	0.0092	205	0.0074	9.5
PNZT-63	-35	1.1	103.2	196.5	1.4	-1103.5	139.9	0.0019	199	0.0094	210	0.0075	10.7
PNZT-53	-25	1.8	93.8	197.4	1.3	-1024.3	129.9	0.0021	200	0.0095	210	0.0074	9.8
PNZT-57	-15	1.9	92.1	214.3	0.8	-940.7	125.7	0.0023	216	0.0092	221	0.0069	5.4
PNZT-58	-10	1.8	90.6	222.3	0.8	-883.5	122.8	0.0025	224	0.0091	230	0.0066	5.5
PNZT-59	-5	1.1	89.5	222.8	1.0	-906.8	122.0	0.0025	225	0.0093	232	0.0068	6.6
PNZT-55	5	2.1	85.7	222.9	1.1	-865.5	115.6	0.0026	226	0.0095	234	0.0069	7.8
PNZT-65	15	0.9	80.9	232.7	1.3	-845.7	112.6	0.0029	236	0.0097	245	0.0068	8.9
PNZT-34	25	2.0	84.1	242.9	1.7	-769.0	108.8	0.0029	248	0.0095	259	0.0065	11.3
PNZT-45	41	-0.3	80.8	244.4	2.1	-803.7	109.1	0.0031	251	0.0098	265	0.0067	14.1
PNZT-44	58	2.0	82.7	262.1	2.4	-863.0	111.0	0.0032	270	0.0104	287	0.0071	17.0
PNZT-60	75	-1.5	87.4	271.9	5.8	-679.4	101.0	0.0033	291	0.0100	329	0.0066	38.2

K_F - bulk modulus in FE (ferroelectric) phase

K_{FA} - bulk modulus in transition from FE to AFE phase transformation

K_A - bulk modulus in AFE (antiferroelectric) phase

a_1- extrapolated pressure corresponding to zero volumetric strain in FE phase

a_2 - extrapolated pressure corresponding to zero volumetric strain during transition from FE to AFE phase

a_3 - extrapolated pressure corresponding to zero volumetric strain in AFE phase

P_{T1}^H - pressure for initiation of FE to AFE phase transformation under hydrostatic compression

P_{T2}^H - pressure for completion of FE to AFE phase transformation under hydrostatic compression

ε_{v1} - volumetric strain at P_{T1}^H

ε_{v2} - volumetric strain at P_{T2}^H

* - Increase in volumetric strain during FE to AFE phase transformation

** - Pressure increase during FE to AFE phase transformation

Effects of Temperature on the Phase Transformation Pressures

The variations of pressures required for the onset (P_{T1}^{H}) and completion (P_{T2}^{H}) of FE to AFE phase transformation depend on temperature. As shown in Figure 8, P_{T2}^{H} data are well represented by a second-order polynomial function of temperature. However, the onset of transition P_{T1}^{H} is well represented by a simple straight line. The best-fit curves are:

$$P_{T1}^{H}\ (\text{MPa}) = 227 + 0.76\ T\ (^{o}\text{C}) \qquad (2)$$

$$P_{T2}^{H}\ (\text{MPa}) = 232 + 0.83\ T\ (^{o}\text{C}) + 0.0047\ T^{2}(^{o}\text{C}) \qquad (3)$$

where the phase transformation pressures P_{T1}^{H} and P_{T2}^{H} are in MPa and T is temperature in degree C. The curved shape of the phase boundary, especially for the completion pressure P_{T2}^{H}, corroborates well with the previous findings in "mixed-oxide" ceramic in the phase diagram (Fritz and Keck, 1978).

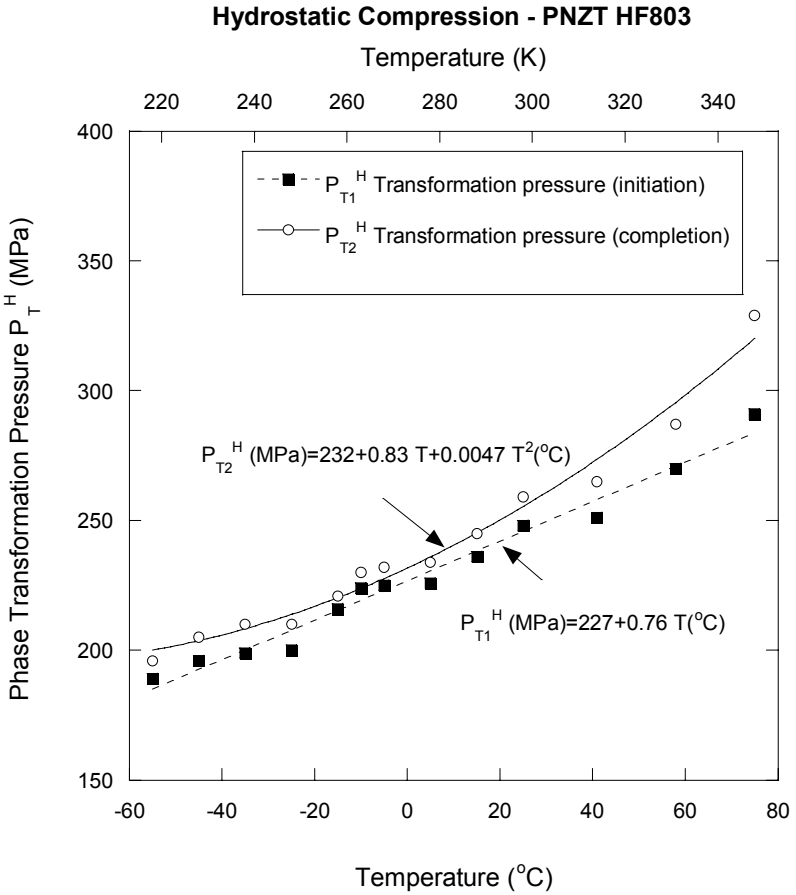

Figure 8. Phase transformation pressures plotted as a function of temperature. Both initiation (P_{T1}^{H}) and completion (P_{T2}^{H}) pressures for phase transformation increase with temperature under hydrostatic pressure.

Effects of Temperature on the Phase Transformation Strains

The volumetric strains at phase boundaries are plotted as a function of temperature (Figure 9). The volumetric strains for the onset of FE to AFE transformation increase with temperature in degree C:

$$\varepsilon_{v1} = 0.0025 + 1.4 \times 10^{-5}\ T\ (^{o}C) \qquad (4)$$

The volumetric strains for the completion of FE to AFE transformation also increase with temperature:

$$\varepsilon_{v2} = 0.0095 + 7.2 \times 10^{-6}\ T\ \ (^{o}C) \qquad (5)$$

The difference between ε_{v2} and ε_{v1} corresponds to the sudden volume reduction during phase transformation. The amount of volume reduction decreases with temperature and can be represented as follows:

$$\varepsilon_{v2} - \varepsilon_{v1} = 0.007 - 6.6 \times 10^{-6}\ T\ (^{o}C) \qquad (6)$$

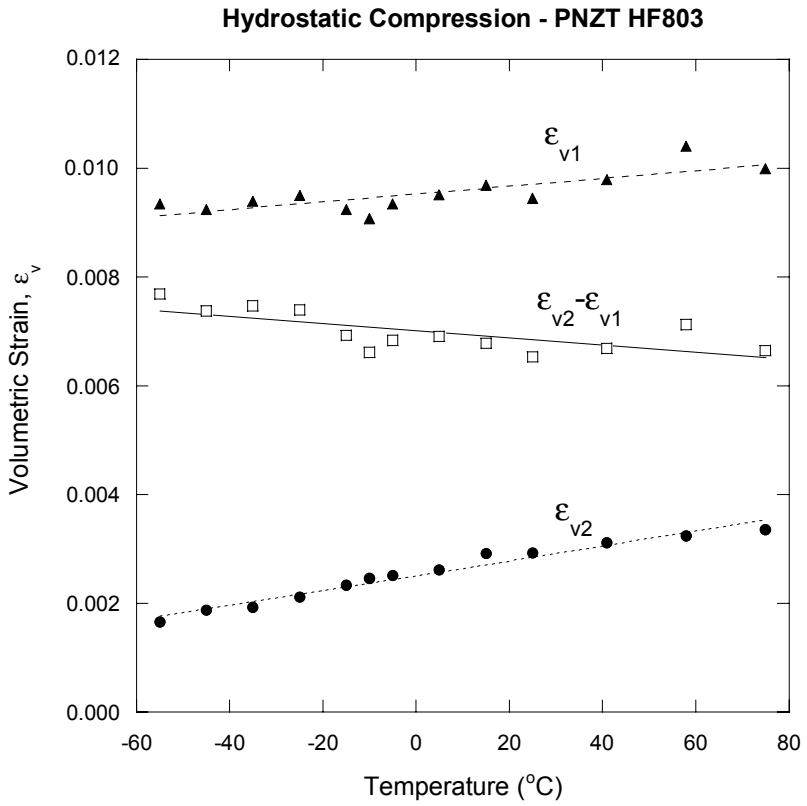

Figure 9. Variations of volumetric strains (ε_v) with temperature during FE to AFE phase transformation.

Effects of Temperature on the Bulk Moduli

Figure 10 shows the variations of bulk moduli K_A and K_F and a tangent modulus K_{FA} of the "chem-prep" PNZT-HF803 with temperature. The results clearly show that, within experimental uncertainty the bulk moduli, K_A and K_F, decrease with increasing temperature

$$K_F\,(\text{GPa}) = e^{-0.03T\,(^{o}\text{C}) + 1.73} + 82 \qquad (7)$$

$$K_A\,(\text{GPa}) = e^{-0.02T\,(^{o}\text{C}) + 3.06} + 98 \qquad (8)$$

where T is temperature in degree C. It also shows that the bulk modulus K_A, after the completion of FE to AFE transition, becomes about 34 % higher than K_A in AFE phase ($K_A \approx 1.35K_F$). The tangent modulus during transition remains constant or slightly increases with the rise of the temperature.

$$K_{FA}\,(\text{GPa}) = e^{0.06T\,(^{o}\text{C}) - 3.03} + 1 \qquad (9)$$

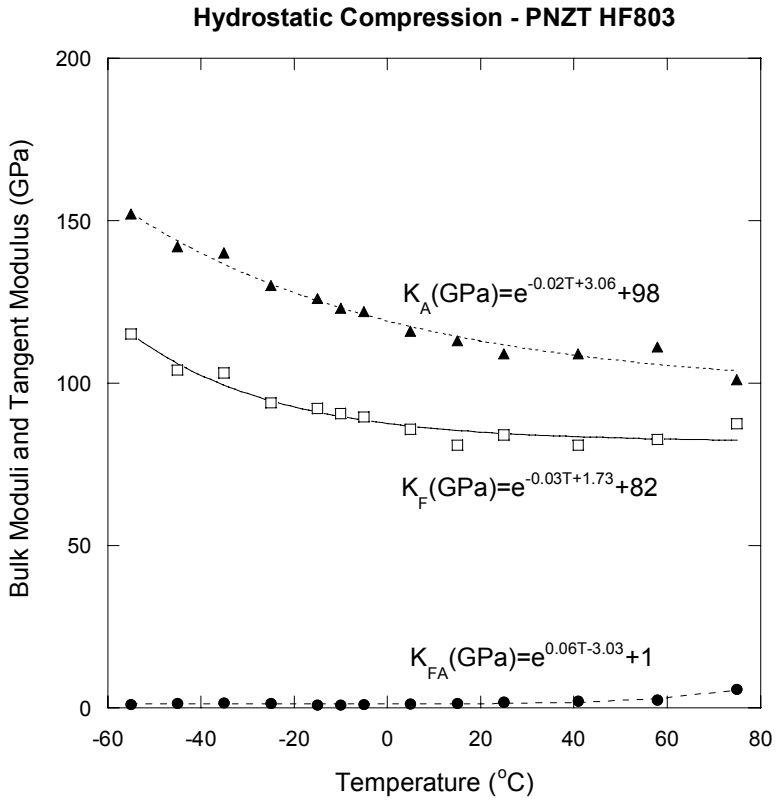

Figure 10. Variations of bulk moduli (K_A and K_F) and transitional tangent modulus (K_{FA}) with temperature for "chem-prep" PNZT-HF803 under hydrostatic compression. K_A and K_F, are bulk moduli for AFE and FE phases, respectively. The tangent modulus K_{FA} represents the slope of volumetric strain vs. pressure data during AFE to FE transition phases.

The results described above are consistent with previous observations on specimens of unpoled "mixed-oxide" PNZT ceramic from batch HF453 tested under quasi-static conditions using hydrostatic, uniaxial compression, and constant strain different loading paths. However, a comparison of properties K_F and K_A obtained from the hydrostatic loading indicate that material from HF803 appears significantly stiffer than material from HF453. In particular, the value of K_F, at room temperature, is ~80 GPa (see Table 3) for material from HF803 and 64.4 GPa (Zeuch *et al.*, 1999d) for material from HF453. This variation in bulk modulus is significantly larger than would be expected by changing from a "mixed-oxide" to a "chem-prep" process for fabricating the ceramic and is being investigated. As described below, the larger values of the bulk modulus observed for HF803 could possibly be attributed to the material being in a mixed phase, i.e. having both FE and AFE phases present.

The usefulness of PNZT ceramic as sources of shock activated electrical power sources is due to the close proximity of the free energies of the FE and AFE phases. It is quite possible to fabricate material as a mixture of the two phases due to the close proximity of the free energies. Because the free energy of the AFE phase is so close to the free energy of the FE phase it is relatively easy to induce an AFE-to-FE phase transformation by the application of an electric field. Consequently, the poling process used to prepare the PNZT material for use as shock activated electrical power sources can convert a mixed phase unpoled ceramic material into a single phase poled FE ceramic. The electromechanical characteristics for HF803 listed in Table 1 indicate that this material is entirely in the FE phase after electrical poling.

It is useful to examine the volume strain on transform from the FE to the AFE phase. Unit cell volumes for the FE and AFE phases are 71.32 $Å^3$ and 70.59 $Å^3$ (Tuttle *et al.*, 2000), consequently the volume strain associated with the phase transformation should be approximately 1 % in solid material. However, the "mixed-oxide" and "chem-prep" materials are porous with the average densities of HF453 and HF803 being about 7.3 and 7.4 gm/cm^3. Based in a theoretical solid density of about 8.0 g/cm^3 the initial distention ratios for HF453 and HF803 are about 1.096 and 1.081. The initial distention ratio, α_0, for a material is calculated as the ratio of its theoretical solid density and initial porous density. If we assume that the distention ratio does not significantly change when the material transforms from the FE to the AFE phase, it would be expected that both materials exhibit similar volumetric transformation strains of roughly 1 %. The volumetric transformation strains observed at room temperature for HF453 and HF803 are roughly 0.9 % and 0.7 %. The smaller value of transformation strain observed for HF453 and HF803 indicates the possible presence of some material in the AFE phase

Phase Reversal and Temperatures

After the transformation was completed at pressure P_{T2}^{H}, the hydrostatic pressure was increased up to 500 MPa following the upward slope of bulk modulus K_A of the ceramic in AFE phase. Upon depressurization, the volumetric strain was partially recovered following the downward slope of K_A. At high temperatures above the ambient condition, the phase transformation was reversible from AFE to FE. At low temperatures, the FE to AFE transition became permanent and the ceramic did not reverse to FE phase even after the hydrostatic pressure had been removed. Figure 11 shows an example of the P-ε_v plots from two hydrostatic compression experiments for bounding temperature range of -55 to 75°C.

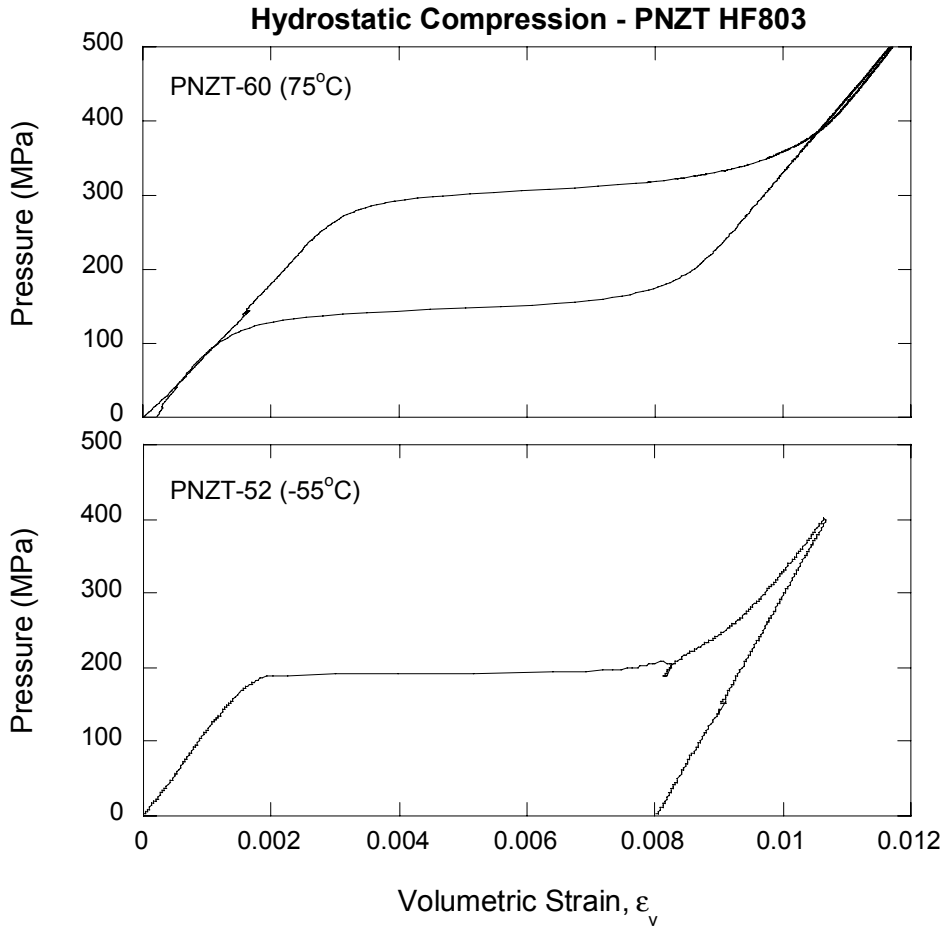

Figure 11. Examples of reversibility of phase transformation (AFE to FE) under hydrostatic loading for bounding temperature range of -55 to 75°C. At 75°C PNZT-60 specimen shows a complete reversal of the phase transformation. In contrast at -55°C, the transformation strain (about 0.8%) and the FE to AFE phase transformation were permanent.

3.2 Unconfined uniaxial compression tests

Uniaxial compression experiments were conducted on unpoled PNZT specimens at three different temperatures of -55, 25 and 75°C. Acoustic velocity and strain measurements were used to measure changes in elastic properties and strains associated with dipole reorientation (or domain switching) and also phase transformation. The stress-strain records and the acoustic velocity data for all UC experiments are shown in Appendix B.

The specimens were prepared in the form of rectangular parallelepipeds with the same specifications used for other types of testing (HC and CSD). The uniaxial compression tests were carried out in an environmental chamber adapted to a 0.1 MN servo-controlled loading machine (Figure 12). The temperature changes in the chamber were controlled by heating elements and a forced circulation of liquid nitrogen. The thermocouple, placed inside the chamber close to the specimen, constantly measured the air temperature and provided feedback signal to the temperature controller. Two through-wall ports, opened in the vertical direction of the chamber, accommodated the loading pistons.

The instrumented specimen (see Figure 2 in Chapter 1) was placed between the upper and lower loading pistons and loaded until it failed. The axial and lateral deformations were measured from a pair of axial and lateral strain gages, respectively. A pair of acoustic transducers measured changes of P-wave velocities perpendicular to the loading direction. The data acquisition system for measuring P-wave velocities was based on an 8-bit wave-form digitizer at sampling rate up to 5×10^9 samples/s.

Figure 12. A uniaxial compression test set-up consisting of a 0.1 MN load-frame and an environmental chamber for temperature control.

Stress-Strain Relationships during UC

A typical uniaxial compression experiment conducted on unpoled PNZT ceramic from batch HF803 is shown in Figure 13. The major principal stress, σ_1, applied axially to the specimen is plotted against axial (ε_a) and lateral (ε_l) strains, respectively. The volumetric strain ($\varepsilon_v = \varepsilon_a + 2\varepsilon_l$) is also plotted. The failure of the specimen is indicated as the peak of the stress-strain curve and the corresponding major principal stress is shown as $\sigma_{1,f}$.

As the axial stress is increased, ε_a and ε_l behave linearly up to the onset of nonlinear behavior indicated as σ_{R1}^U. The stress level corresponding to σ_{R1}^U is well below the stress level required for phase transformation, σ_{T1}^U, identified as the onset of deviation in the linear trend of σ_1 vs. ε_v. The stress-strain behavior past σ_{R1}^U is that ε_a becomes more compressive and ε_l becomes more tensile compared to elastic responses of the "chem-prep" PNZT specimen. However, each axial and lateral component of strains behaves proportionally, therefore, overall linear trend of the volumetric strain is maintained until the phase transformation initiates at σ_{T1}^U as shown in Figure 13.

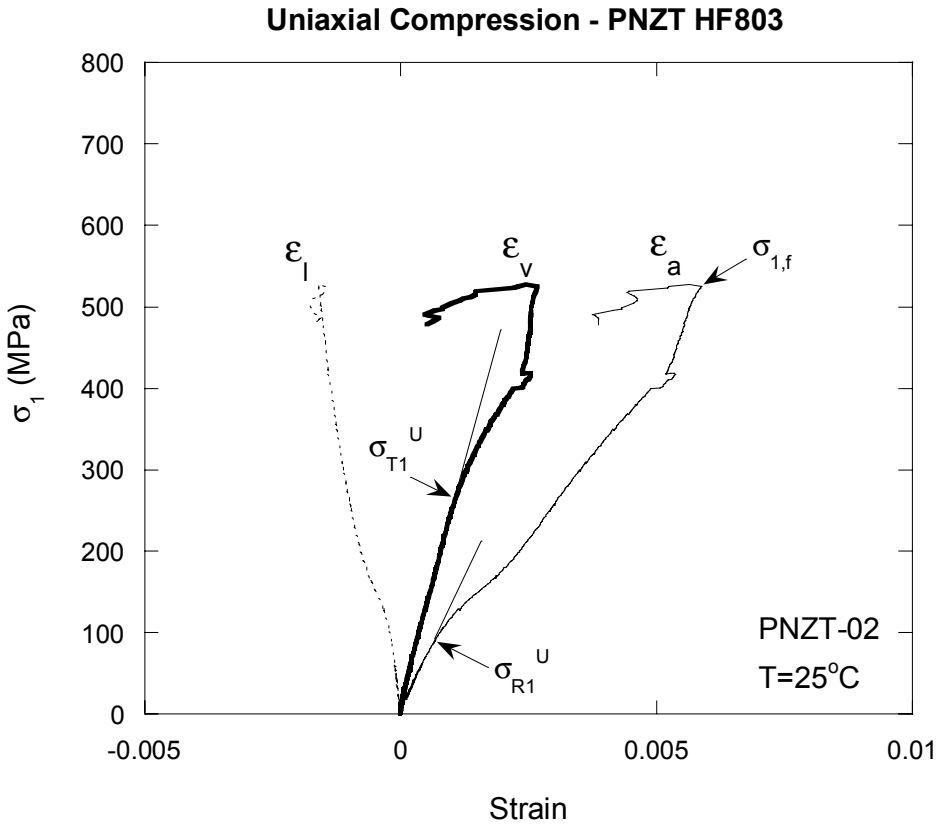

Figure 13. Typical uniaxial compression experiment on unpoled PNZT-HF803 ceramic. The major principal stress, σ_1, is plotted against axial (ε_a), lateral (ε_l) and volumetric (ε_v) strains, respectively. The major principal stress corresponding to the failure of the ceramic is indicated as $\sigma_{1,f}$. The major principal stress required for dipole reorientation under uniaxial compression is shown as σ_{R1}^U. The major principal stress for the initiation of FE to AFE phase transformation under uniaxial compression is indicated as σ_{T1}^U.

According to Fritz (1979), uniaxial compression results of this nature indicate dipole reorientation in a low stress regime before phase transformation occurs. Our experimental observation in PNZT-02 shown in Figure 13 is in excellent accordance with the characteristics of isovolumetric phenomenon of dipole reorientation. Moreover, as the axial stress is increased past dipole reorientation in PNZT-02, the phase transformation is indicated as the onset of nonlinear response in the σ_1-ε_v plot. However, the volume reduction at the phase transformation in UC tests is not as significant as in HC or in CSD tests. The volume change in UC tests at phase transformation is the net result of volume reduction caused by phase transformation superimposed on the dilatation of the specimen caused by shear stress.

Effects of Temperatures in UC

The summary of uniaxial compression tests at different temperatures is shown in Table 4. As indicated in Table 4 and Figure 14, the phenomenon of dipole reorientation is not evident in the stress-strain plot at low temperatures. Our uniaxial compression tests based on stress-strain (ε_a, ε_l and ε_v) results show that at low temperatures (-55°C) dipole reorientation starting at lower stress levels than phase transformation is effectively suppressed and only the phase transformation occurs. We could not observe any nonlinear behavior in ε_a and ε_l at lower stress levels before the phase transformation occurring at σ_{T1}^{U}.

Figure 15 shows the P-wave velocity normalized to the baseline P-wave velocity measured for the unstrained PNZT ceramic. Although acoustic velocity measurements during UC tests (Appendix B) did not show consistent data, with a significant amount of scatter in them, it appears that the effect of dipole reorientation in P-wave velocity can be seen in test PNZT-01 at an ambient temperature of 25°C. At low stress level below 200 MPa of axial stress, P-wave velocity begins to decrease as observed by Fritz (1979). At high stress level above 200 MPa of axial stress, P-wave velocity starts to increase due to FE to AFE phase transformation.

Table 4. Summary of phase transformation and dipole reorientation in "chem-prep" PNZT-HF803 under uniaxial compression (UC).

Specimen no.	Temperature (ºC)	$\sigma_{1,f}$ (MPa)	σ_{R1}^{U} (MPa)	σ_{T1}^{U} (MPa)	σ_{Tm}^{U} (MPa)	P_{T1}^{H} (MPa)	P_{T2}^{H} (MPa)
PNZT-04	-55	754	NA	160	53	189	196
PNZT-71	-55	703	NA	160	53	189	196
PNZT-01	25	536	110	250	83	248	259
PNZT-02	25	527	90	250	83	248	259
PNZT-06	75	495	85	310	103	291	329

$\sigma_{1,f}$ - major principal stress corresponding to the peak of the stress-strain curve
σ_{R1}^{U} - major principal stress required for dipole reorientation under uniaxial compression
σ_{T1}^{U} - major principal stress required for FE to AFE phase transformation under uniaxial compression
σ_{Tm}^{U} - mean stress required for FE to AFE phase transformation under uniaxial compression
P_{T1}^{H} - pressure for initiation of FE to AFE phase transformation under hydrostatic compression
P_{T2}^{H} - pressure for completion of FE to AFE phase transformation under hydrostatic compression

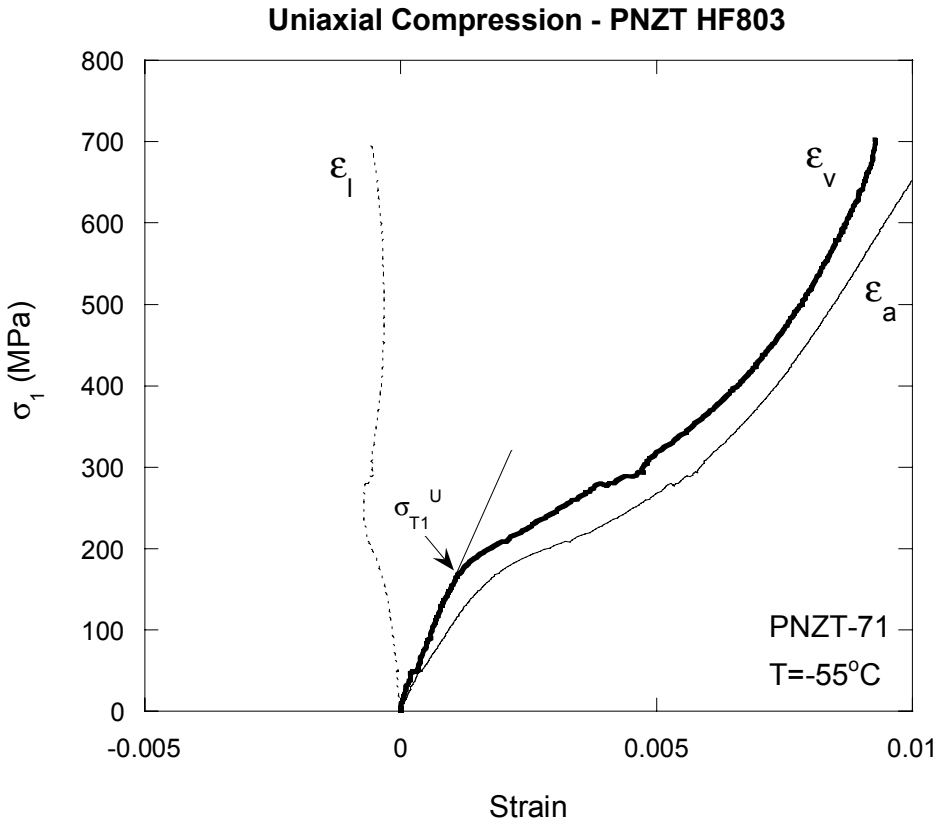

Figure 14. Typical uniaxial compression experiment on unpoled PNZT-HF803 ceramic at low temperature (-55°C). The major principal stress, σ_1, is plotted against axial (ε_a), lateral (ε_l) and volumetric (ε_v) strains, respectively. The major principal stress for the initiation of FE to AFE phase transformation under uniaxial compression is indicated as σ_{T1}^{U}.

For the PNZT-04 specimen at a low temperature (-55°C), it appears that dipole reorientation is suppressed and the P-wave velocity remains unchanged until FE to AFE phase transformation. The other three tests display discontinuous responses in P-wave velocity with large scatter. Therefore, the significance in test results is in doubt (see Appendix B). A definite conclusion in dipole reorientation may be obtained if the uncertainties in identifying the P-wave arrival time are reduced.

Figure 16 shows variation of failure strength, phase transformation, and dipole reorientation with respect to temperature in uniaxial compression of "chem-prep" PNZT-HF803. The uniaxial compressive strength of PNZT-HF803 ranges from 500 to 750 MPa and is inversely related with temperature.

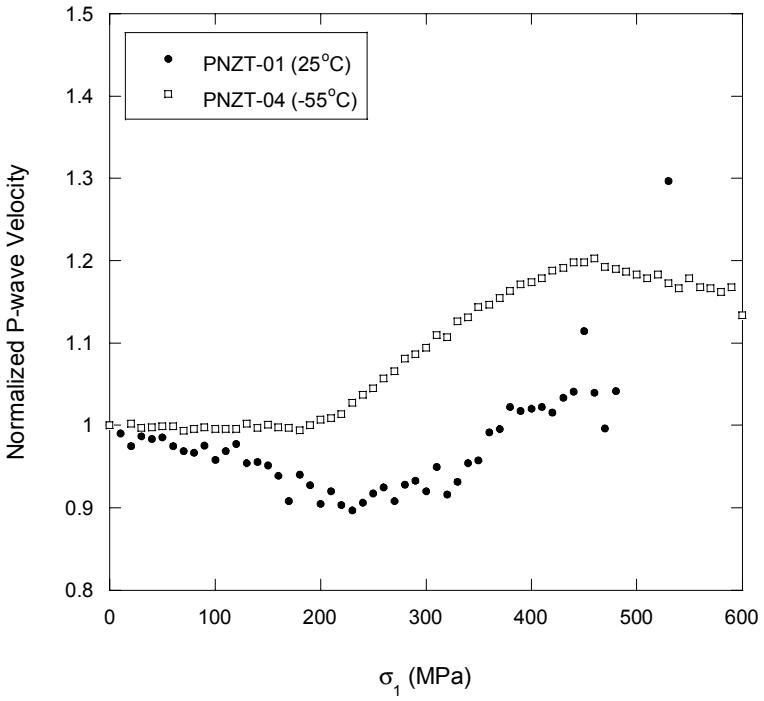

Figure 15. Changes in P-wave velocities with respect to applied axial stress (σ_1) on unpoled PNZT-HF803 ceramic. The normalized P-wave velocities are the ratio of P-wave velocities to the baseline P-wave velocities measured at zero stress.

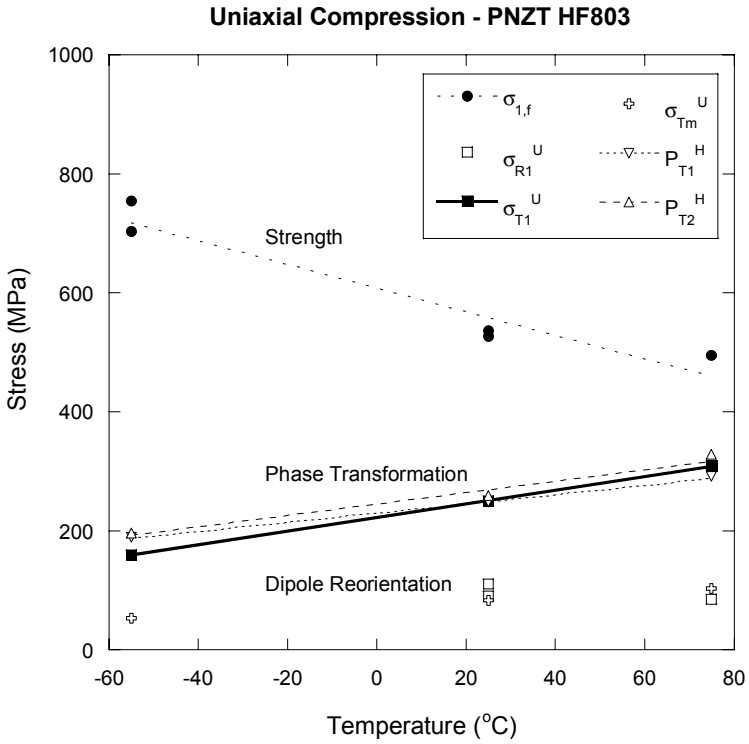

Figure 16. Effects of temperature on failure strength ($\sigma_{1,\,f}$), phase transformation pressures (P_{T1}^{H}, P_{T2}^{H}, σ_{T1}^{U} and σ_{Tm}^{U}) and dipole reorientation pressures (σ_{R1}^{U}) in uniaxial compression of "chem-prep" PNZT-HF803.

Maximum Stress Criterion for Phase Transformation

For comparison purposes, the pressures required for the onset (P_{T1}^{H}) and completion (P_{T2}^{H}) of FE to AFE phase transformation under hydrostatic compression are shown in the same plot. Also the mean stresses ($\sigma_{Tm}^{U} = \sigma_{T1}^{U}/3$) for phase transformation under uniaxial compression are plotted. The maximum principal stress at phase transformation (σ_{T1}^{U}) under uniaxial compression is in good accordance with the phase transformation pressures (P_{T1}^{H} and P_{T2}^{H}) under hydrostatic compression. Figure 16 also shows that the stress at dipole reorientation (σ_{R1}^{U}), is approximately one third of the phase transformation stress (σ_{T1}^{U}). Therefore, σ_{R1}^{U} is in general agreement with σ_{Tm}^{U}.

Figures 17 and 18 compare σ-ε_v behavior in uniaxial compression on unpoled PNZT and hydrostatic compression on the same material at the same temperature. In Figure 17 the phase transformation data are plotted in terms of the mean stress and the volumetric strain. In Figure 18, the same data are plotted in terms of the major principal stress and the volumetric strain. The comparison of these two plots clearly demonstrates that in unpoled "chem-prep" PNZT-HF803, the phase transformation occurs when the major principal stress equals the hydrostatic pressure at which the transformation otherwise takes place.

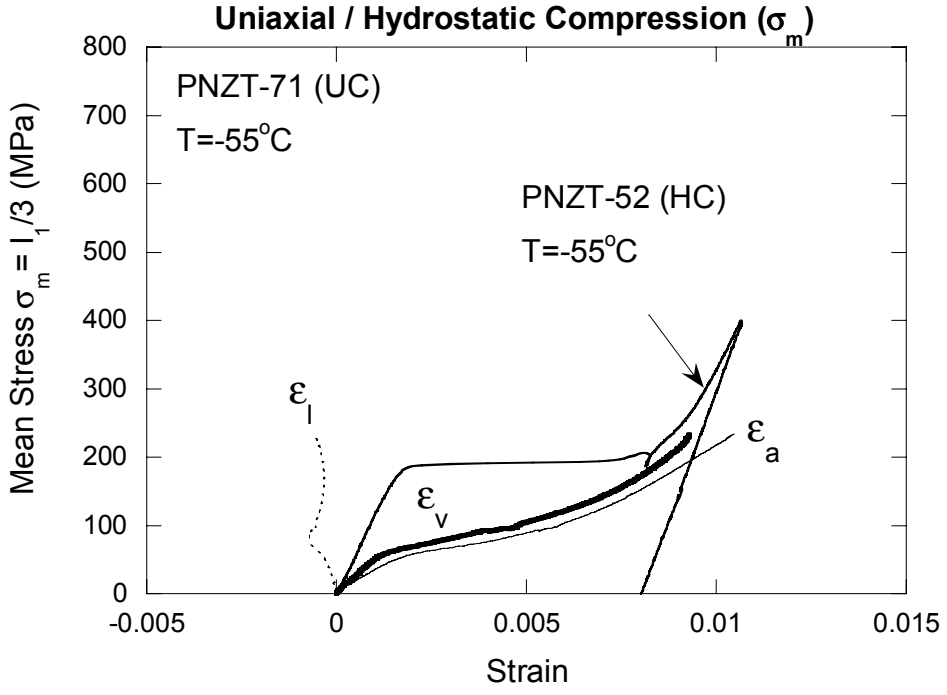

Figure 17. Comparison of stress-strain plots obtained during uniaxial compression with hydrostatic compression experiment using mean stress ($\sigma_m = \frac{\sigma_1 + \sigma_2 + \sigma_3}{3}$). Shown are the axial strain (ε_a); lateral strain (ε_l); and volumetric strain (ε_v).

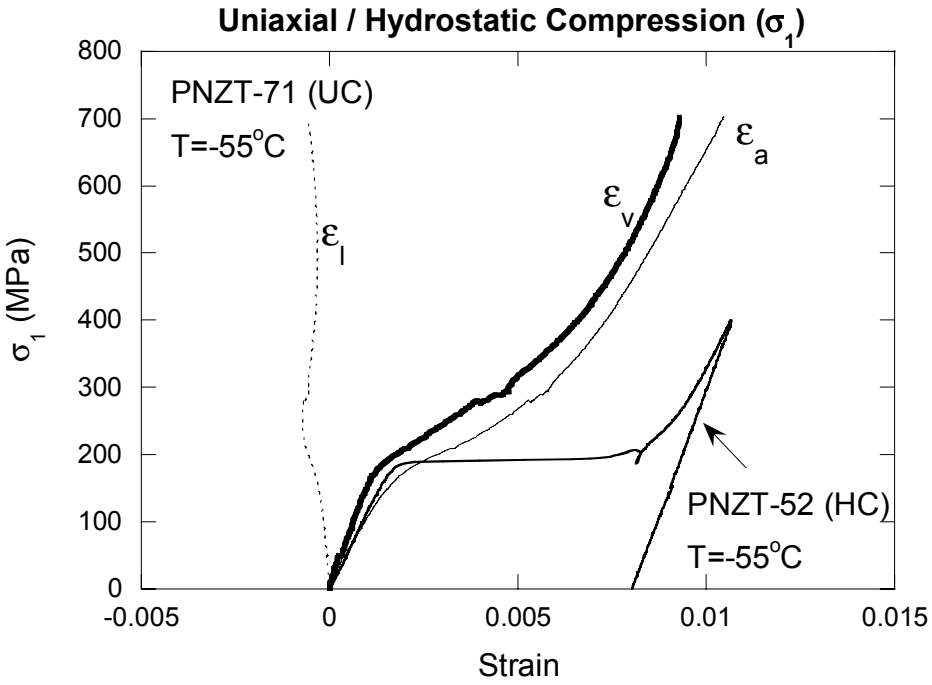

Figure 18. Comparison of stress-strain plots obtained during uniaxial compression with hydrostatic compression experiment using major principal stress (σ_1). Shown are the axial strain (ε_a); lateral strain (ε_l); and volumetric strain (ε_v).

3.3 Constant stress difference tests

Constant-Stress-Difference experiments (Zeuch *et al*., 1999a) were conducted to characterize the effects of nonhydrostatic loading on the phase transformation of the "chem-prep" PNZT-HF803. The sample preparation procedures and test equipment for the CSD tests were identical to those used for the HC and UC tests described in previous Chapter 2.4.

The typical loading path for the CSD test is shown in Figure 19. The PNZT-10 specimen was hydrostatically compressed to 69 MPa which is far below the expected transformation pressure under hydrostatic loading (P_T^{HC}~250 MPa). While the confining pressure, σ_3, was kept constant at 69 MPa, the axial stress, σ_1, was increased to 119 MPa creating the stress difference ($\sigma_d = \sigma_1 - \sigma_3 = 50$ MPa). Then, both σ_1 and σ_3 were increased simultaneously at the same rate. As the mean stress was increased without changing the shear stress, the maximum principal stress reached the critical stress for FE to AFE phase transformation under CSD condition.

Appendix C shows the loading paths used for the CSD testing. Four levels of stress differences 50, 100, 150, and 200 MPa were used. Figures 20 and 21 show the complete σ_3-ε and σ_1-ε plots obtained from PNZT-10 experiment, respectively. As in the HC tests, the phase transformation is indicated as the abrupt increase in strains approximately at 250 MPa of σ_1 or 200 MPa of σ_3.

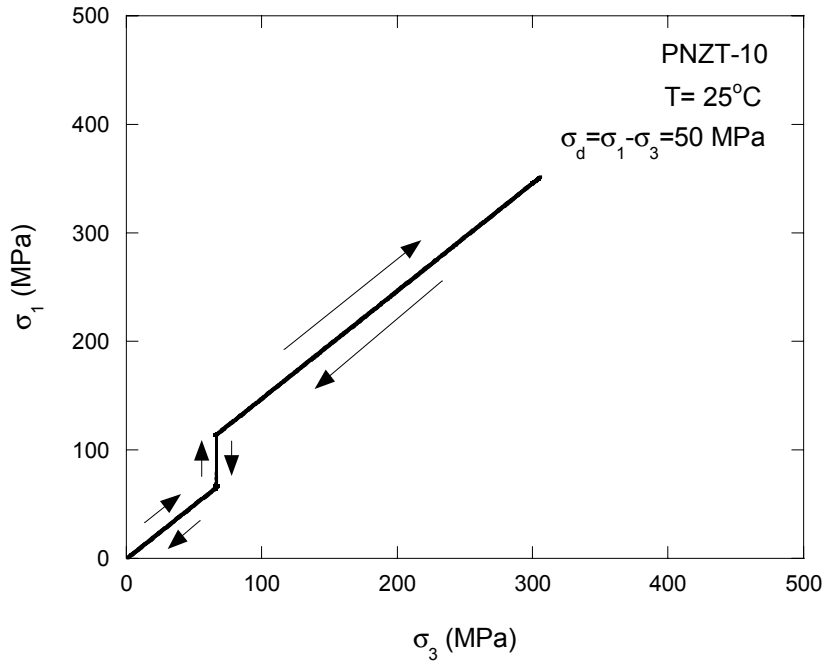

Figure 19. A loading path obtained from the Constant Stress Difference test PNZT-10 conducted at 50 MPa stress difference ($\sigma_d=\sigma_1-\sigma_3$). The unloading path is not discernable from the loading path since the unloading path exactly followed over the loading path in reverse direction.

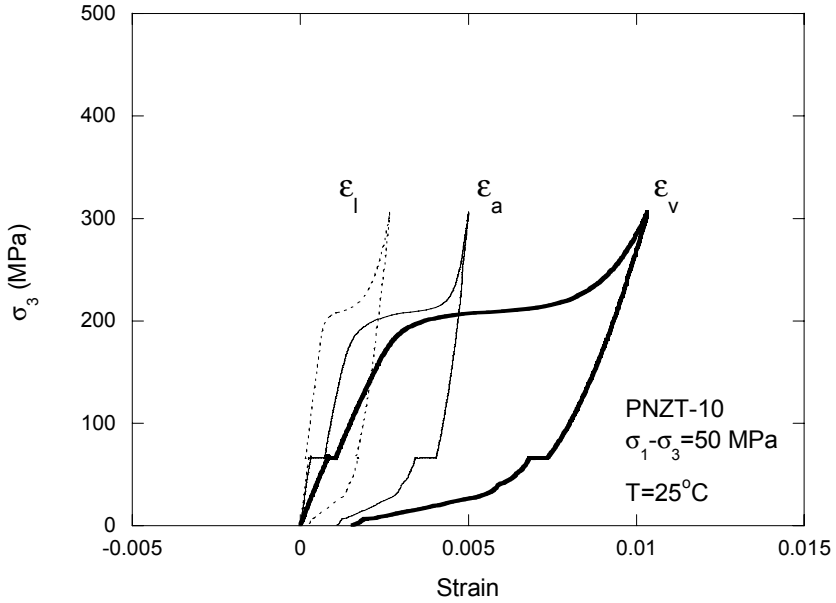

Figure 20. Minimum compressive stress (σ_3)-strain responses of the unpoled "chem-prep" PNZT-HF803 under CSD experiment. Initiation of phase transformation is represented by increase in axial (ε_a), lateral (ε_l), and volumetric (ε_v) strains around 200 MPa of σ_3.

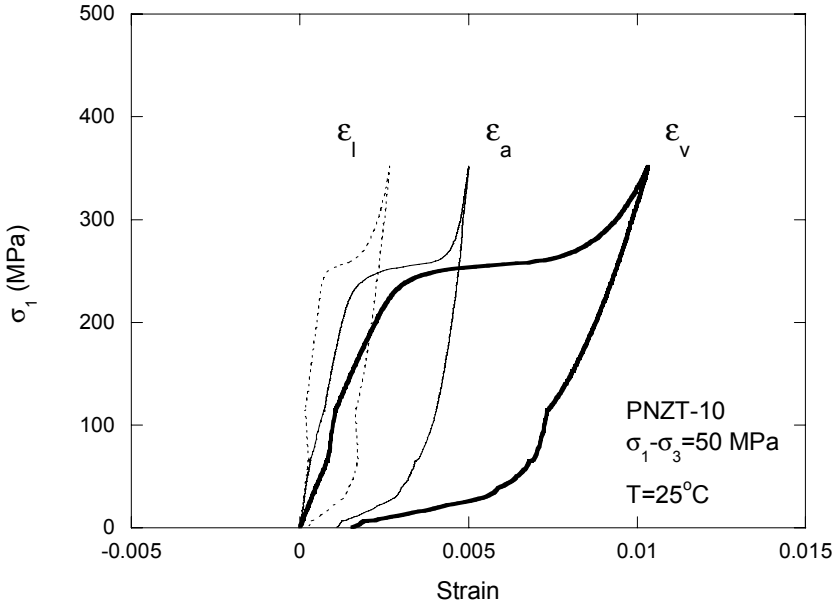

Figure 21. Maximum compressive stress (σ_1)-strain responses of the unpoled "chem-prep" PNZT-HF803 under CSD experiment. Initiation of phase transformation is represented by increase in axial (ε_a), lateral (ε_l), and volumetric (ε_v) strains around 250 MPa of σ_1.

In order to study the effects of temperature in the CSD testing, we conducted a series of CSD tests for the temperature range of -55 to 75°C. Figures 22, 23, and 24 show the mean stress-volumetric strain plots of the CSD testing conducted at three different levels of temperatures (low –55°C, ambient 25°C, and high 75°C), respectively. For each temperature group, a HC test ($\sigma_d = \sigma_1 - \sigma_3 = 0$) is also shown to compare with data obtained with the stress differences from 50 to 200 MPa. The results are summarized in Table 5 and Figures 22, 23, and 24.

A comparison of bulk moduli, K_F and K_A, obtained under identical temperature and σ_d condition shows that the scatters of K_F and K_A are large. This may indicates the amount of sample to sample variation of the phase mixture. The cause of sample to sample variations in bulk moduli is the subject of further investigation.

As in the HC tests, the phase transformation of the "chem-prep" PNZT-HF803 under CSD condition was identified as the sudden increase in volumetric strain of the specimen ranging from 0.3 to 0.8 %. At low temperature, the volumetric strain at phase transformation was about 0.8 %. The volumetric strain was slightly reduced to 0.7 % for ambient temperature. At high temperature, FE to AFE transition was gradual with indistinct onset of phase transformation. As a result, the range of corresponding volumetric strain reduction varied widely from 0.3 to 0.7 %.

At the low temperature bound (-55°C), FE to AFE phase transformation was permanent under set temperature condition. Even though the stresses on the specimen returned to the initial condition, the ceramic did not revert to FE phase. Figure 22 shows that approximately 0.75% of irreversible volumetric strain remained even after the specimen was completely

unloaded. However, at ambient temperature (25°C) and at the upper temperature bound (75°C), the FE to AFE phase transformation became reversible. Figures 23 and 24 show that an insignificant amount of permanent volumetric strain remained after the stresses were removed. As the stresses were reversed, the AFE to FE phase transformation occurred with a gradual decrease in volumetric strain.

Figure 25 shows the effect of temperature on the levels of critical stresses required for the phase transformation of the "chem-prep" PNZT-HF803 under CSD condition. Both the maximum stress (σ_{T1}^{CSD}) and the mean stress (σ_{Tm}^{CSD}) for FE to AFE phase transformation increased with temperature under CSD loading conditions. It also shows that the critical pressure, P_{T1}^{H}, for FE to AFE phase transformation under hydrostatic loading increased in parallel with σ_{T1}^{CSD} and σ_{Tm}^{CSD}. The results shown in Figure 25 clearly indicate that σ_{Tm}^{CSD} underestimates P_{T1}^{H}. The results also confirm the previous findings in uniaxial compression that transformation occurs when the maximum compressive stress reaches P_{T1}^{H} (Zeuch *et al*., 1999c).

If we assume that the transformation occurs when the maximum compressive stress reaches the hydrostatic pressure at which transformation would otherwise take place, then the mean stress, σ_{Tm}^{CSD}, at transformation can be represented as follows (Zeuch *et al*., 1999c):

$$\begin{aligned} \sigma_{Tm}^{CSD} &= \frac{(\sigma_{T1}^{CSD} + 2\sigma_3)}{3} \\ &= \frac{\sigma_{T1}^{CSD} + 2(\sigma_{T1}^{CSD} - \sigma_d)}{3} \\ &= \sigma_{T1}^{CSD} - \frac{2\sigma_d}{3} \end{aligned} \tag{10}$$

Equation 10 shows that the mean stress for transformation will be lowered by two-thirds of the increasing shear stress or stress difference from σ_{T1}^{CSD}. Under HC loading, σ_{T1}^{CSD} becomes same as P_{T1}^{H}, pressure required for FE to AFE phase transformation under HC loading. Figure 26 shows the effects of shear stress and temperature on the volumetric strain at the onset of phase transformation. Increasing the temperature from –55 to 75°C clearly increases the volumetric strain at the onset of transformation. Sometimes this phenomenon is described as retardation of transformation. Under set temperature conditions, increasing shear stress linearly decreases the volumetric strain required to trigger FE to AFE phase transformation.

Table 5. Summary of phase transformation in "chem-prep" PNZT-HF803 under Constant Stress Difference (CSD) loading.

Specimen no.	Temperature (° C)	σ_d	a_1 (MPa)	K_F (GPa)	a_2 (MPa)	K_{FA} (GPa)	a_3 (MPa)	K_A (GPa)	ε_{v1}^{CSD}	σ_{Tm1}^{CSD} (MPa)	ε_{v2}^{CSD}	σ_{Tm2}^{CSD} (MPa)	$\varepsilon_{v2}^{CSD} - \varepsilon_{v1}^{CSD}$	$\Delta\sigma_m$ (MPa)	σ_{T1}^{CSD}	σ_{T2}^{CSD}
PNZT-52	-55	0	-1.0	115.3	187.2	1.0	-1220.4	151.7	0.0016	189	0.0093	196	0.0077	8	189	196
PNZT-22	-55	50	0.2	101.5	160.0	2.1	-1089.6	140.9	0.0016	163	0.0090	179	0.0074	16	197	212
PNZT-25	-55	100	-0.8	125.0	123.9	5.8	-1364.8	176.1	0.0010	130	0.0087	175	0.0077	45	197	241
PNZT-08	-55	100	-4.4	144.0	124.3	7.0	-1342.2	176.8	0.0009	131	0.0086	185	0.0077	54	198	251
PNZT-27*	-55	150	1.3	106.0	122.8	-0.4	-1328.1	165.9	0.0011	122	0.0087	120	0.0076	-3	222	220
PNZT-28*	-55	150	-1.4	121.8	121.9	-0.2	-1229.4	158.6	0.0010	122	0.0085	120	0.0075	-1	222	220
PNZT-23*	-55	200	0.3	99.5	107.1	5.3	-1395.0	177.8	0.0011	113	0.0087	153	0.0076	40	246	286
PNZT-34	25	0	2.0	84.1	242.9	1.7	-769.0	108.8	0.0029	248	0.0095	259	0.0065	11	248	259
PNZT-17	25	50	4.1	72.8	206.4	3.1	-662.0	99.7	0.0029	215	0.0090	234	0.0061	19	249	268
PNZT-10	25	50	2.5	75.9	207.8	2.9	-749.4	103.4	0.0028	216	0.0095	236	0.0067	20	249	269
PNZT-18	25	100	13.8	78.3	164.5	10.4	-738.7	113.5	0.0022	188	0.0088	255	0.0065	68	254	322
PNZT-15	25	100	6.4	75.8	176.3	7.3	-720.4	103.3	0.0025	194	0.0093	245	0.0069	50	261	311
PNZT-19	25	150	3.7	64.9	148.0	10.1	-736.8	100.3	0.0026	175	0.0098	247	0.0072	72	275	347
PNZT-07	25	150	0.2	93.3	132.2	13.2	-500.1	91.8	0.0016	154	0.0080	238	0.0064	84	254	338
PNZT-11*	25	200	1.6	61.4	51.0	23.6	-535.6	91.0	0.0013	82	0.0087	256	0.0074	174	215	389
PNZT-60	75	0	-1.5	87.4	271.9	5.8	-679.4	101.0	0.0033	291	0.0100	329	0.0066	38	291	329
PNZT-30	75	50	1.2	80.2	250.9	8.1	-512.5	101.0	0.0035	279	0.0082	317	0.0048	38	312	351
PNZT-35	75	50	7.8	69.8	218.3	15.8	-140.6	66.0	0.0039	280	0.0071	331	0.0033	51	313	364
PNZT-31	75	100	-1.6	86.7	230.4	12.6	-400.5	83.2	0.0031	270	0.0089	343	0.0058	73	336	409
PNZT-32	75	150	1.0	85.4	188.8	20.2	-383.0	88.9	0.0029	247	0.0083	357	0.0054	110	347	457
PNZT-36**	75	150	5.4	78.4	71.6	47.3	-199.7	100.1	0.0021	172	0.0051	315	0.0030	142	272	415
PNZT-33**	75	200	1.9	87.3	177.5	21.0	-444.0	86.4	0.0027	233	0.0095	377	0.0068	144	367	510

K_F - bulk modulus in FE (ferroelectric) phase; K_A - bulk modulus in AFE (antiferroelectric) phase; K_{FA} - tangent modulus in transition from FE to AFE phase

a_1- extrapolated pressure corresponding to zero volumetric strain in FE phase

a_2 - extrapolated pressure corresponding to zero volumetric strain during transition from FE to AFE phase

a_3 - extrapolated pressure corresponding to zero volumetric strain in AFE phase

σ_{Tm1}^{CSD} –mean stress at initiation of FE to AFE phase transformation under CSD compression

σ_{Tm2}^{CSD} –mean stress at completion of FE to AFE phase transformation under CSD compression

ε_{v1}^{CSD} - volumetric strain at σ_{Tm1}^{CSD}; ε_{v2}^{CSD} - volumetric strain at σ_{Tm2}^{CSD}

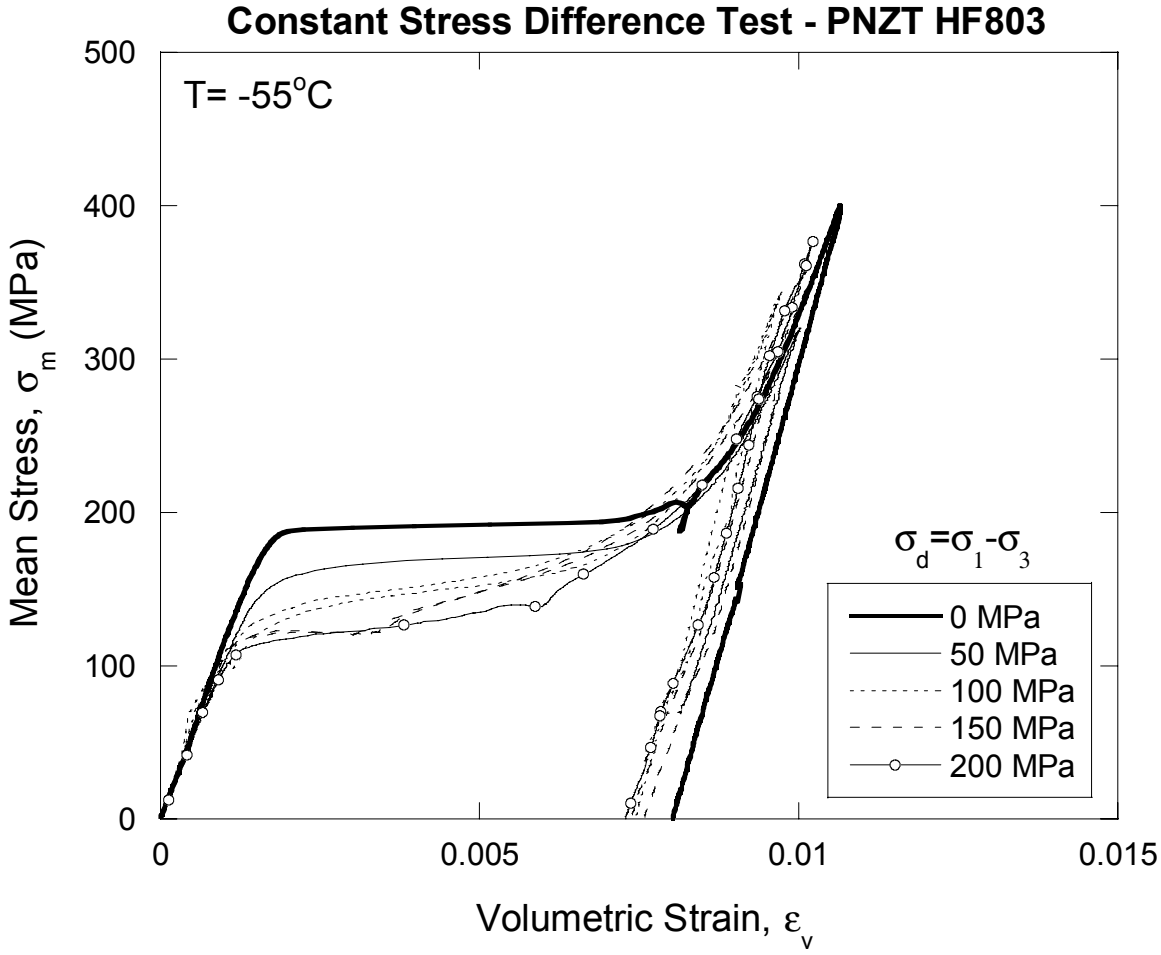

Figure 22. Mean Stress-volumetric strain plot during constant stress difference test for unpoled "chem-prep" PNZT-HF803 ceramic at low temperature (-55°C).

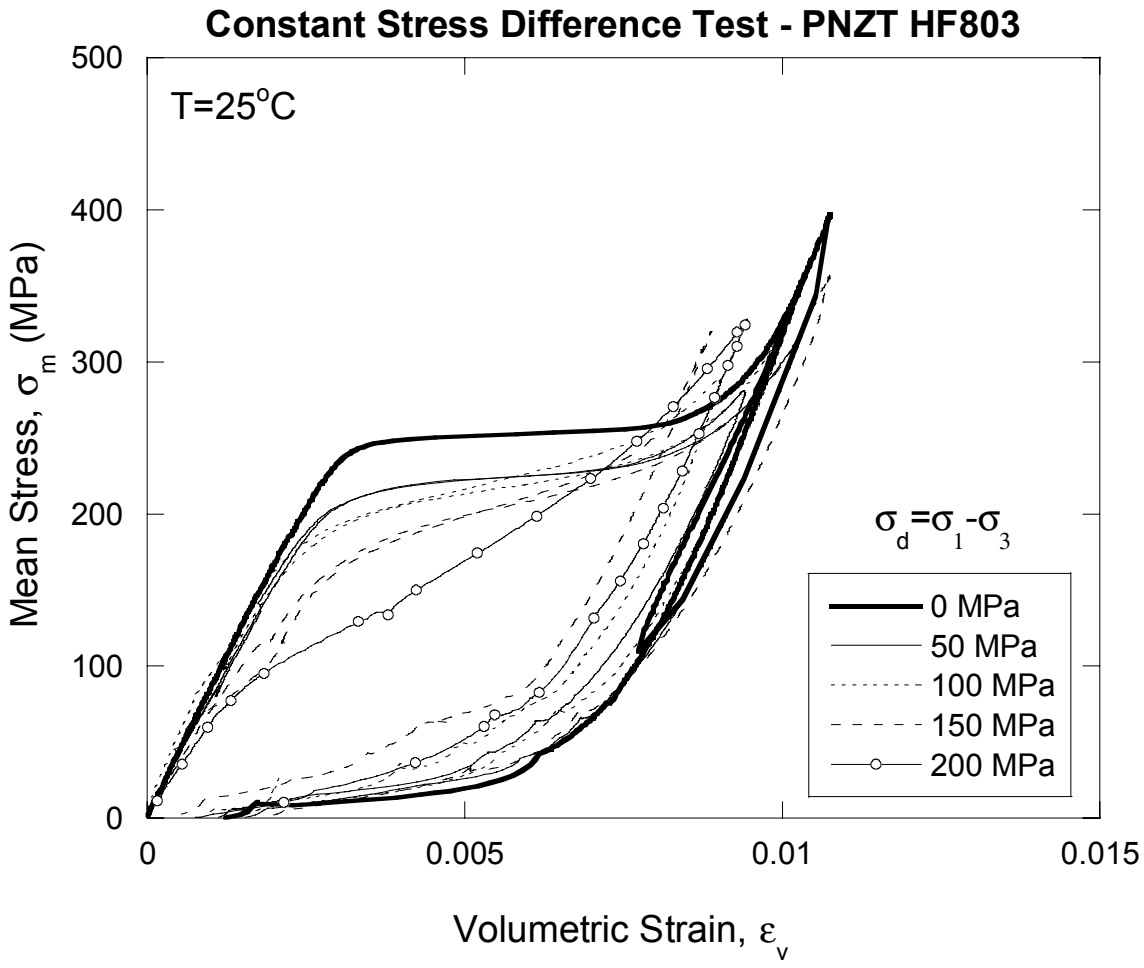

Figure 23. Mean Stress-volumetric strain plot during constant stress difference test for unpoled "chem-prep" PNZT-HF803 ceramic at ambient temperature (25°C).

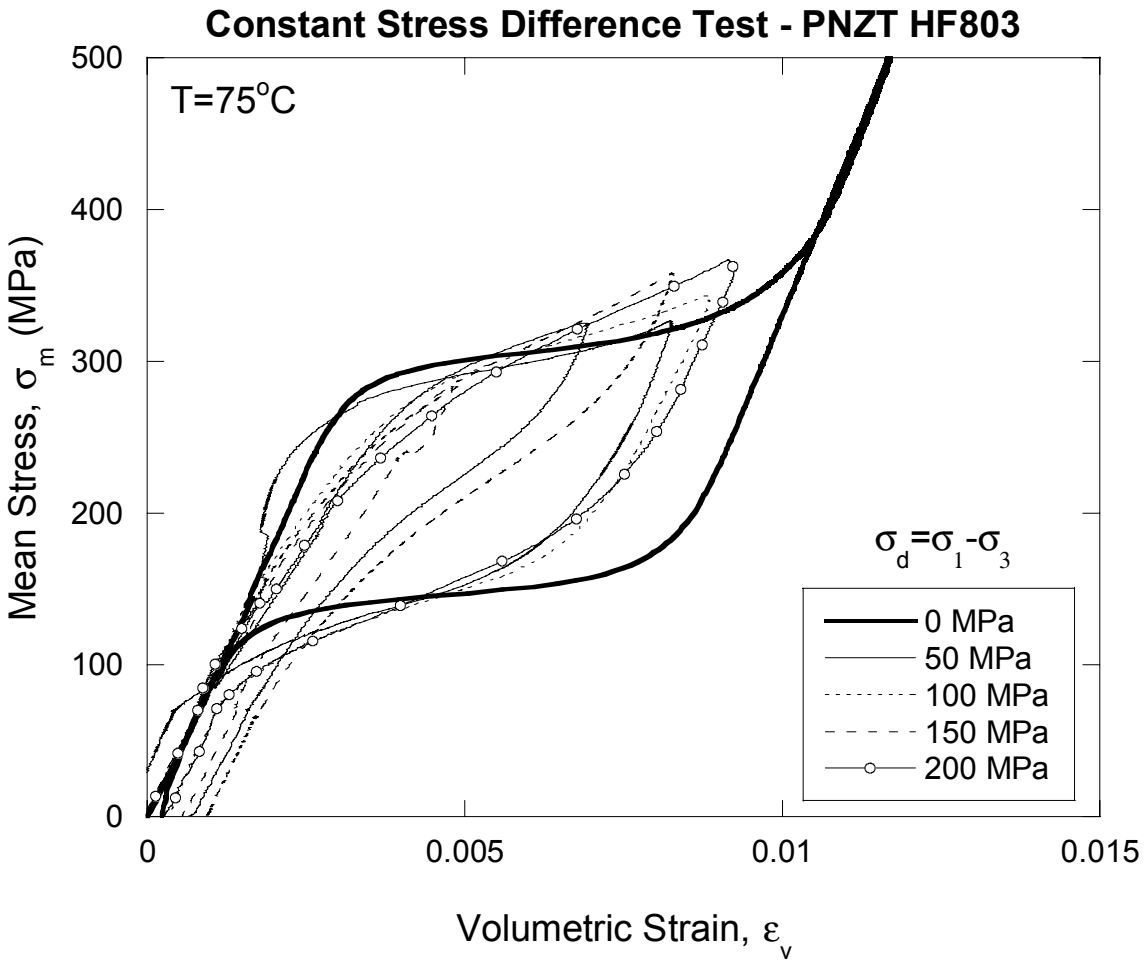

Figure 24. Mean Stress-volumetric strain plot during constant stress difference test for unpoled "chem-prep" PNZT-HF803 ceramic at elevated temperature (75°C).

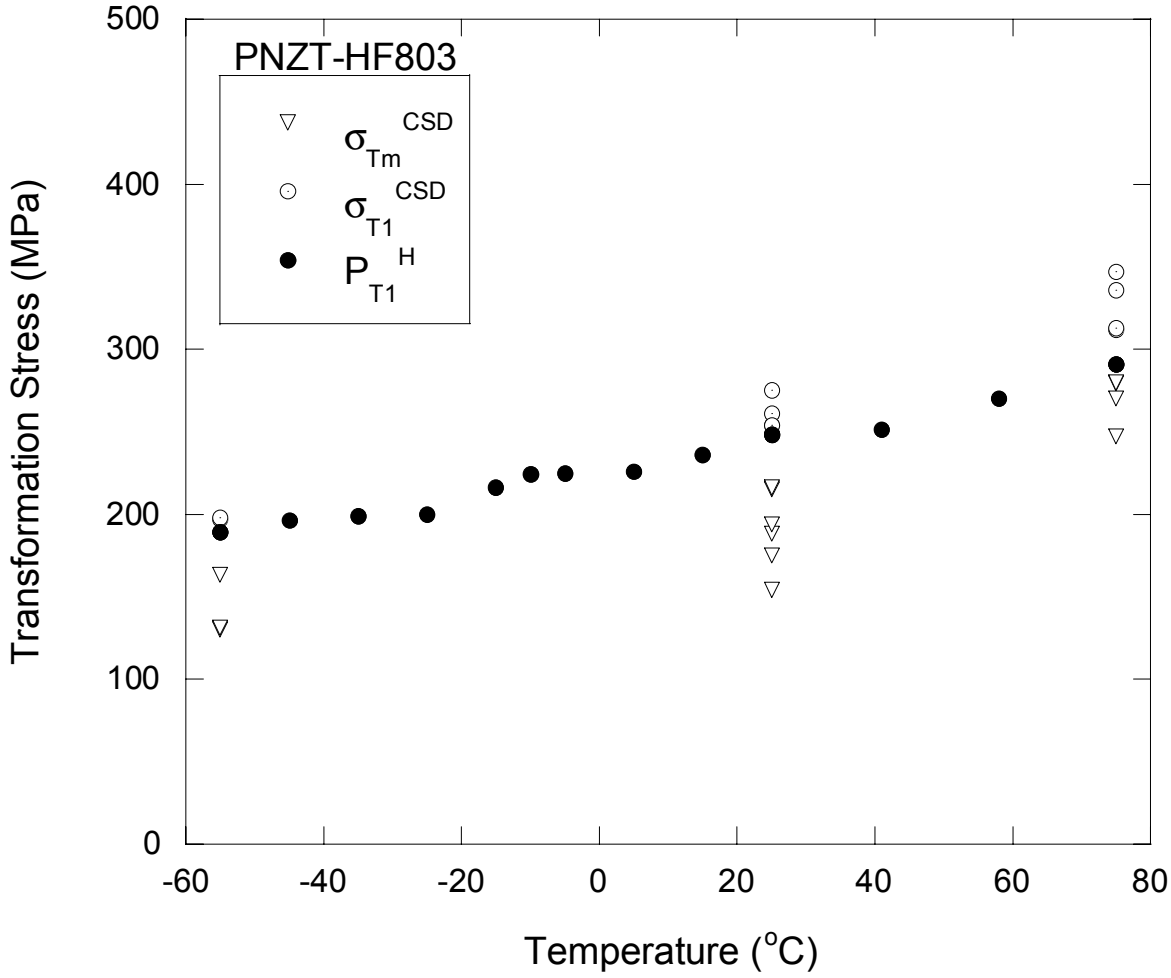

Figure 25. Critical stresses required for phase transformation of "chem-prep" PNZT- HF803 under constant stress difference (circles) and hydrostatic (diamonds) tests. σ_{Tm}^{CSD} is the mean stress for FE to AFE phase transformation under CSD loading, σ_{T1}^{CSD} is the maximum compressive stress for FE to AFE phase transformation under CSD loading, and P_{T1}^{H} is the pressure for FE to AFE phase transformation under hydrostatic loading

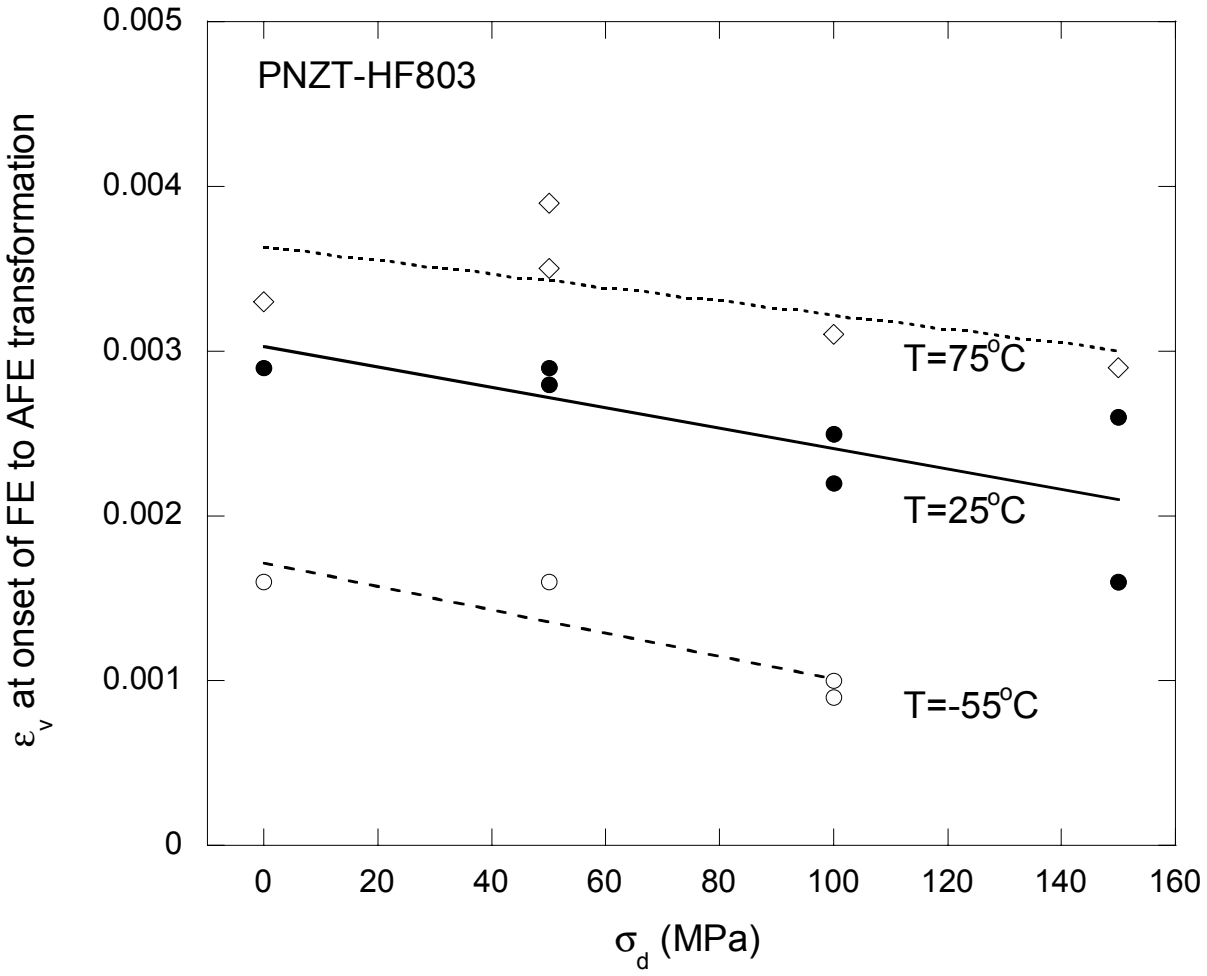

Figure 26. Effects of shear stress and temperature on the volumetric strain, ε_v, of "chem-prep" PNZT at the onset of phase transformation.

4. Conclusions

The specimens of unpoled "chem-prep" PNZT ceramic from batch HF803 were tested under quasi-static conditions using hydrostatic, uniaxial compression, and constant strain difference loading paths. The stress-strain behavior during the FE to AFE phase transformation was investigated within the temperature range (-55 to 75°C). The results from the laboratory experiments can be summarized as follows:

- The phase transformation occurs when the maximum compressive stress equals the hydrostatic pressure at which the transformation otherwise takes place.

- The pressure required for the onset (P_{T1}^{H}) of the FE to AFE phase transformation under hydrostatic loading is represented by the following linear relationship:

$$P_{T1}^{H}\ (\text{MPa}) = 227 + 0.76\ T\ (°\text{C})$$

- The curved structure in the phase boundary is shown in the completion (P_{T2}^{H}) of the FE to AFE phase transformation. The relationship is:

$$P_{T2}^{H}\ (\text{MPa}) = 232 + 0.83\ T + 0.0047\ T^2$$

- The volumetric strain for the onset of the FE to AFE transformation increases with temperature.

- The uniaxial compression test shows the isovolumetric phenomenon of dipole reorientation (or domain switching).

- At the low temperature bound (-55°C), the FE to AFE phase transformation is permanent and irreversible. However, at the upper temperature bound (75°C), the phase transformation is reversible from AFE to FE as the stress causing the phase transformation is removed.

- Under constant temperature conditions, increasing shear stress lowers the mean stress and the volumetric strain required to trigger phase transformation.

References

Bauer, F., K. Vollrath, Y. Fetiveau and L. Eyraud (1976). Ferroelectric ceramics: application to mechanical energy conversion under shock compression. Ferroelectrics, **10**: 61-64.

Brannon, R. M., Montgomery, S. T., Aidun, J. B., and A. C. Robinson (2001), *Macro- and meso-scale modeling of PZT ferroelectric ceramics*, 12th Biennial International Conference of the American Physical Society Topical Group on Shock Compression on Condensed Matter, Atlanta, GA.

Fritz, I. J., and J. D. Keck (1978). *Pressure-temperature phase diagrams for several modified lead zirconate ceramics.* J. Phys. Chem. Solids, **39**: 1163-1167.

Fritz, I. J. (1979). *Stress effects in two modified lead zirconate titanate ferroelectric ceramics*. J. Appl. Phys. **50** (8): 5265-5271.

Lee, M. Y., Fossum A. and D. R. Bronowski (2002). *Material testing and constitutive modeling of Alaskan frozen soil,* Eos Trans. AGU, 83(47), Fall Meeting Suppl., Abstract T22B-1147.

Lysne, P. C. and C. M. Percival (1975). Electric energy generation by shock compression of ferroelectric ceramics: normal-mode response of PZT 95/5. J. Appl. Phys., **46**: 1519-1526.

Samara, G., L. V. Hansen, J. A. Voigt and B. A. Tuttle (1999). *Dielectric properties and Pressure-Temperature Phase Diagram for Chem-Prep PZT 95/5.* In: Samara, G. (ed), *Neutron Generator Supporting Research: A Progress Report on Selected Topics.* Rept. No. SAND99-3084, Sandia National Laboratories, Albuquerque, NM, pp. 23-29.

B. A. Tuttle, J. A. Voigt, T. W. Scofield, P. Yang, D. H. Zeuch and M. A. Rodriguez (2000). *Dielectric properties and depoling characteristics of Pb ($Zr_{0.95}Ti_{0.05}$) O_3 based ceramics: near-critical grain size behavior.* Proceedings of the 9th U.S.-Japan Seminar on Dielectric and Piezoelectric Ceramics, Okinawa, Japan, November 2-5, pp. 55-58.

Voigt, J. A., Sipola, D. L., Ewsuk, K. G., Tuttle, B. A., Moore, R. H., Montoya, T. V., and M.A. Anderson (1998). *Solution Synthesis and Processing of PZT Materials for Neutron Generator Applications*, Rept. No. SAND98-2750, Sandia National Laboratories, Albuquerque, NM.

Voigt, J.A., D. L. Sipola, B. A. Tuttle, and M. T. Anderson (1999). *Nonaqueous solution synthesis process for preparing oxide powders of lead zirconate titanate and related materials*.U.S. Patent 5,908,802.

Yang, P. (2003) Personal communication.

Zeuch, D. H., S. T. Montgomery and D. J.Holcomb (1999a). *The effects of nonhydrostatic stress and applied electric field on the electromechanical behavior of poled lead zirconate titanate 95/5-2Nb ceramic during the ferroelectric to antiferroelectric polymorphic transformation.* J. Mater. Res., **14**: 1814-1827.

Zeuch, D. H., S. T. Montgomery, J. B. Aidun and J. M. Grazier (1999b). *Uniaxial Compression Experiments at Low Temperature on PZT 95/5-2Nb Ceramic.* In: Samara, G. (ed), *Neutron Generator Supporting Research: A Progress Report on Selected Topics.* Rept. No. SAND99-3084, Sandia National Laboratories, Albuquerque, NM, pp. 17-23.

Zeuch, D. H., S. T. Montgomery, D. J. Holcomb, J. M. Grazier and L. W. Carlson (1999c). *Uniaxial compression experiments on PZT 95/5-2Nb ceramic: evidence for an orientation-dependent "maximum compressive stress" criterion for onset of the* $F_{R1} \rightarrow A_O$ *polymorphic phase transformation.* Rept. No. SAND99-0077, Sandia National Laboratories, Albuquerque, NM.

Zeuch, D. H., S. T. Montgomery, L. W. Carlson, and J. M. Grazier (1999d). *Failure surfaces and related mechanical properties for poled and unpoled PZT 95/5-2Nb voltage bar ceramic.* Rept. No. SAND99-0635, Sandia National Laboratories, Albuquerque, NM.

Zeuch, D. H, Lee, M. Y., Costin, L. S., Wawersik, W. R., Grazier, J. M., Bronowski, D. R., and R. D. Hardy (1999d). *A high-pressure, low-temperature triaxial test apparatus*. International Mechanical Engineering Congress & Exposition of the ASME. Nashville, TN.

APPENDIX A

Hydrostatic Compression (HC) Test Plots for PNZT-HF803 (ε_v-volumetric strain and T-temperature)

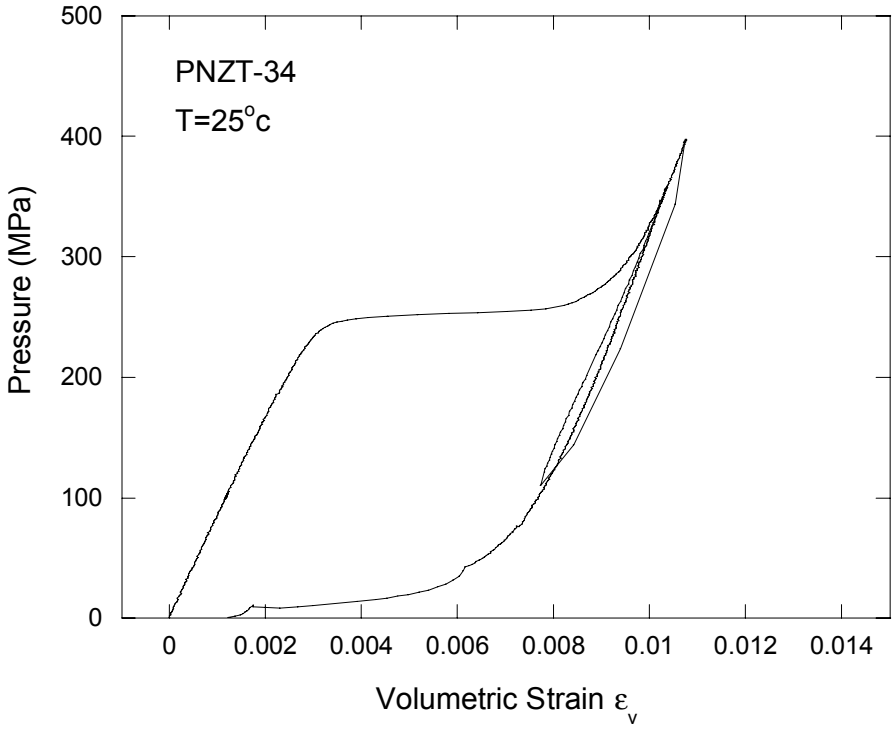
PNZT-34
T=25°c
Pressure (MPa)
Volumetric Strain ε_v
0
100
200
300
400
500
0
0.002
0.004
0.006
0.008
0.01
0.012
0.014

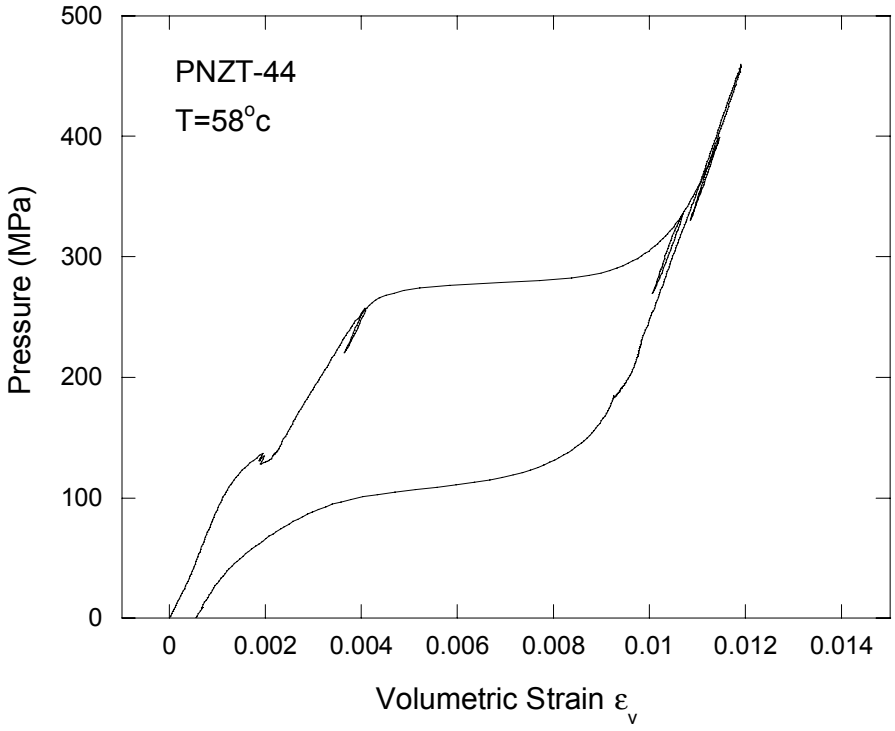
PNZT-44
T=58°c
Pressure (MPa)
Volumetric Strain ε_v
0
100
200
300
400
500
0
0.002
0.004
0.006
0.008
0.01
0.012
0.014

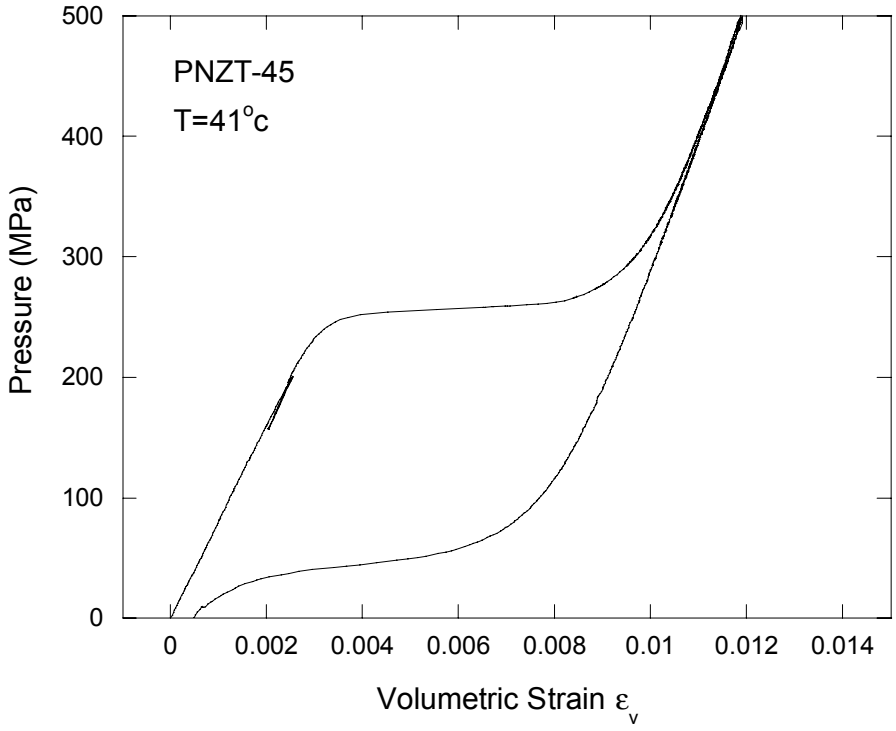
PNZT-45
T=41°c
Pressure (MPa)
Volumetric Strain ε_v
0
100
200
300
400
500
0
0.002
0.004
0.006
0.008
0.01
0.012
0.014

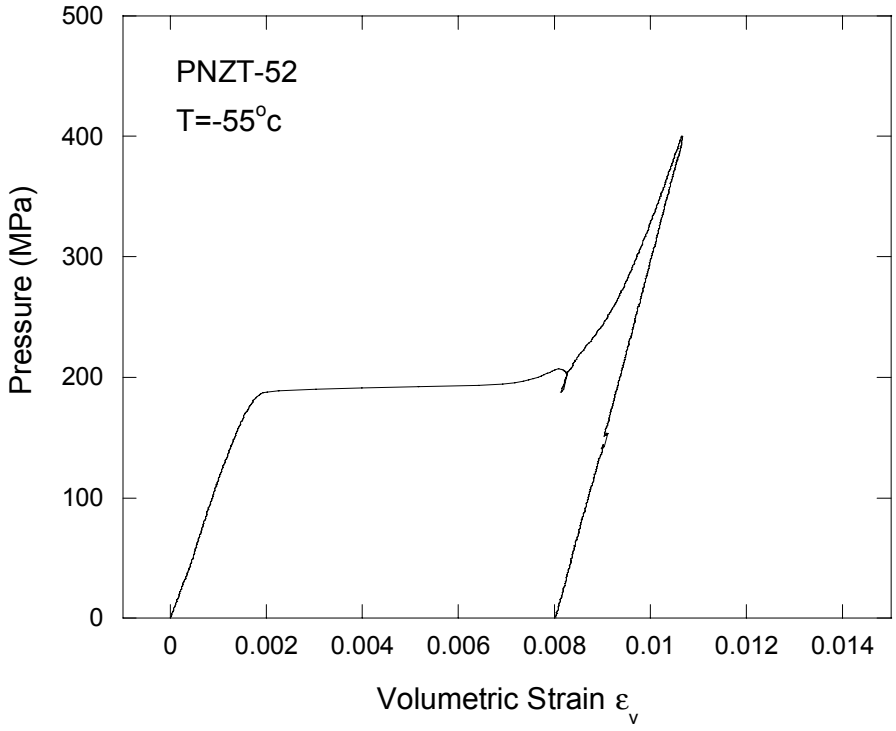
PNZT-52
T=-55°c
Pressure (MPa)
Volumetric Strain ε_v
0
100
200
300
400
500
0
0.002
0.004
0.006
0.008
0.01
0.012
0.014

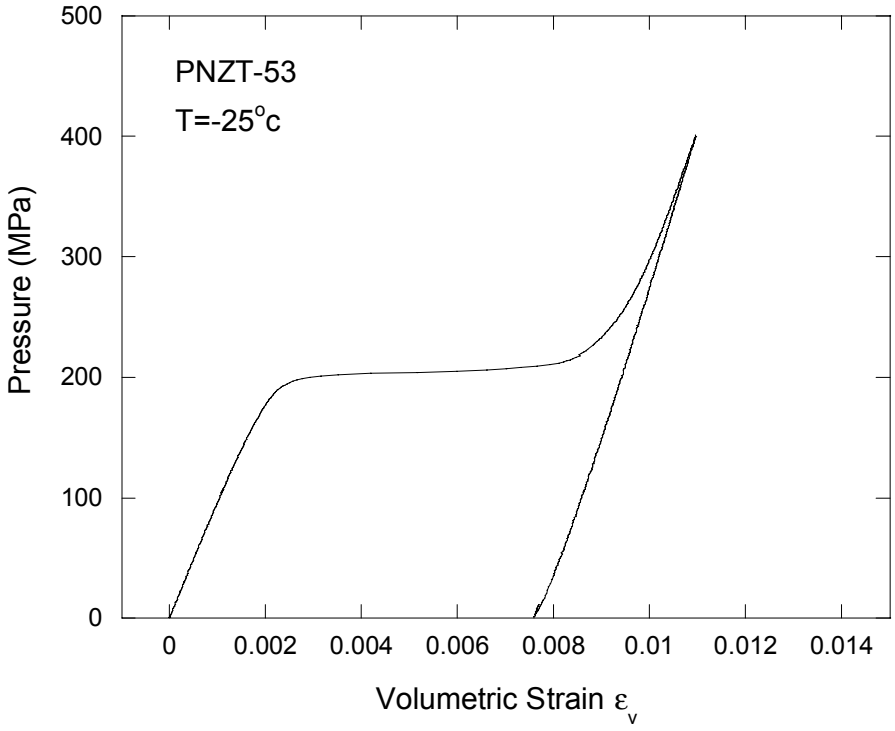
PNZT-53
T=-25°c
Pressure (MPa)
Volumetric Strain ε_v
0
100
200
300
400
500
0
0.002
0.004
0.006
0.008
0.01
0.012
0.014

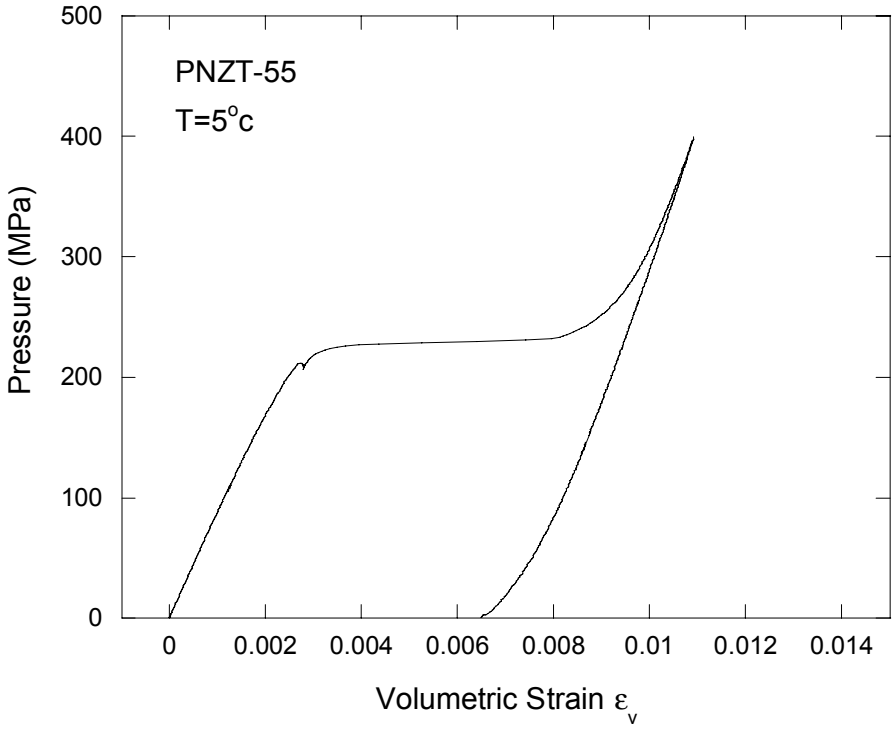
PNZT-55
T=5°c
Pressure (MPa)
Volumetric Strain ε_v
0
100
200
300
400
500
0
0.002
0.004
0.006
0.008
0.01
0.012
0.014

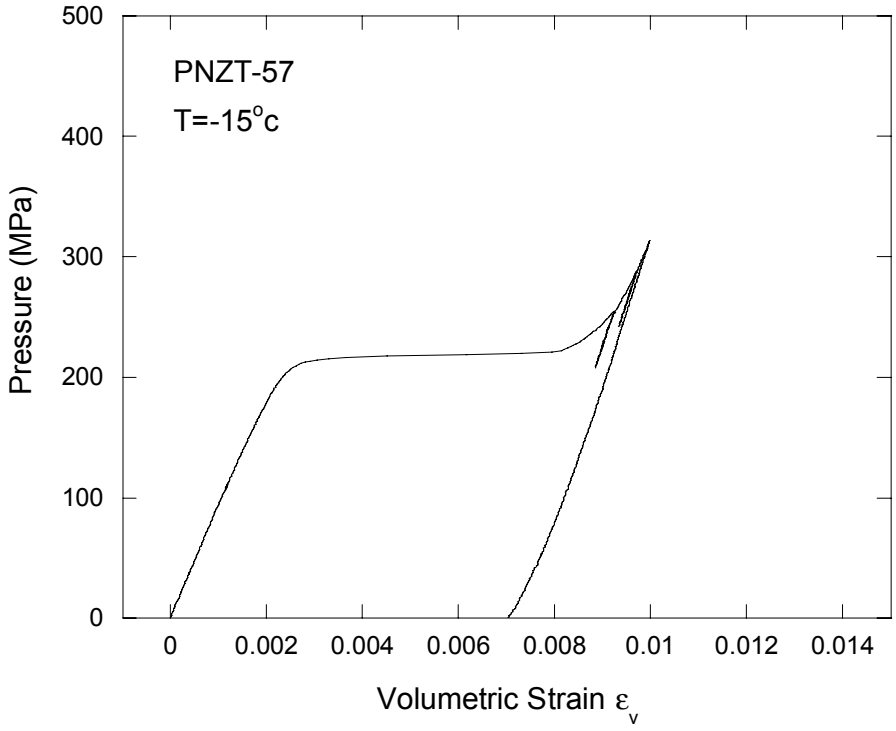
PNZT-57
T=-15°c
Pressure (MPa)
Volumetric Strain ε_v
0
100
200
300
400
500
0
0.002
0.004
0.006
0.008
0.01
0.012
0.014

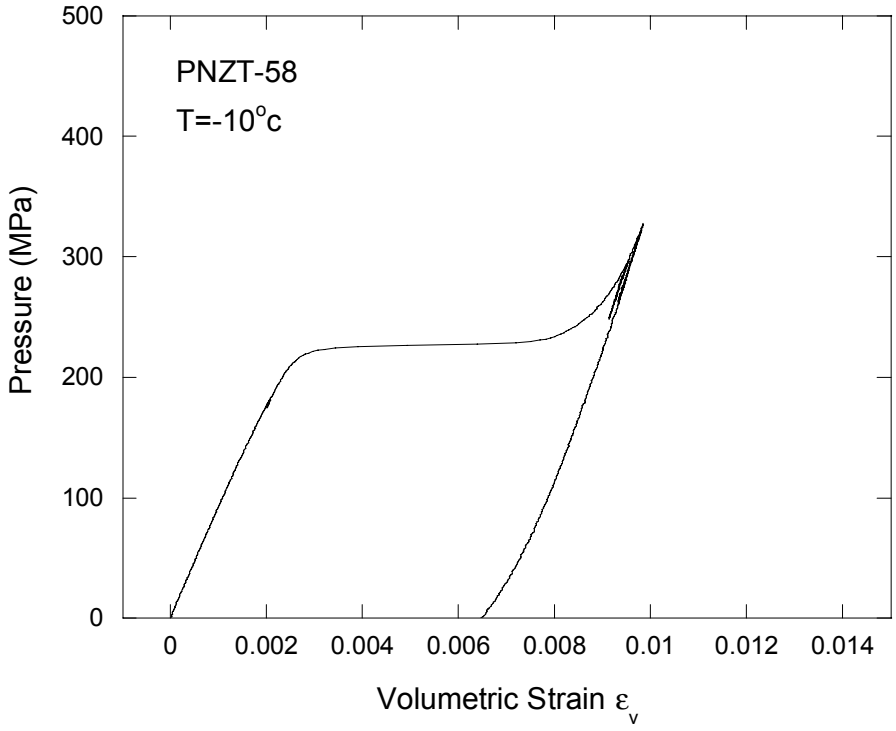
PNZT-58
T=-10°c
Pressure (MPa)
Volumetric Strain ε_v
0
100
200
300
400
500
0
0.002
0.004
0.006
0.008
0.01
0.012
0.014

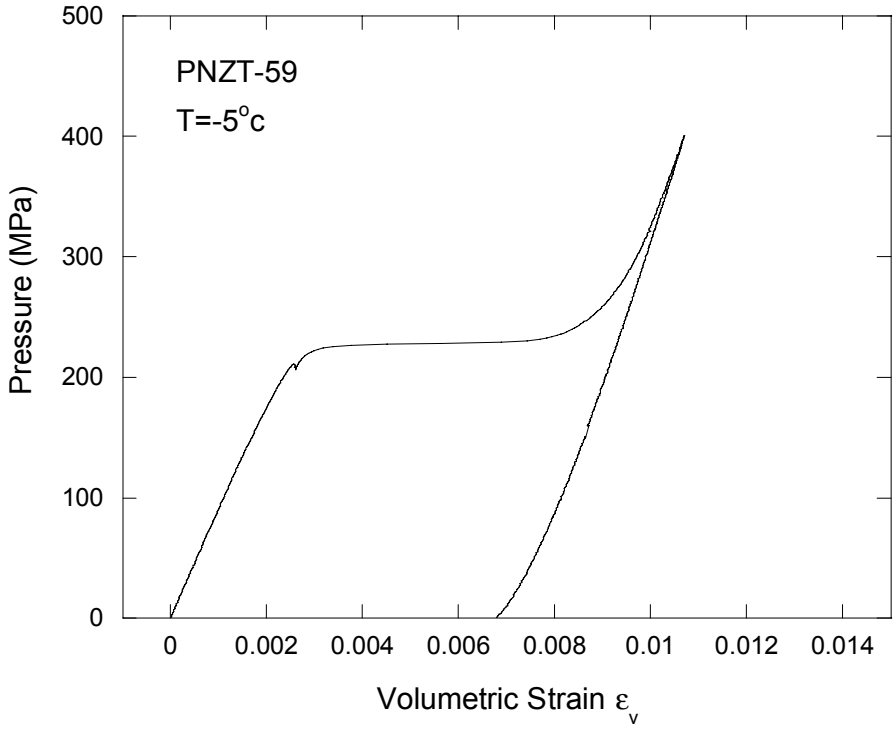
PNZT-59
T=-5°c
Pressure (MPa)
Volumetric Strain ε_v
0
100
200
300
400
500
0
0.002
0.004
0.006
0.008
0.01
0.012
0.014

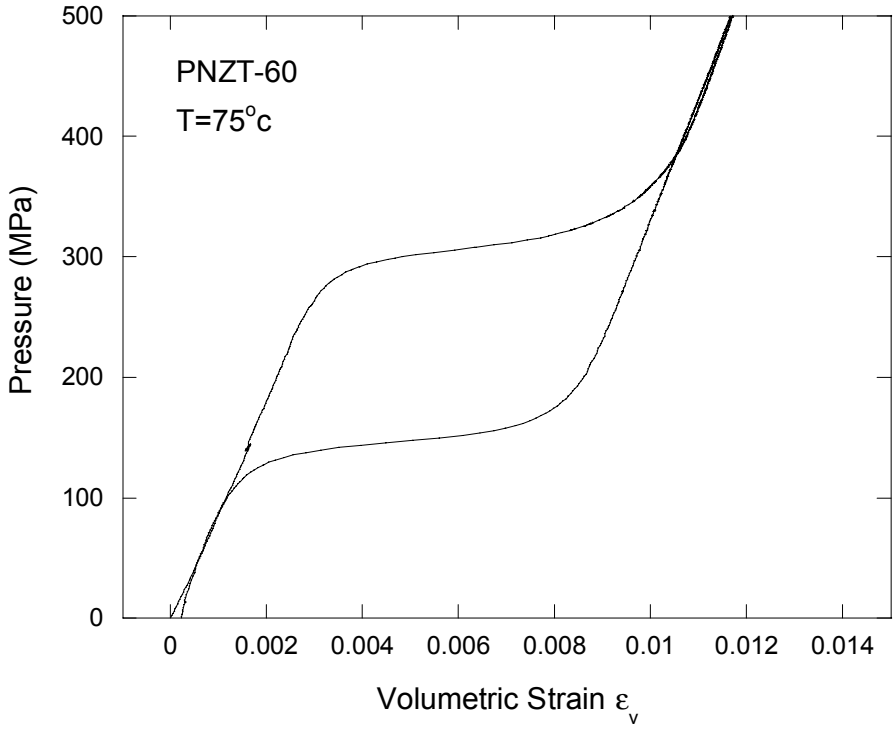
PNZT-60
T=75°c
Pressure (MPa)
Volumetric Strain ε_v
0
100
200
300
400
500
0
0.002
0.004
0.006
0.008
0.01
0.012
0.014

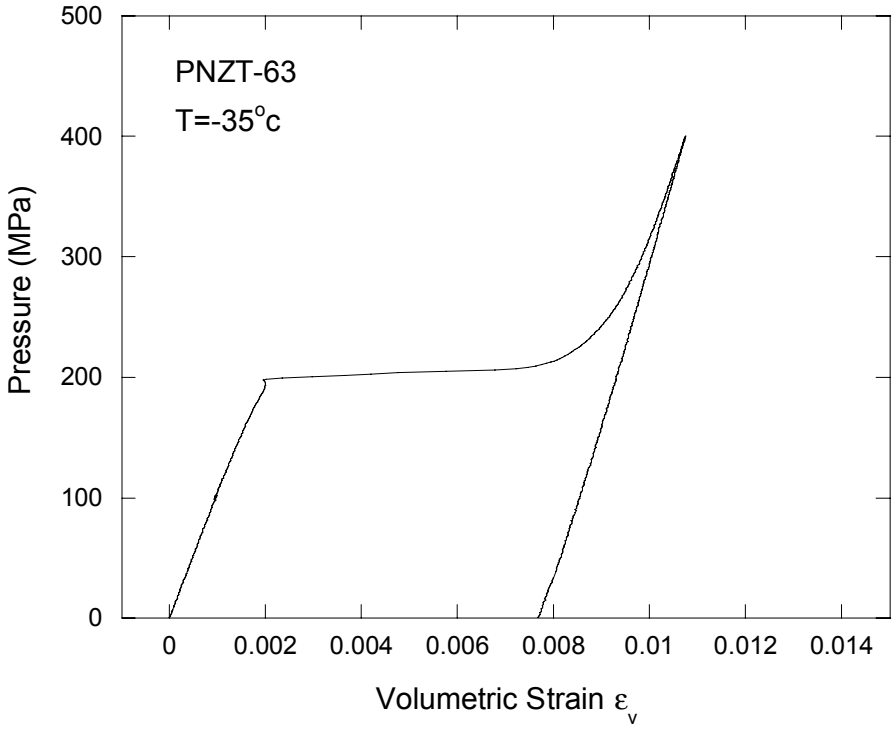
PNZT-63
T=-35°c
Pressure (MPa)
Volumetric Strain ε_v
500
400
300
200
100
0
0
0.002
0.004
0.006
0.008
0.01
0.012
0.014

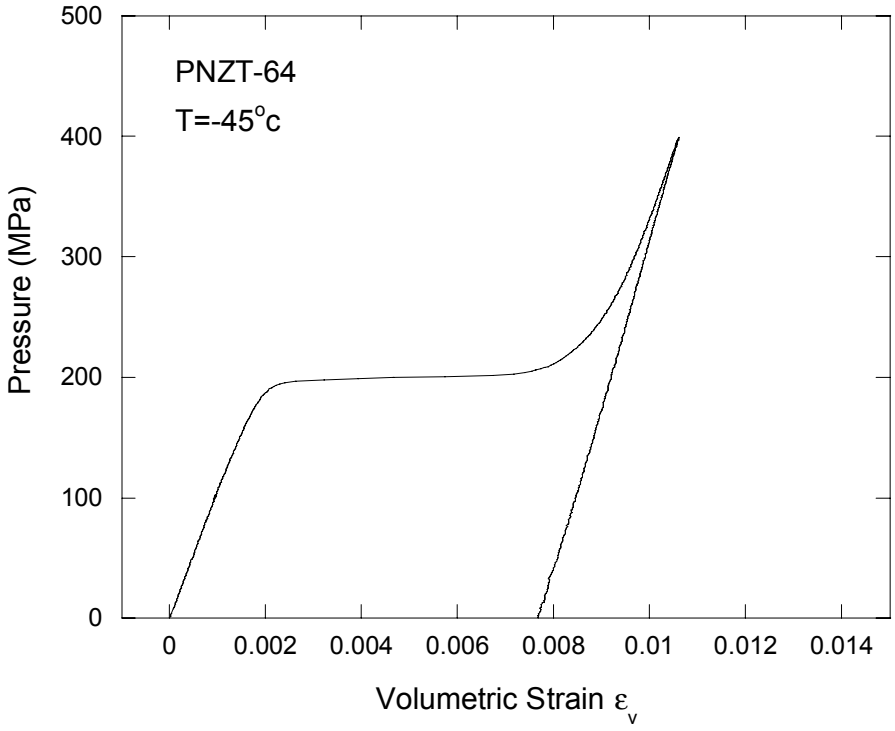
PNZT-64
T=-45°c
Pressure (MPa)
Volumetric Strain ε_v
500
400
300
200
100
0
0
0.002
0.004
0.006
0.008
0.01
0.012
0.014

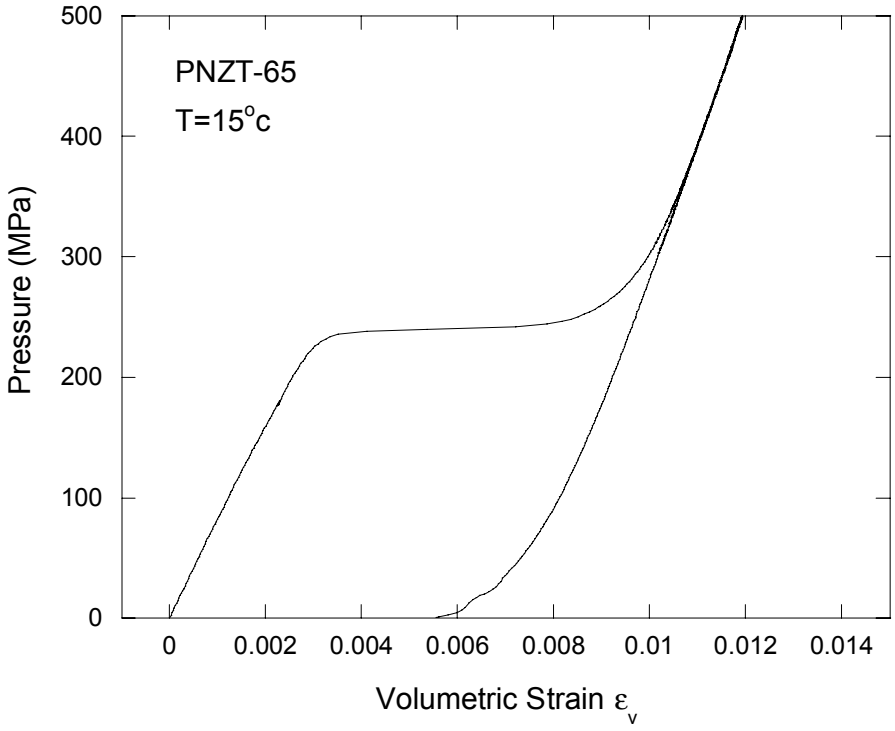
PNZT-65
T=15°c
Pressure (MPa)
500
400
300
200
100
0
0
0.002
0.004
0.006
0.008
0.01
0.012
0.014
Volumetric Strain ε_v

APPENDIX B

Uniaxial Compression (UC) Test Plots for PNZT-HF803 (σ_1-axial stress, ε_a-axial strain, ε_l-lateral strain, ε_v-volumetric strain and T-temperature)

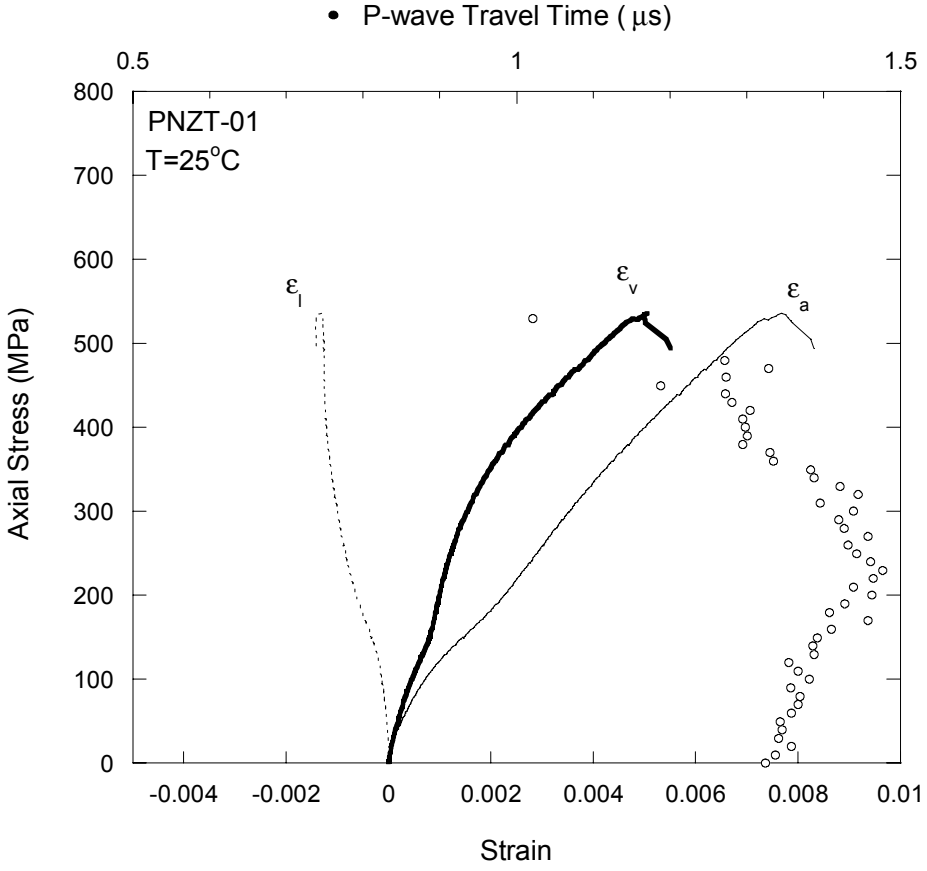
• P-wave Travel Time (μs)
0.5
1
1.5
PNZT-01
T=25°C
ε_l
ε_v
ε_a
Axial Stress (MPa)
800
700
600
500
400
300
200
100
0
-0.004
-0.002
0
0.002
0.004
0.006
0.008
0.01
Strain

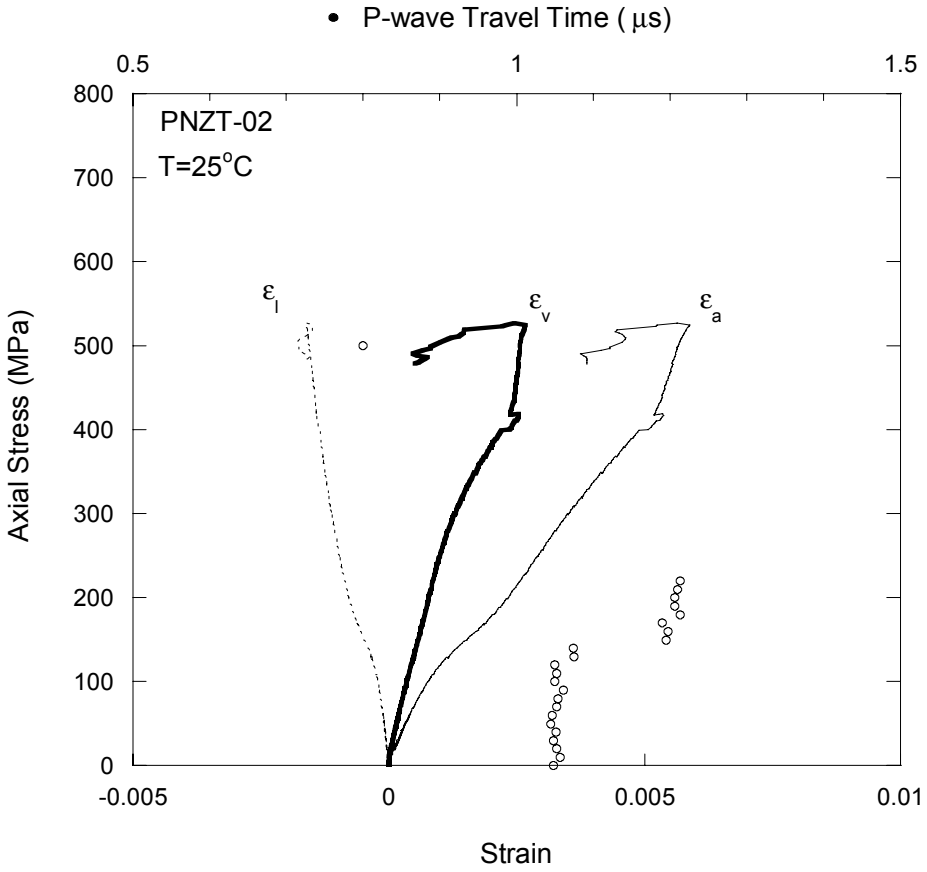
• P-wave Travel Time (μs)
0.5
1
1.5
PNZT-02
T=25°C
ε_l
ε_v
ε_a
Axial Stress (MPa)
800
700
600
500
400
300
200
100
0
-0.005
0
0.005
0.01
Strain

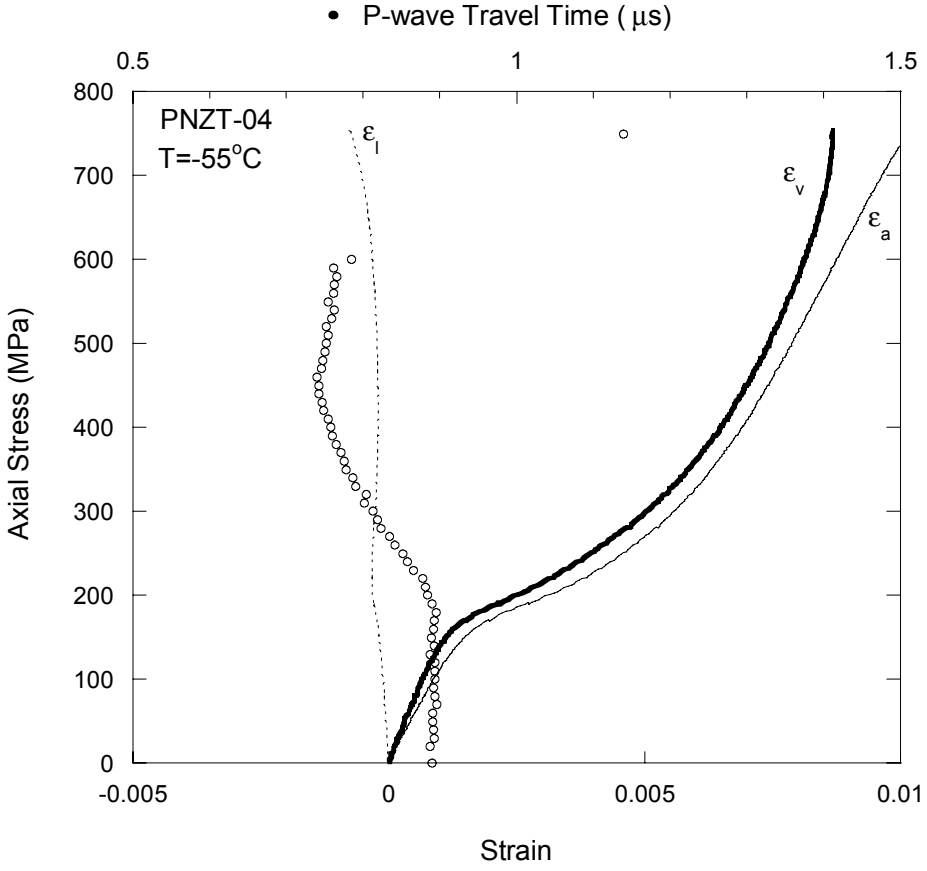
• P-wave Travel Time (μs)
0.5
1
1.5
800
700
600
500
400
300
200
100
0
PNZT-04
T=-55°C
ε_l
ε_v
ε_a
Axial Stress (MPa)
-0.005
0
0.005
0.01
Strain

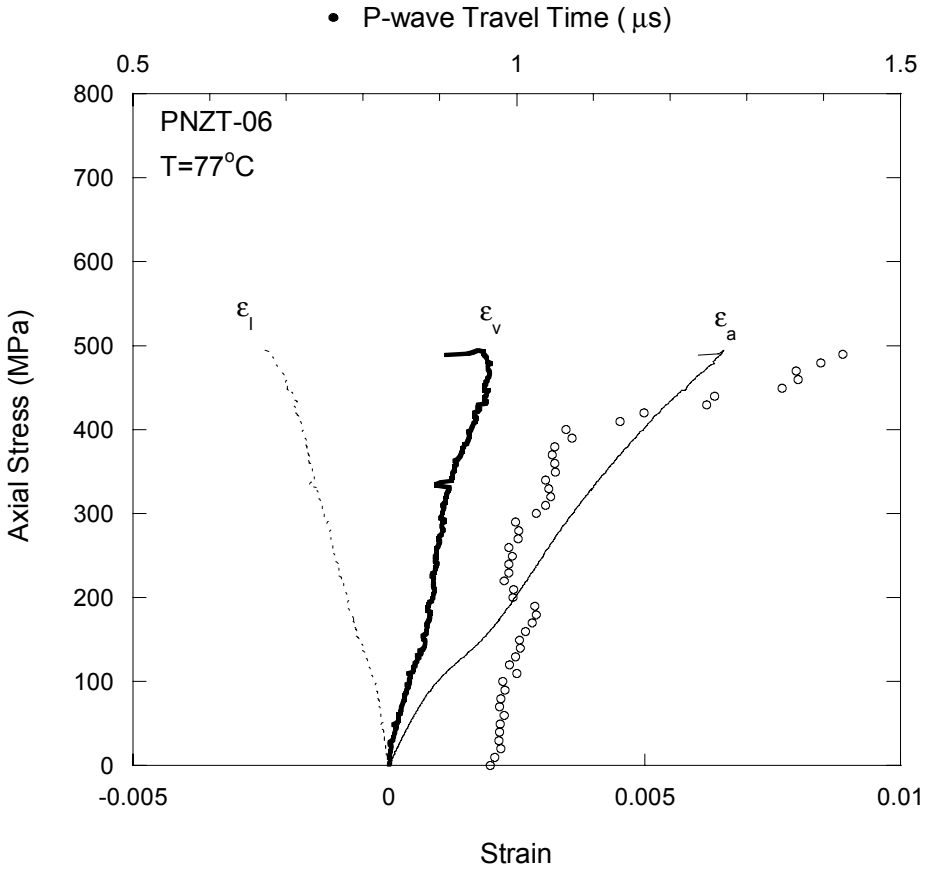
• P-wave Travel Time (μs)
0.5
1
1.5
800
700
600
500
400
300
200
100
0
PNZT-06
T=77°C
ε_l
ε_v
ε_a
Axial Stress (MPa)
-0.005
0
0.005
0.01
Strain

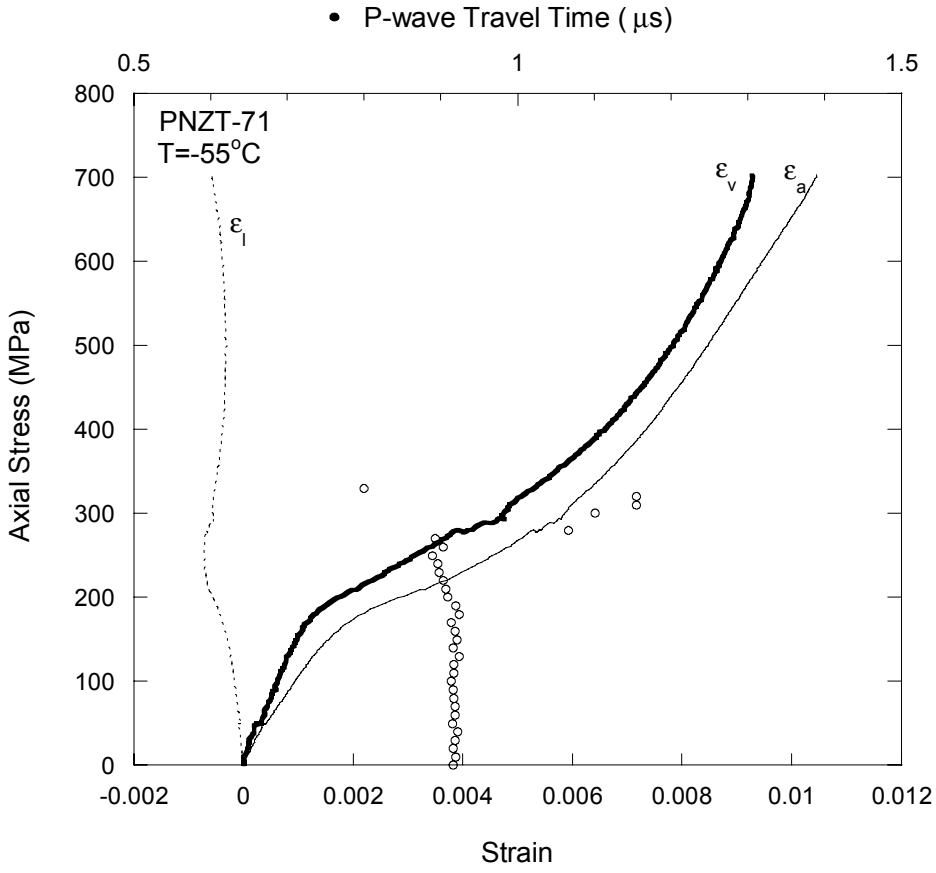
• P-wave Travel Time (μs)
0.5
1
1.5
800
700
600
500
400
300
200
100
0
PNZT-71
T=-55°C
ε_v
ε_a
ε_l
Axial Stress (MPa)
-0.002
0
0.002
0.004
0.006
0.008
0.01
0.012
Strain

APPENDIX C

Stress Paths and Stress-Strain Test Plots for Constant Stress Difference (CSD) Test for PNZT-HF803 (σ_1-axial stress, σ_3-confining stress, ε_a-axial strain, ε_l-lateral strain, ε_v-volumetric strain and T-temperature)

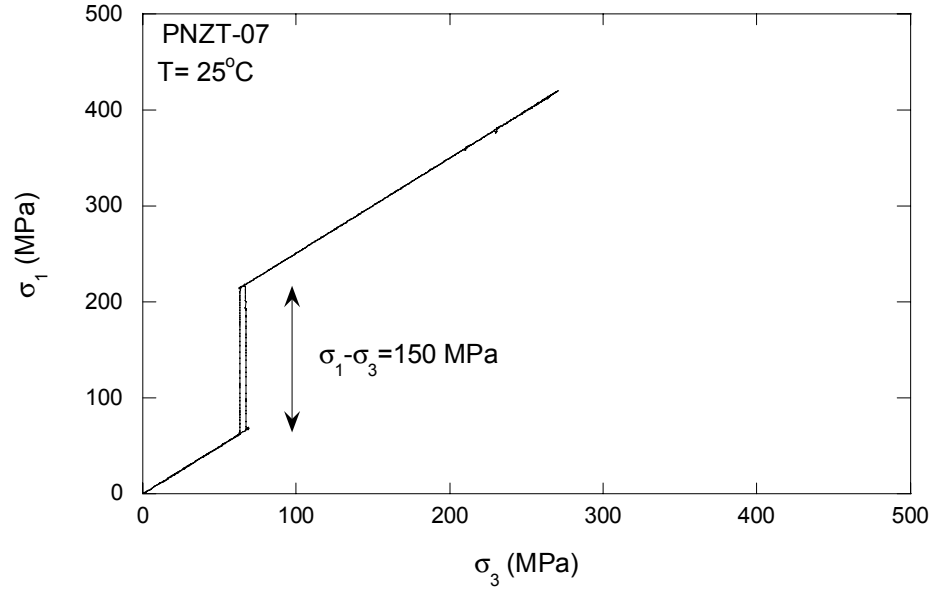
PNZT-07
T= 25°C
σ1-σ3=150 MPa
σ1 (MPa)
σ3 (MPa)
0
100
200
300
400
500

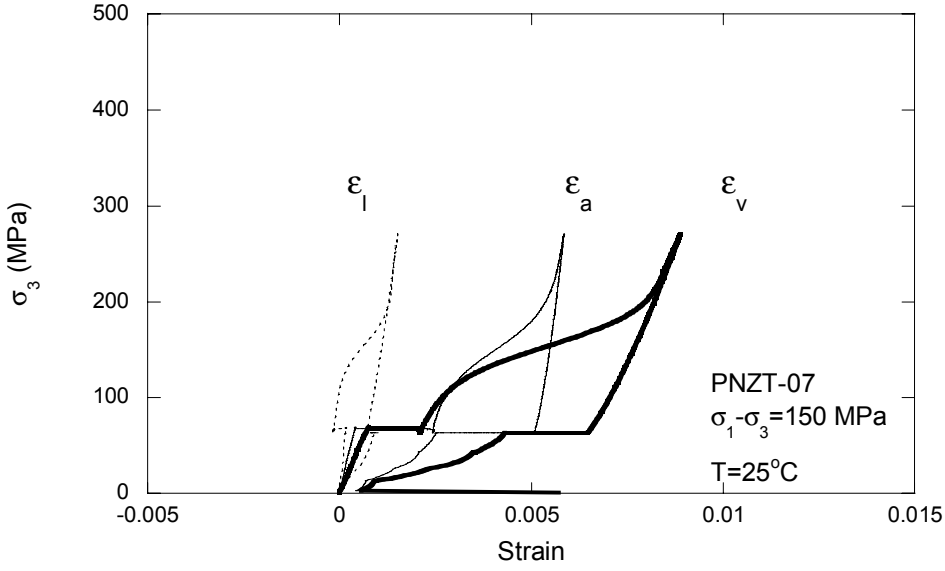
εl
εa
εv
PNZT-07
σ1-σ3=150 MPa
T=25°C
σ3 (MPa)
Strain
-0.005
0
0.005
0.01
0.015

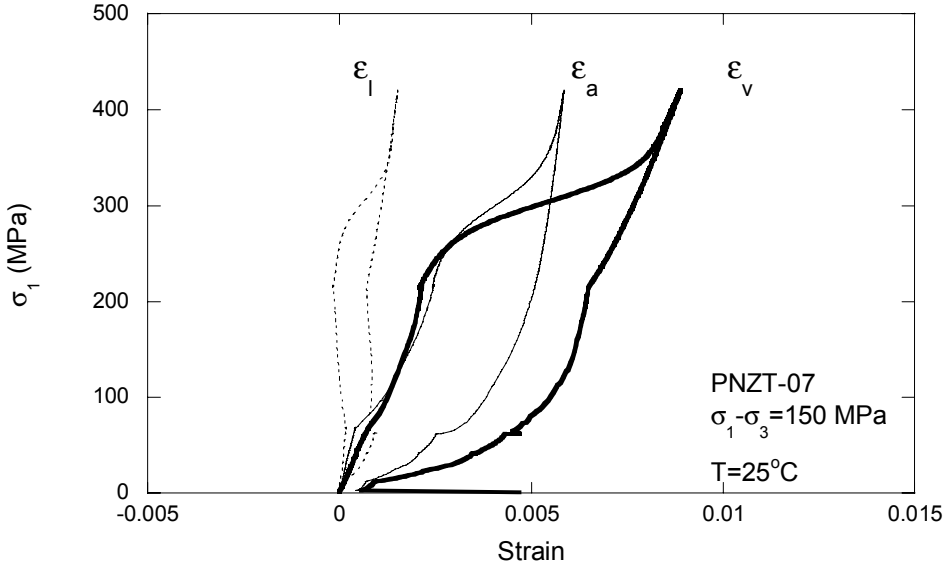
εl
εa
εv
PNZT-07
σ1-σ3=150 MPa
T=25°C
σ1 (MPa)
Strain
-0.005
0
0.005
0.01
0.015

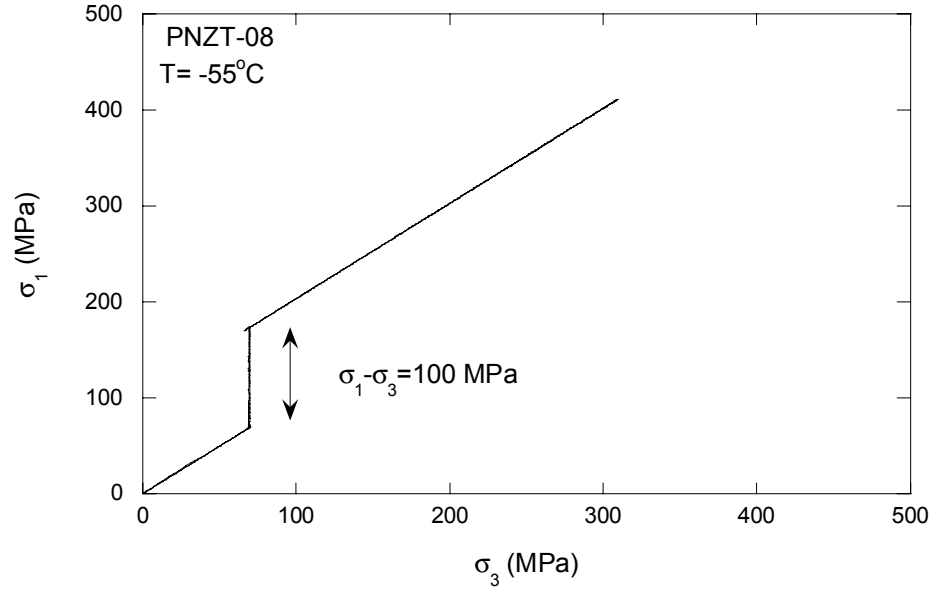
PNZT-08
T= -55°C
σ1-σ3=100 MPa
σ1 (MPa)
σ3 (MPa)
0
100
200
300
400
500

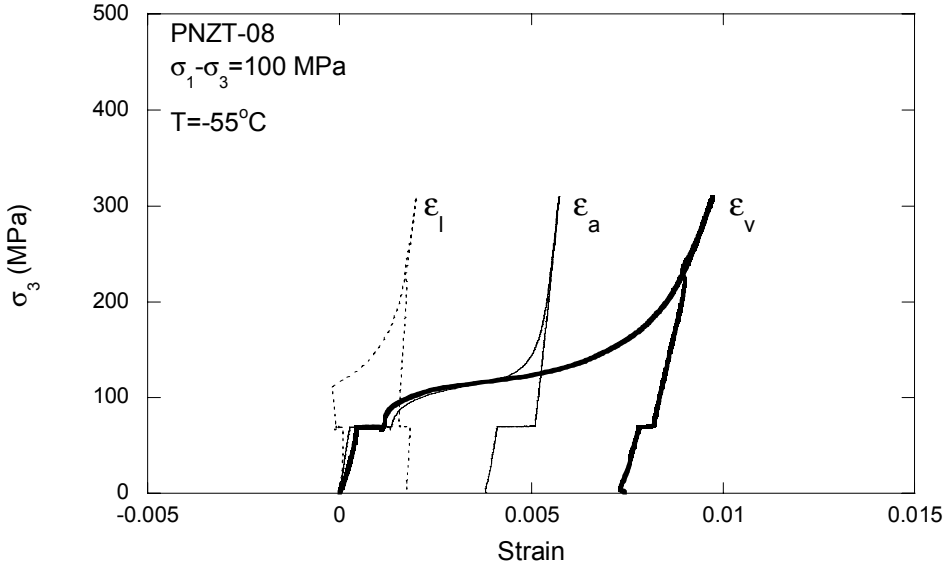
PNZT-08
σ1-σ3=100 MPa
T=-55°C
εl
εa
εv
σ3 (MPa)
Strain
-0.005
0
0.005
0.01
0.015

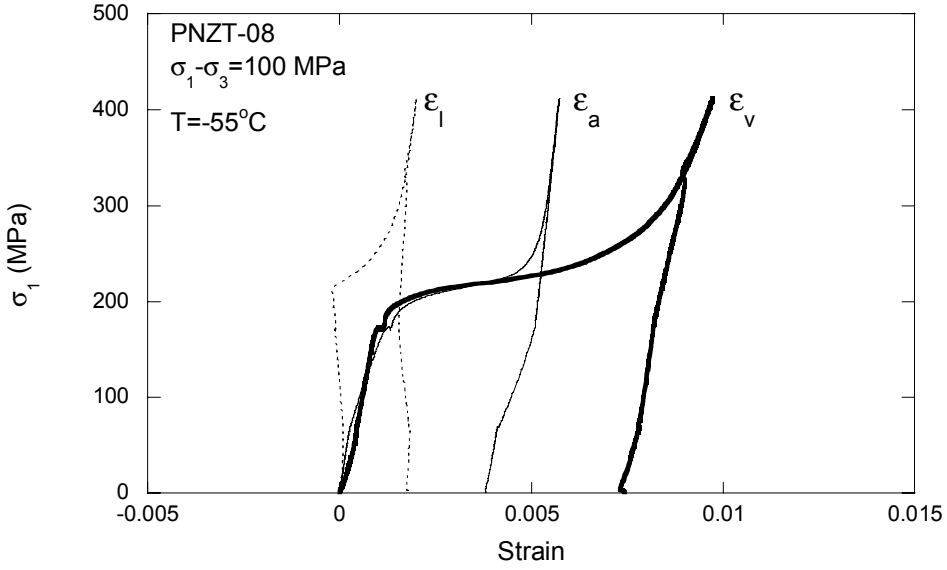
PNZT-08
σ1-σ3=100 MPa
T=-55°C
εl
εa
εv
σ1 (MPa)
Strain
-0.005
0
0.005
0.01
0.015

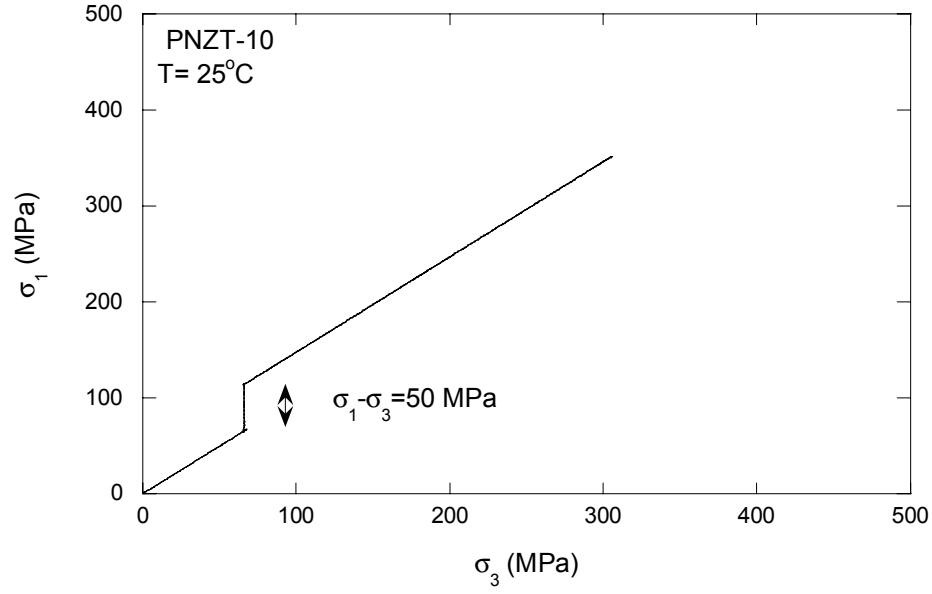
PNZT-10
T= 25°C
σ1-σ3=50 MPa
σ1 (MPa)
σ3 (MPa)
0
100
200
300
400
500

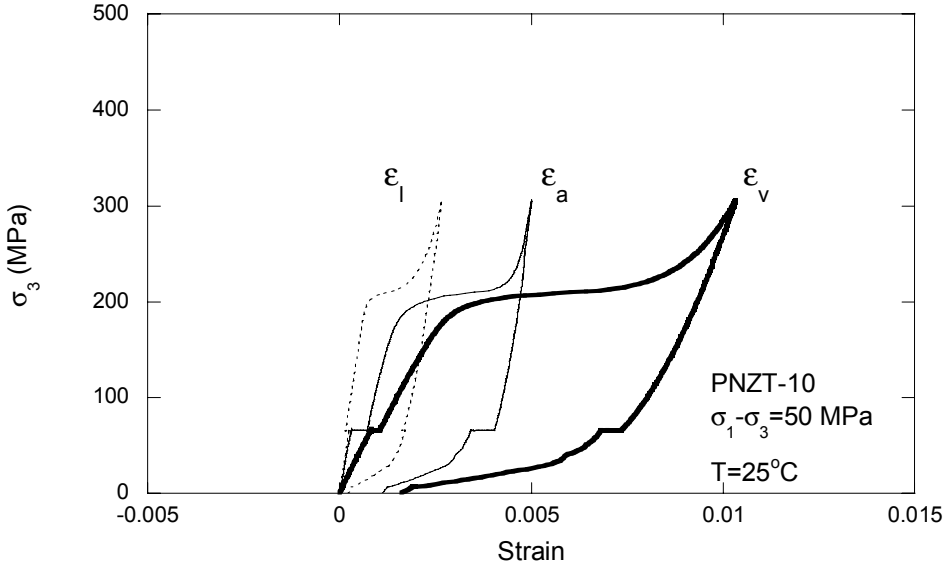
εl
εa
εv
PNZT-10
σ1-σ3=50 MPa
T=25°C
σ3 (MPa)
Strain
-0.005
0
0.005
0.01
0.015

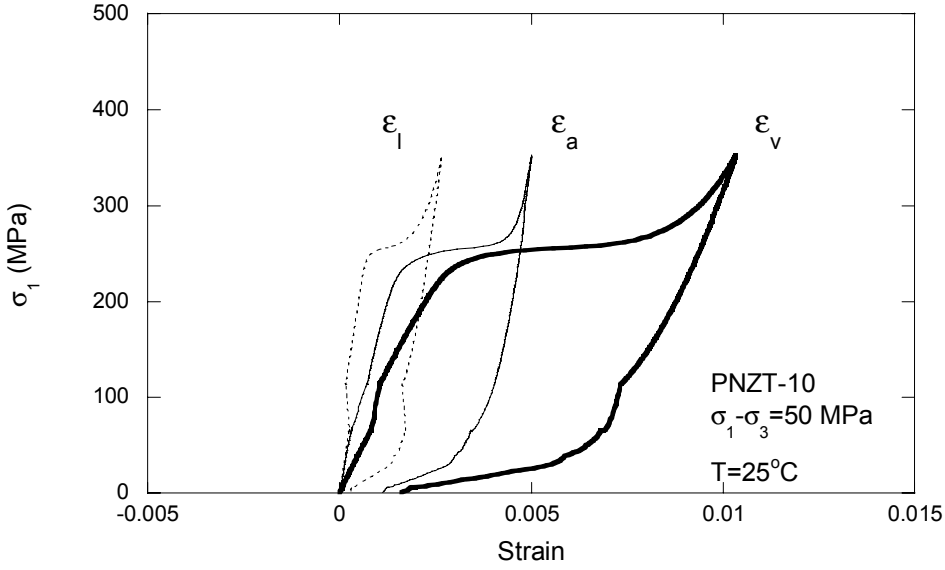
εl
εa
εv
PNZT-10
σ1-σ3=50 MPa
T=25°C
σ1 (MPa)
Strain
-0.005
0
0.005
0.01
0.015

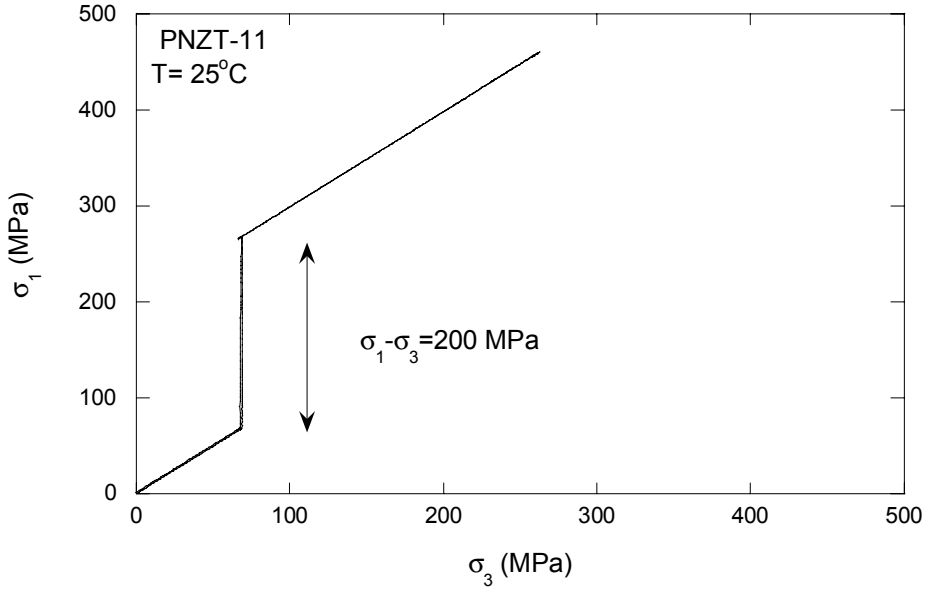
PNZT-11
T= 25°C
σ1-σ3=200 MPa
σ1 (MPa)
σ3 (MPa)
0
100
200
300
400
500

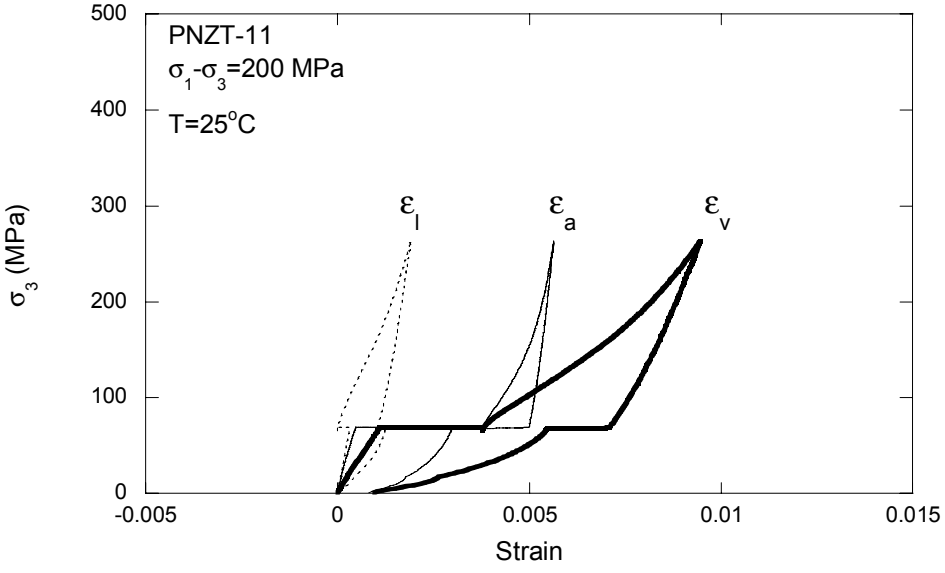
PNZT-11
σ1-σ3=200 MPa
T=25°C
εl
εa
εv
σ3 (MPa)
Strain
-0.005
0
0.005
0.01
0.015

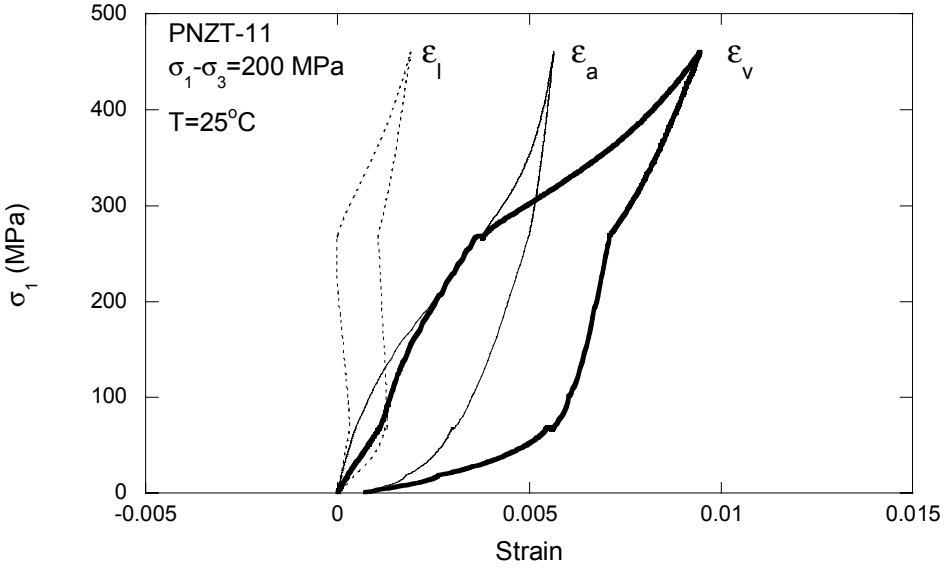
PNZT-11
σ1-σ3=200 MPa
T=25°C
εl
εa
εv
σ1 (MPa)
Strain
-0.005
0
0.005
0.01
0.015

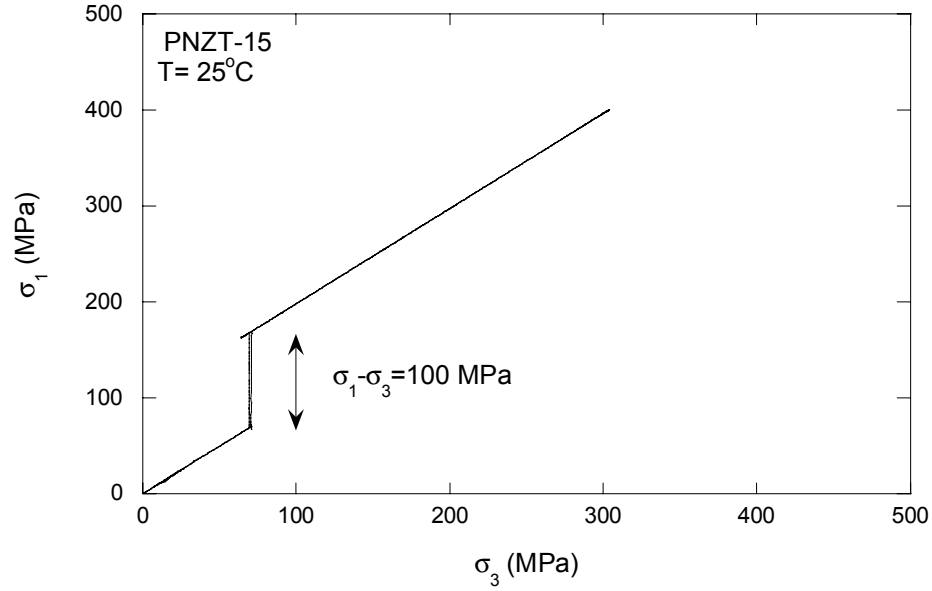
PNZT-15
T= 25°C
σ1-σ3=100 MPa
σ1 (MPa)
σ3 (MPa)
0
100
200
300
400
500

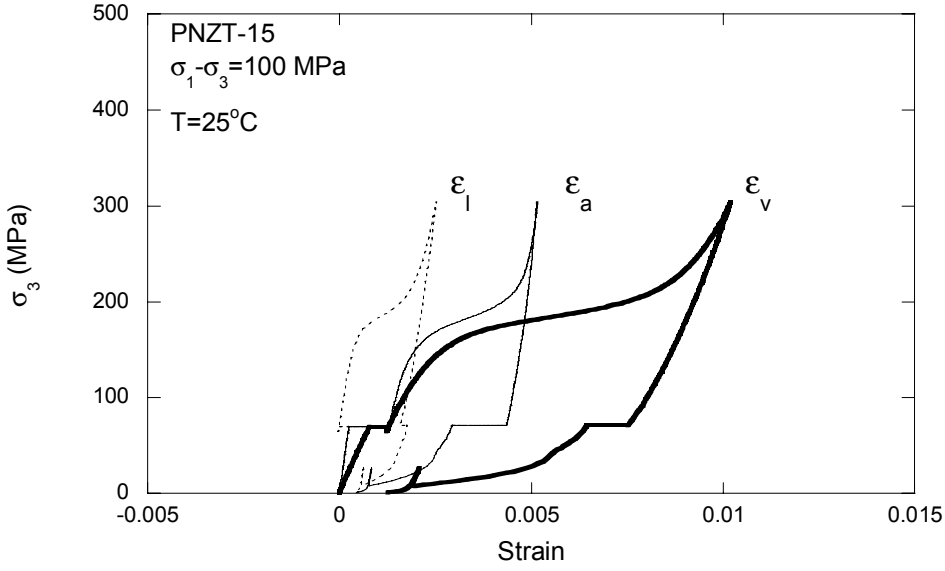
PNZT-15
σ1-σ3=100 MPa
T=25°C
εl
εa
εv
σ3 (MPa)
Strain
-0.005
0
0.005
0.01
0.015

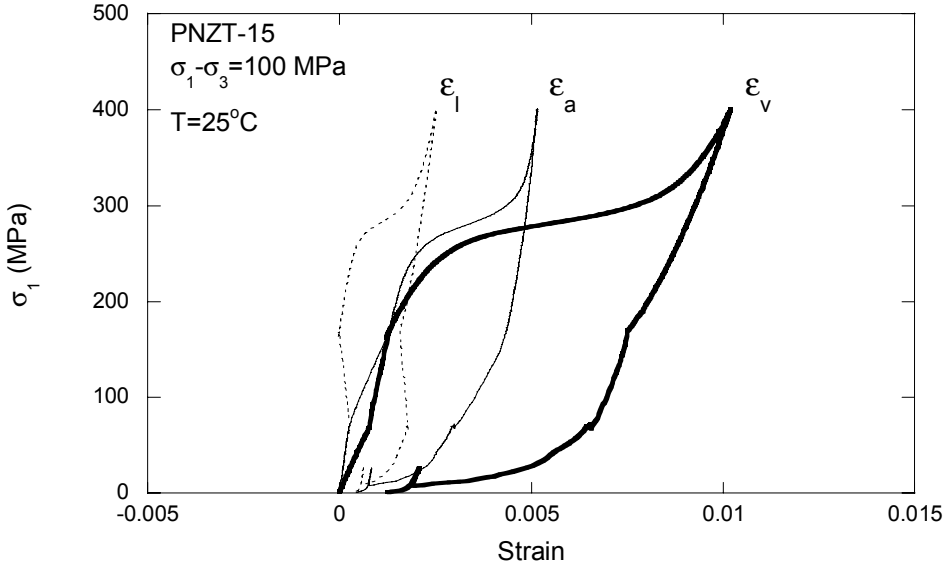
PNZT-15
σ1-σ3=100 MPa
T=25°C
εl
εa
εv
σ1 (MPa)
Strain
-0.005
0
0.005
0.01
0.015

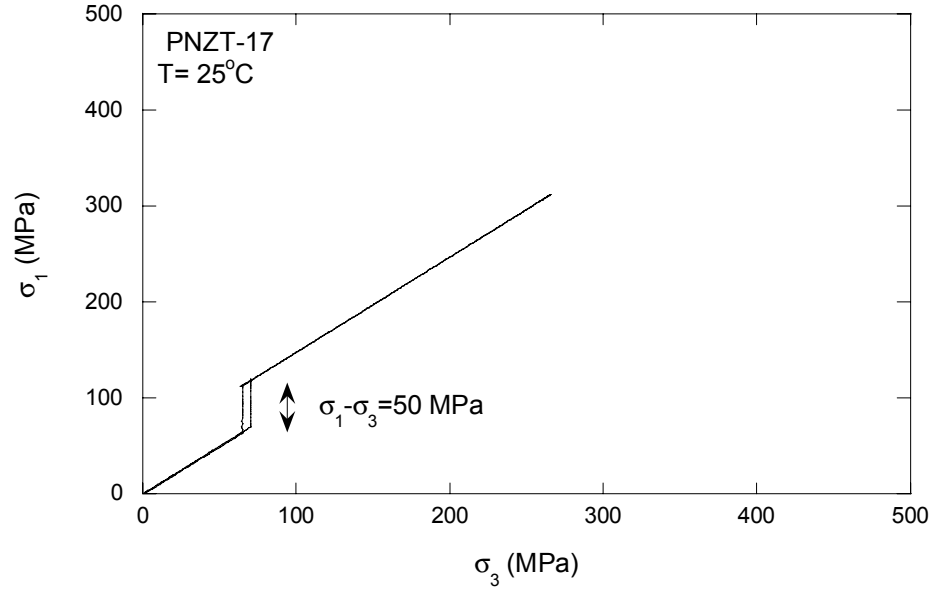
PNZT-17
T= 25°C
σ1-σ3=50 MPa
σ1 (MPa)
σ3 (MPa)
0
100
200
300
400
500

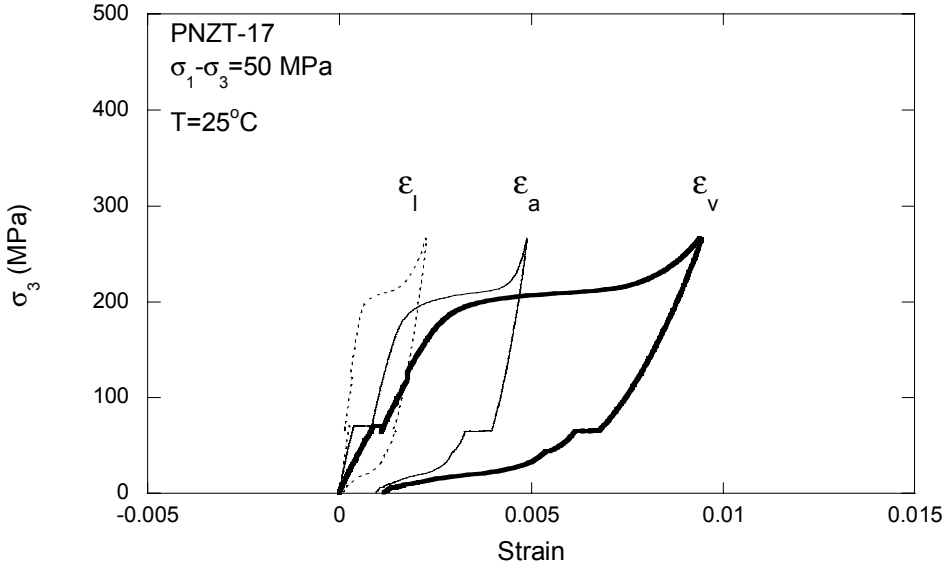
PNZT-17
σ1-σ3=50 MPa
T=25°C
εl
εa
εv
σ3 (MPa)
Strain
-0.005
0
0.005
0.01
0.015

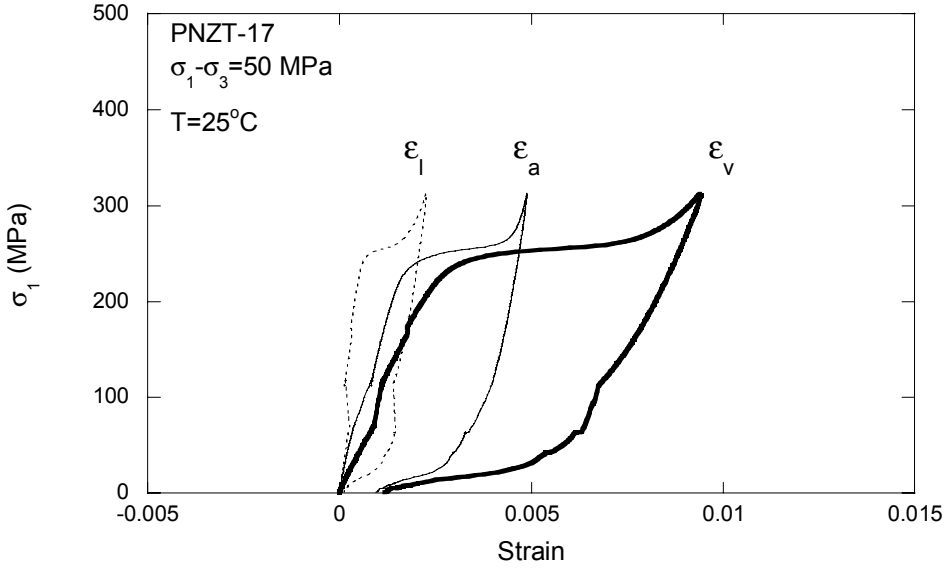
PNZT-17
σ1-σ3=50 MPa
T=25°C
εl
εa
εv
σ1 (MPa)
Strain
-0.005
0
0.005
0.01
0.015

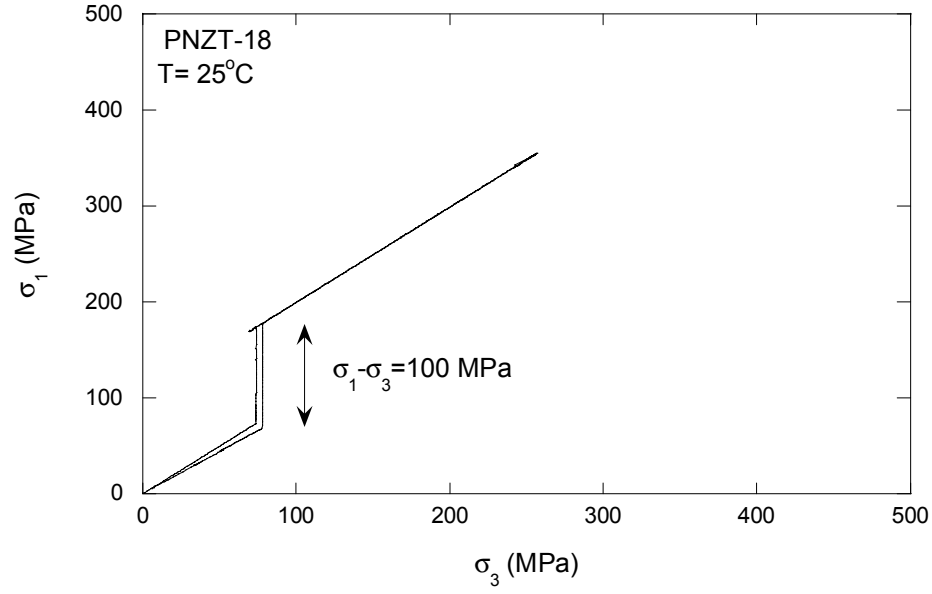
PNZT-18
T= 25°C
σ1-σ3=100 MPa
σ1 (MPa)
σ3 (MPa)
0
100
200
300
400
500

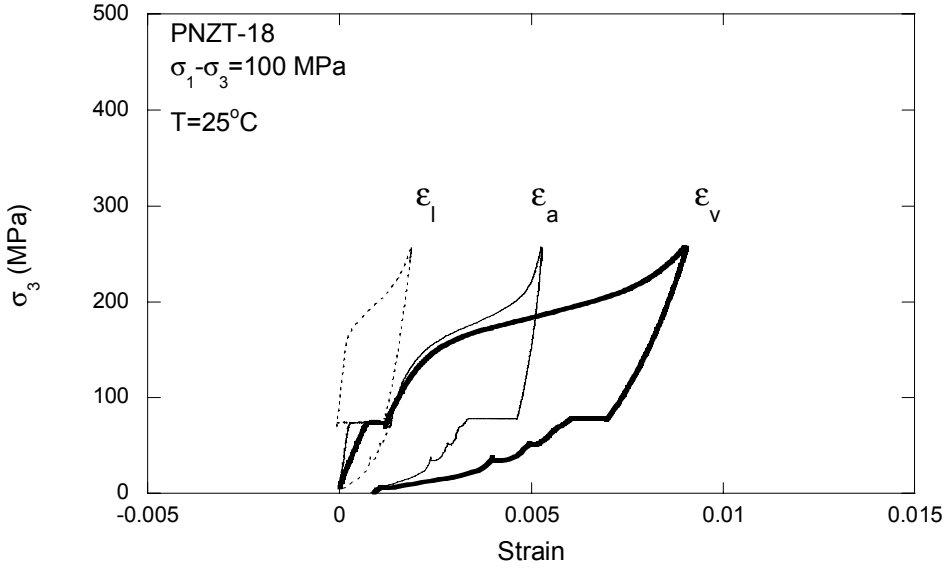
PNZT-18
σ1-σ3=100 MPa
T=25°C
εl
εa
εv
σ3 (MPa)
Strain
-0.005
0
0.005
0.01
0.015

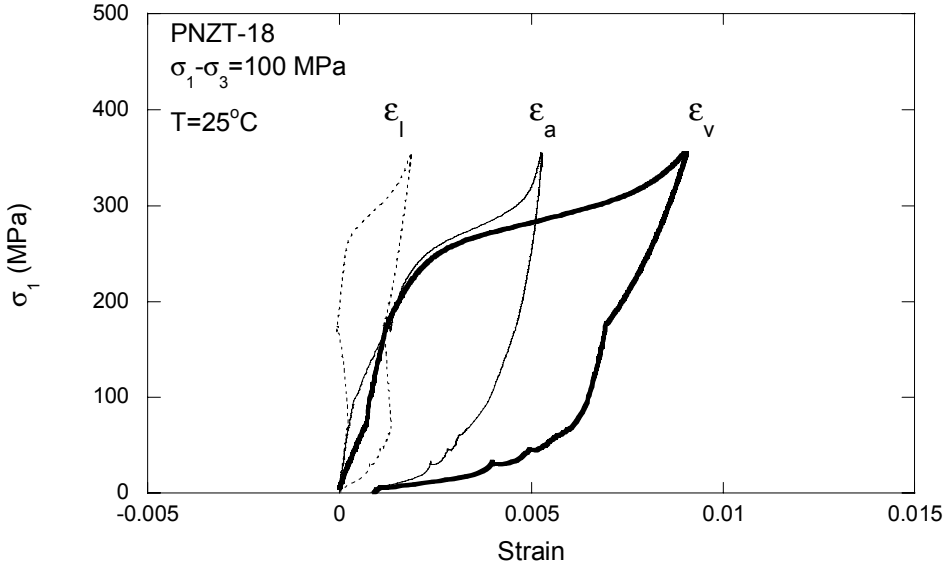
PNZT-18
σ1-σ3=100 MPa
T=25°C
εl
εa
εv
σ1 (MPa)
Strain
-0.005
0
0.005
0.01
0.015

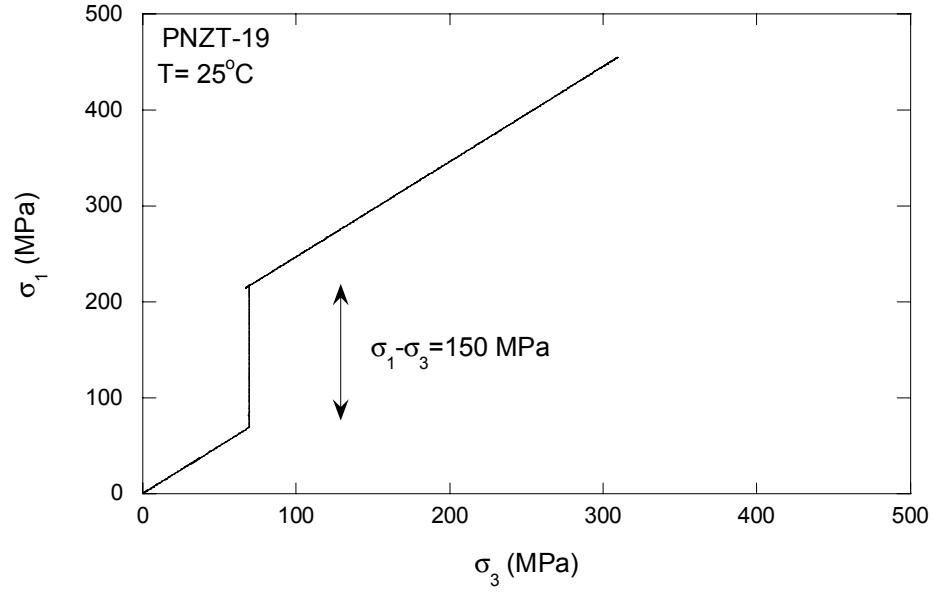
PNZT-19
T= 25°C
σ1-σ3=150 MPa
σ1 (MPa)
σ3 (MPa)
0
100
200
300
400
500

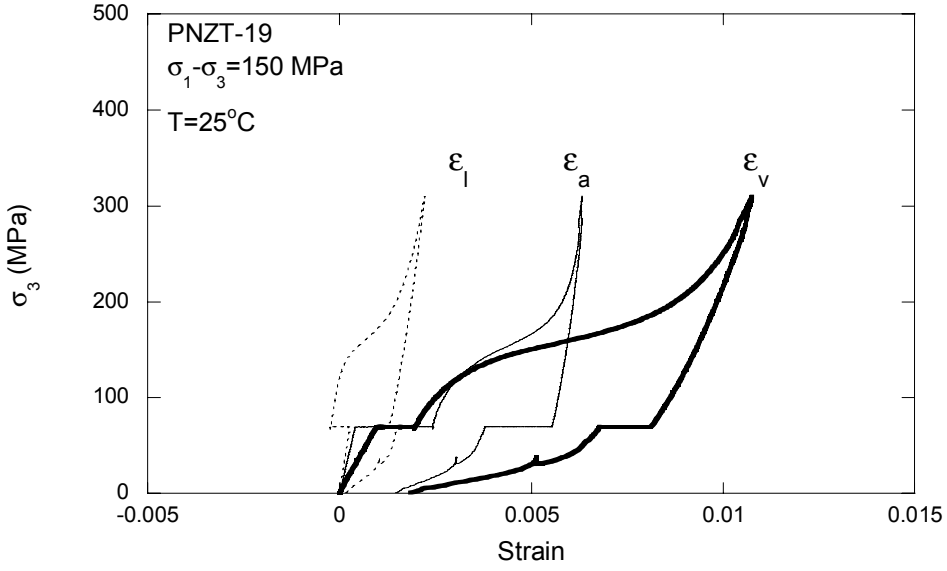
PNZT-19
σ1-σ3=150 MPa
T=25°C
εl
εa
εv
σ3 (MPa)
Strain
-0.005
0
0.005
0.01
0.015

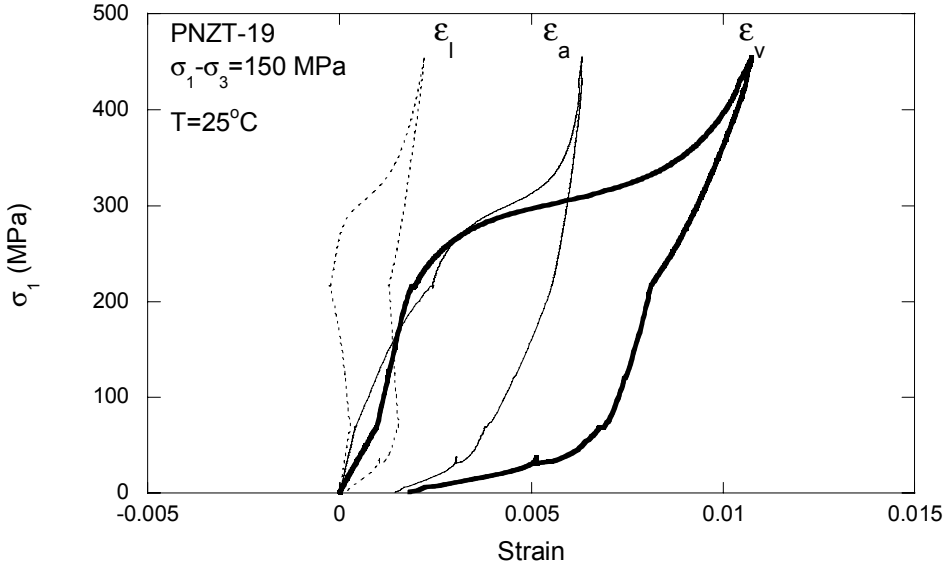
PNZT-19
σ1-σ3=150 MPa
T=25°C
εl
εa
εv
σ1 (MPa)
Strain
-0.005
0
0.005
0.01
0.015

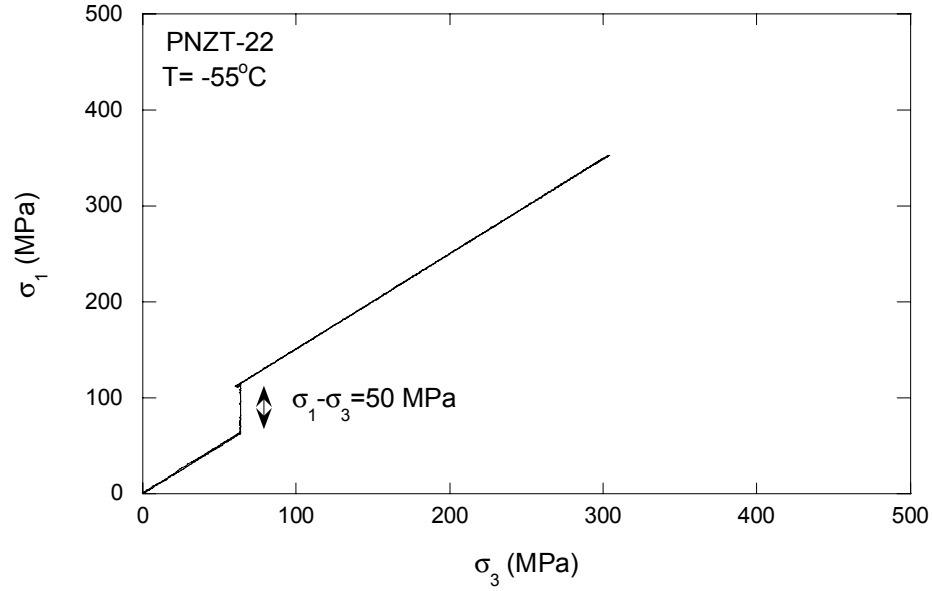
PNZT-22
T= -55°C
σ1-σ3=50 MPa
σ1 (MPa)
σ3 (MPa)
0
100
200
300
400
500

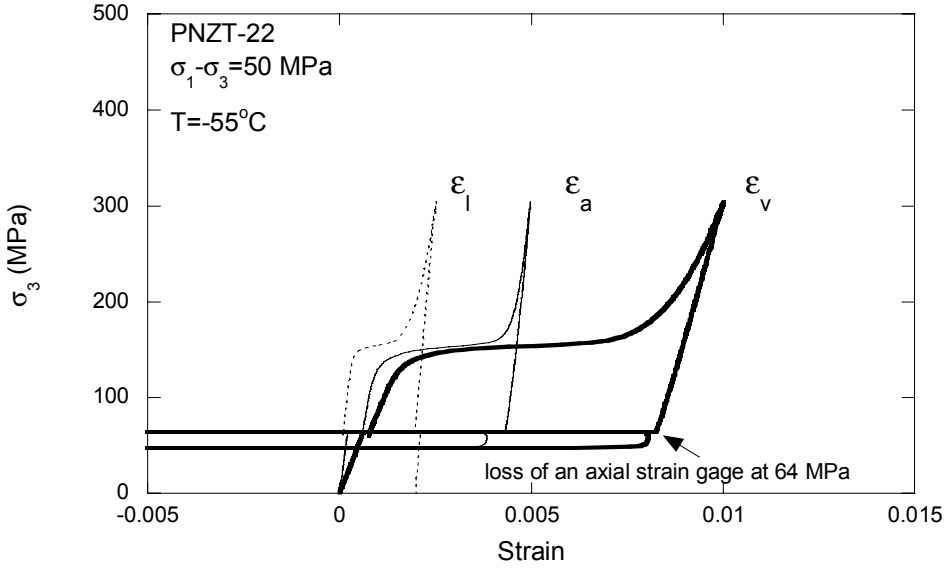
PNZT-22
σ1-σ3=50 MPa
T=-55°C
εl
εa
εv
loss of an axial strain gage at 64 MPa
σ3 (MPa)
Strain
-0.005
0
0.005
0.01
0.015

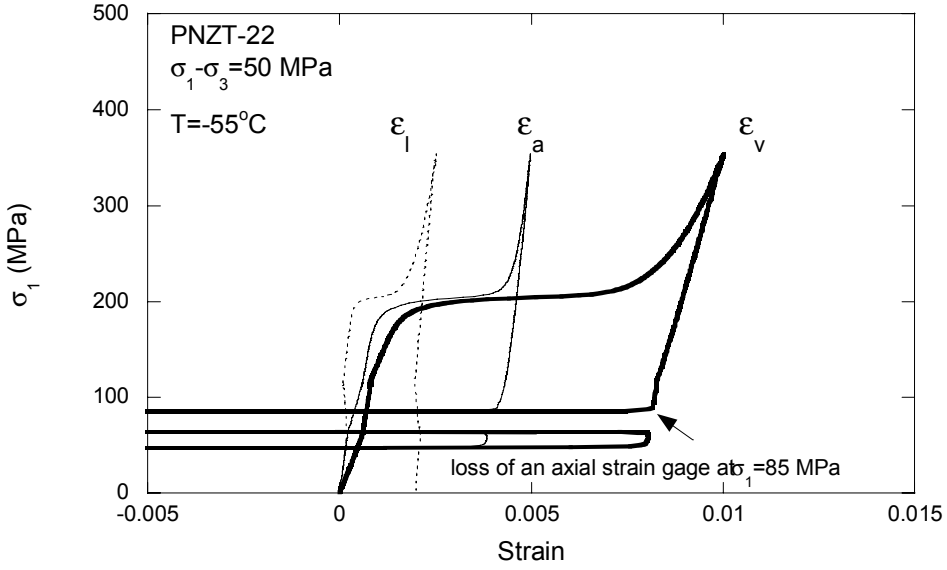
PNZT-22
σ1-σ3=50 MPa
T=-55°C
εl
εa
εv
loss of an axial strain gage at σ1=85 MPa
σ1 (MPa)
Strain
-0.005
0
0.005
0.01
0.015

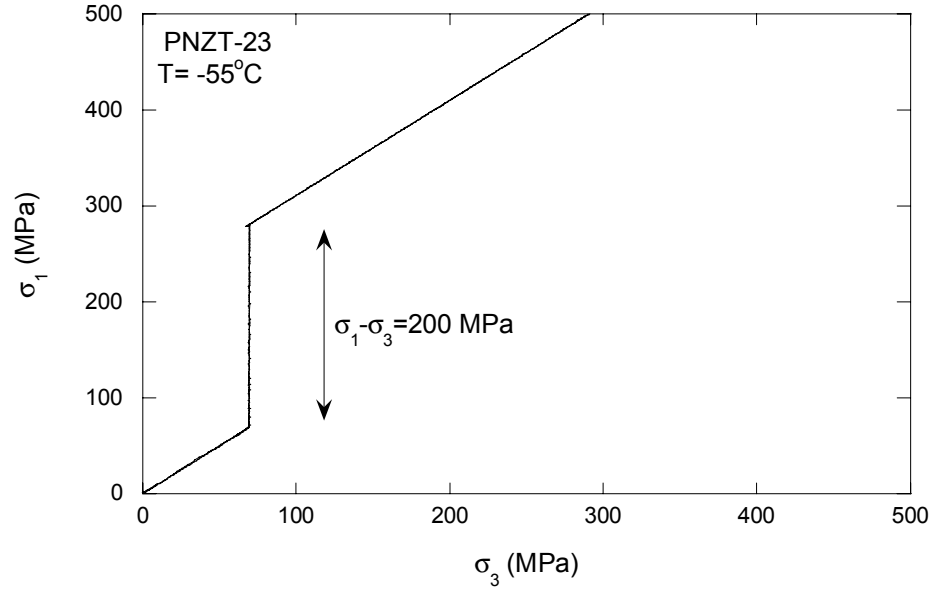
PNZT-23
T= -55°C
σ1-σ3=200 MPa
σ1 (MPa)
σ3 (MPa)
0
100
200
300
400
500

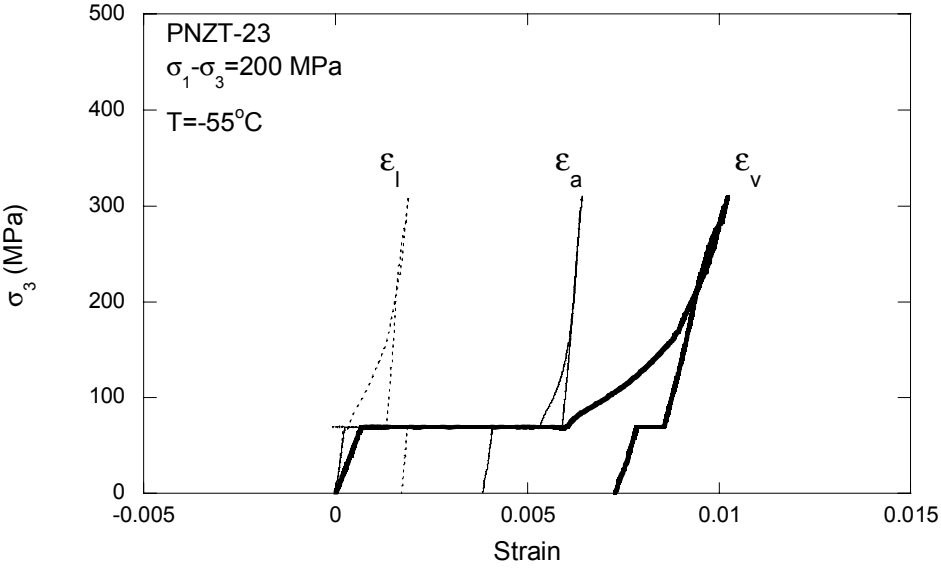
PNZT-23
σ1-σ3=200 MPa
T=-55°C
εl
εa
εv
σ3 (MPa)
Strain
-0.005
0
0.005
0.01
0.015

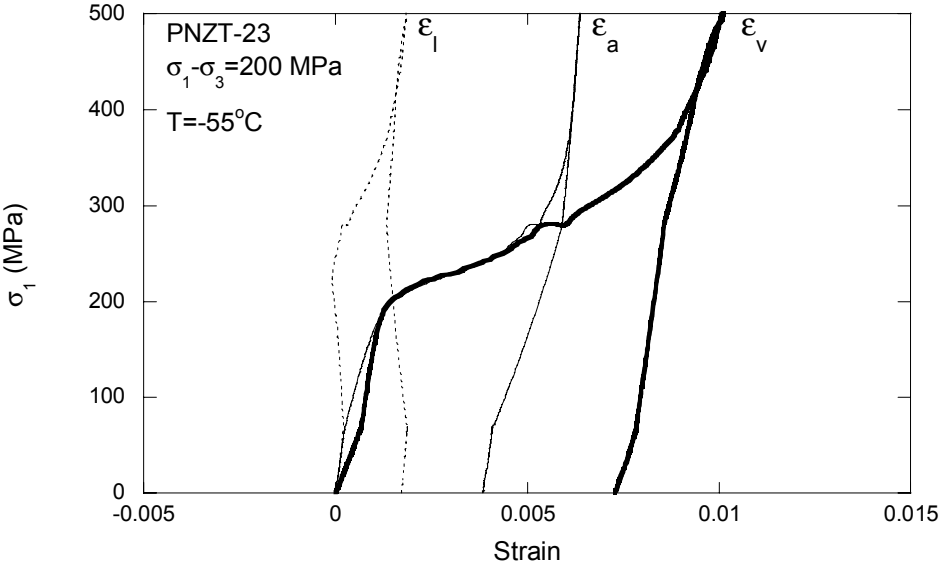
PNZT-23
σ1-σ3=200 MPa
T=-55°C
εl
εa
εv
σ1 (MPa)
Strain
-0.005
0
0.005
0.01
0.015

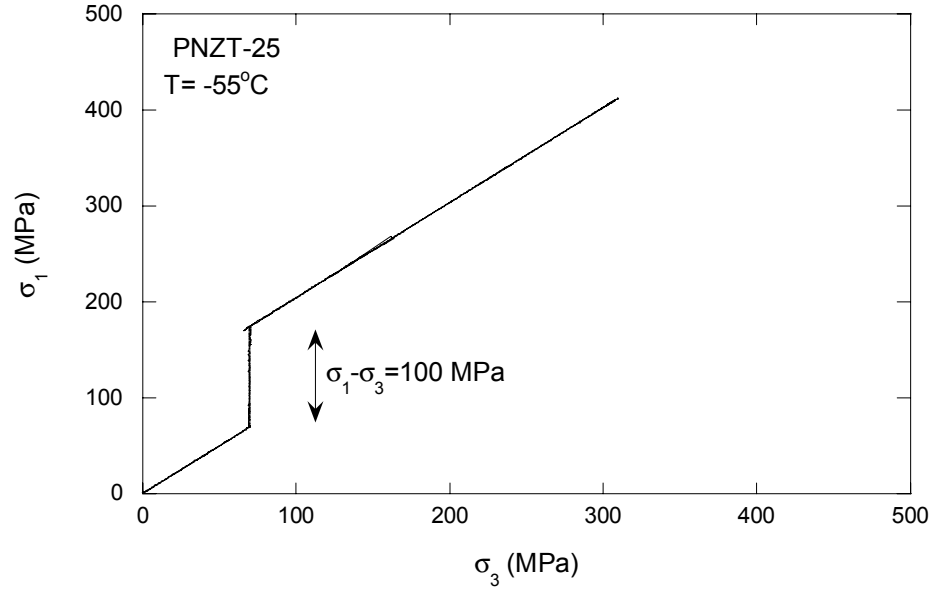
PNZT-25
T= -55°C
σ1-σ3=100 MPa
σ1 (MPa)
σ3 (MPa)
0
100
200
300
400
500

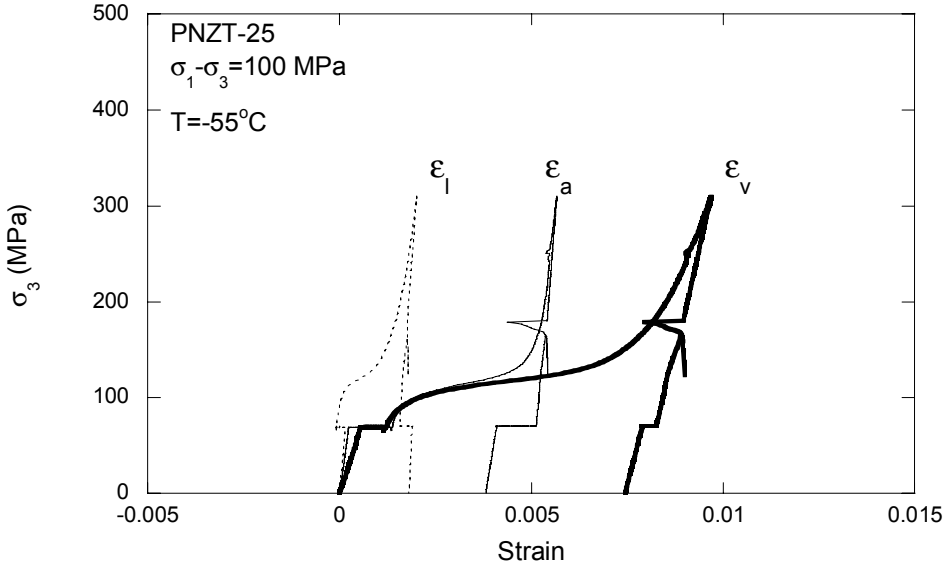
PNZT-25
σ1-σ3=100 MPa
T=-55°C
εl
εa
εv
σ3 (MPa)
Strain
-0.005
0
0.005
0.01
0.015

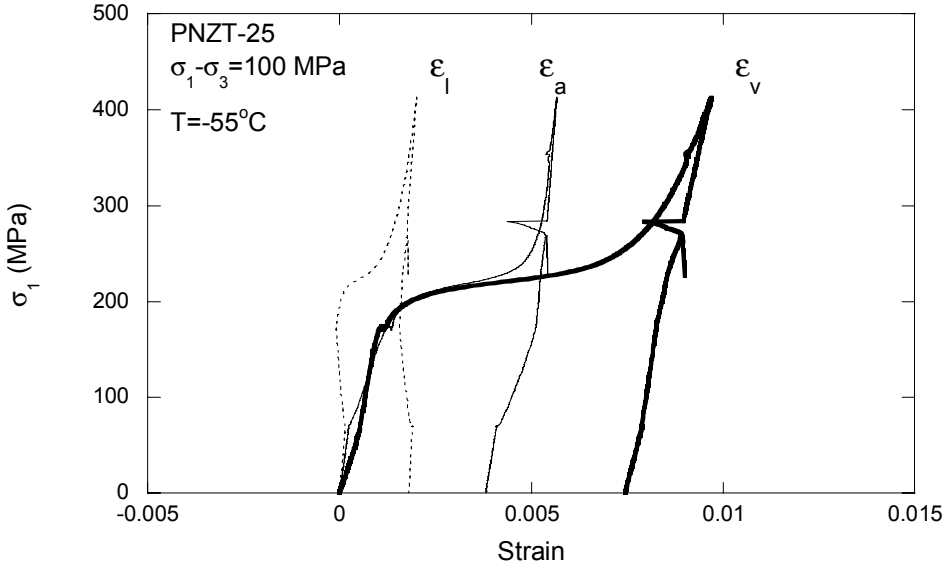
PNZT-25
σ1-σ3=100 MPa
T=-55°C
εl
εa
εv
σ1 (MPa)
Strain
-0.005
0
0.005
0.01
0.015

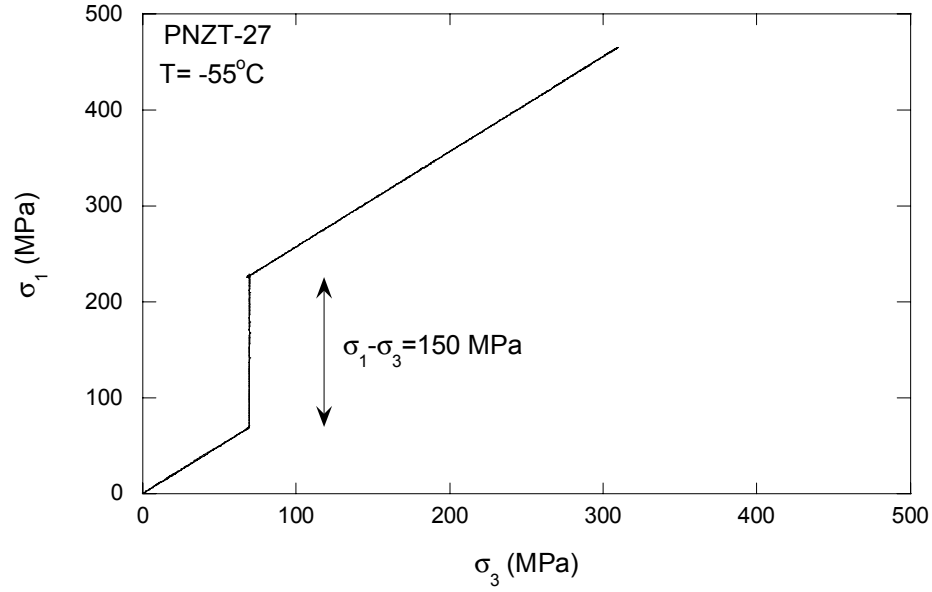
PNZT-27
T= -55°C
σ1-σ3=150 MPa
σ1 (MPa)
σ3 (MPa)
0
100
200
300
400
500

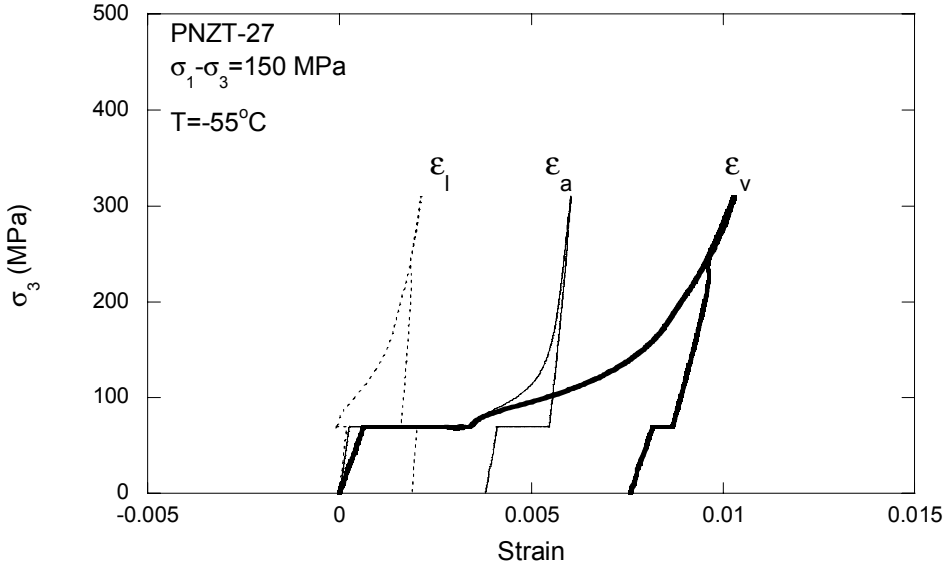
PNZT-27
σ1-σ3=150 MPa
T=-55°C
εl
εa
εv
σ3 (MPa)
Strain
-0.005
0
0.005
0.01
0.015

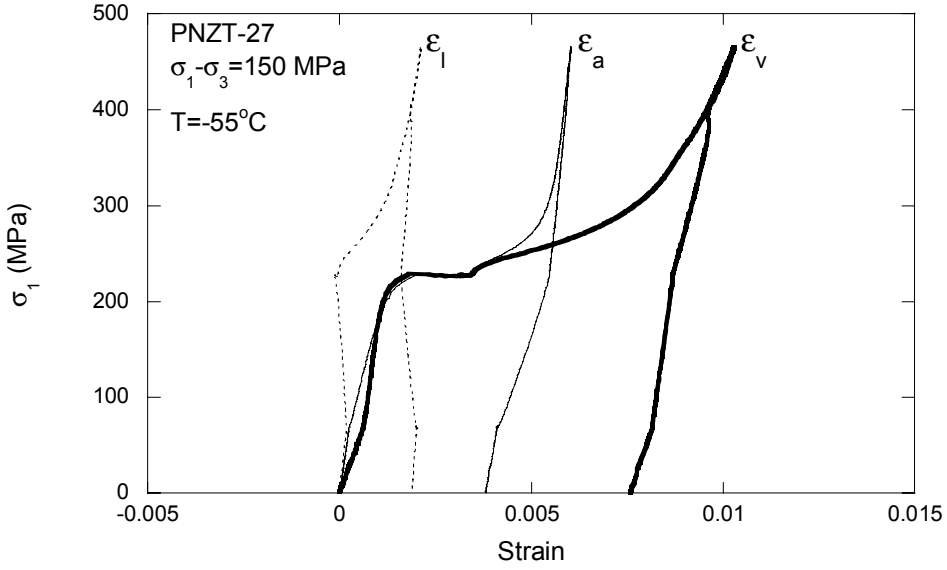
PNZT-27
σ1-σ3=150 MPa
T=-55°C
εl
εa
εv
σ1 (MPa)
Strain
-0.005
0
0.005
0.01
0.015

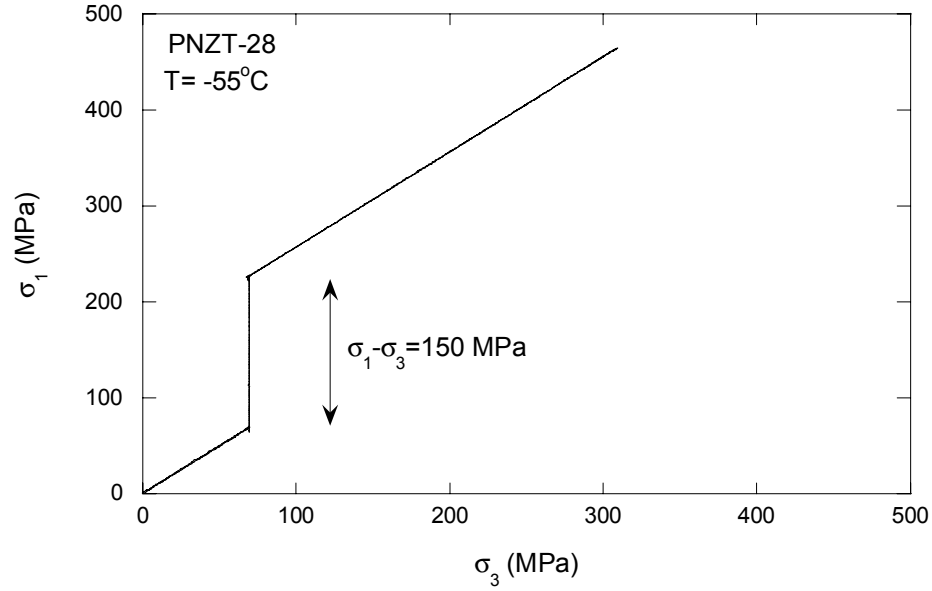
PNZT-28
T= -55°C
σ1-σ3=150 MPa
σ1 (MPa)
σ3 (MPa)
0
100
200
300
400
500

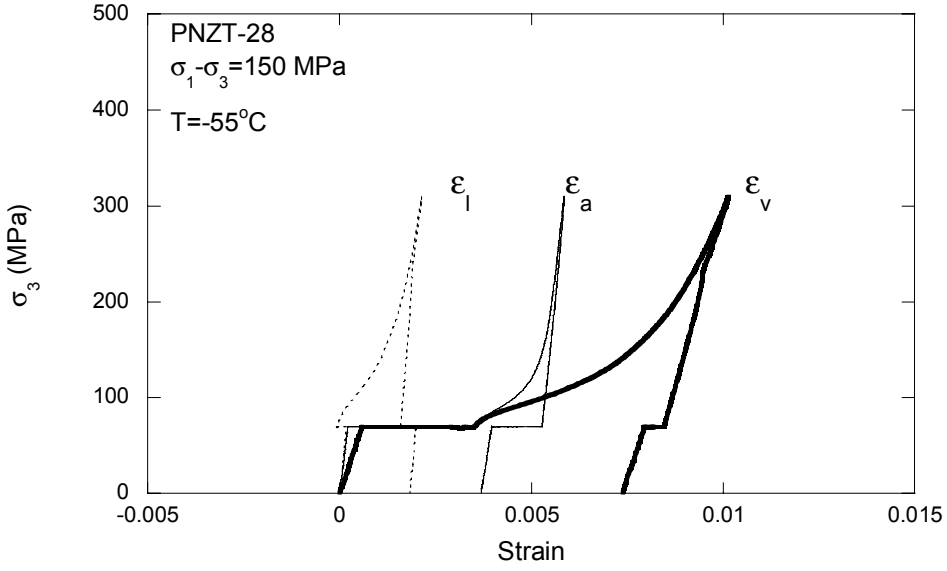
PNZT-28
σ1-σ3=150 MPa
T=-55°C
εl
εa
εv
σ3 (MPa)
Strain
-0.005
0
0.005
0.01
0.015

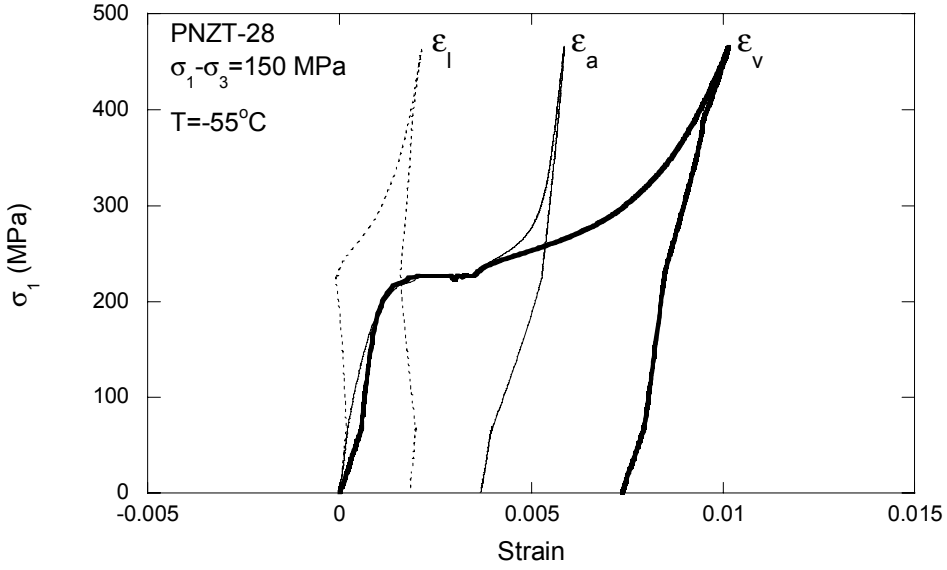
PNZT-28
σ1-σ3=150 MPa
T=-55°C
εl
εa
εv
σ1 (MPa)
Strain
-0.005
0
0.005
0.01
0.015

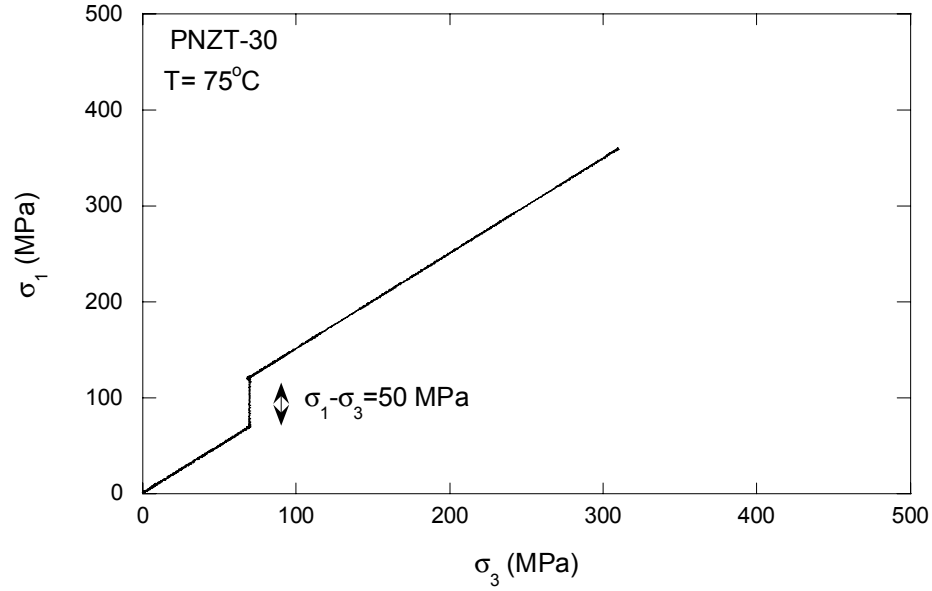
PNZT-30
T= 75°C
σ1-σ3=50 MPa
σ1 (MPa)
σ3 (MPa)
0
100
200
300
400
500

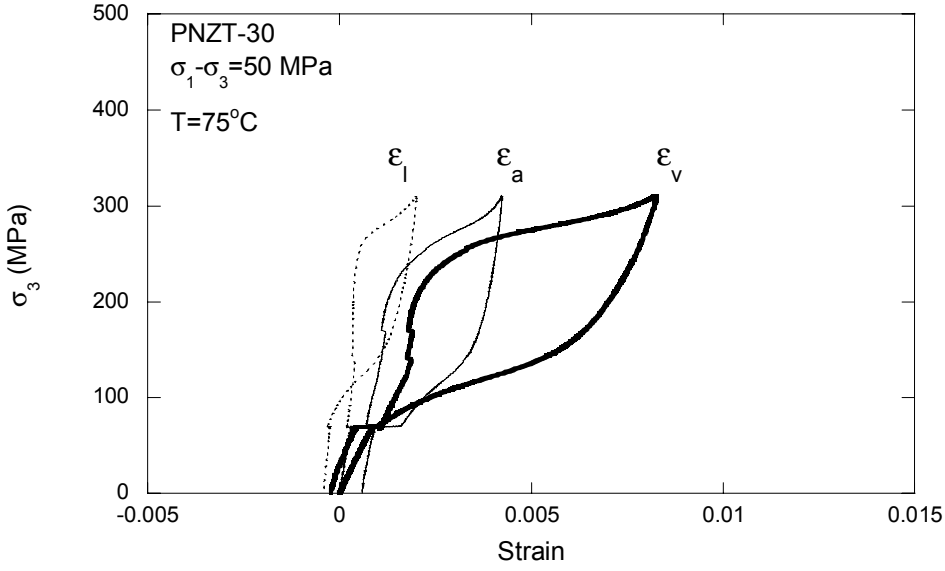
PNZT-30
σ1-σ3=50 MPa
T=75°C
εl
εa
εv
σ3 (MPa)
Strain
-0.005
0
0.005
0.01
0.015

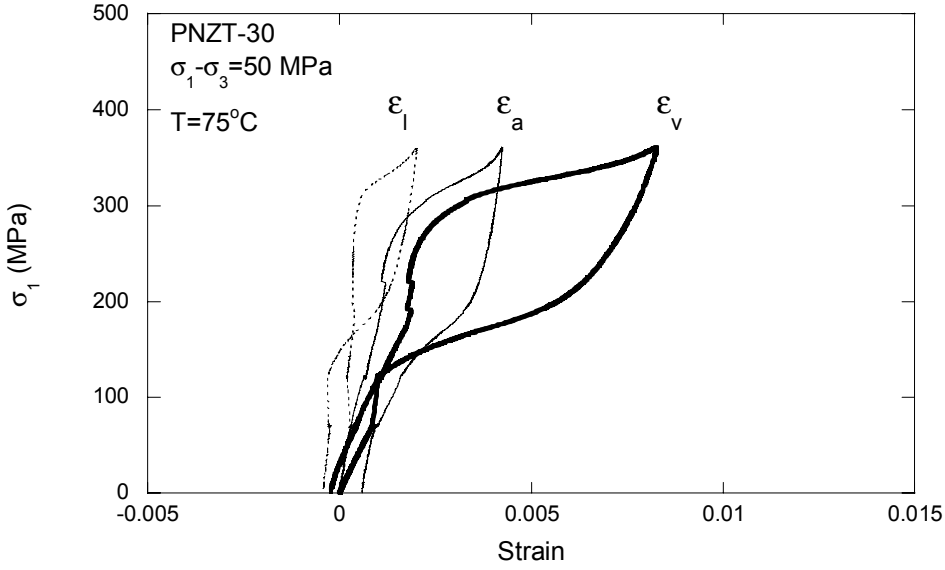
PNZT-30
σ1-σ3=50 MPa
T=75°C
εl
εa
εv
σ1 (MPa)
Strain
-0.005
0
0.005
0.01
0.015

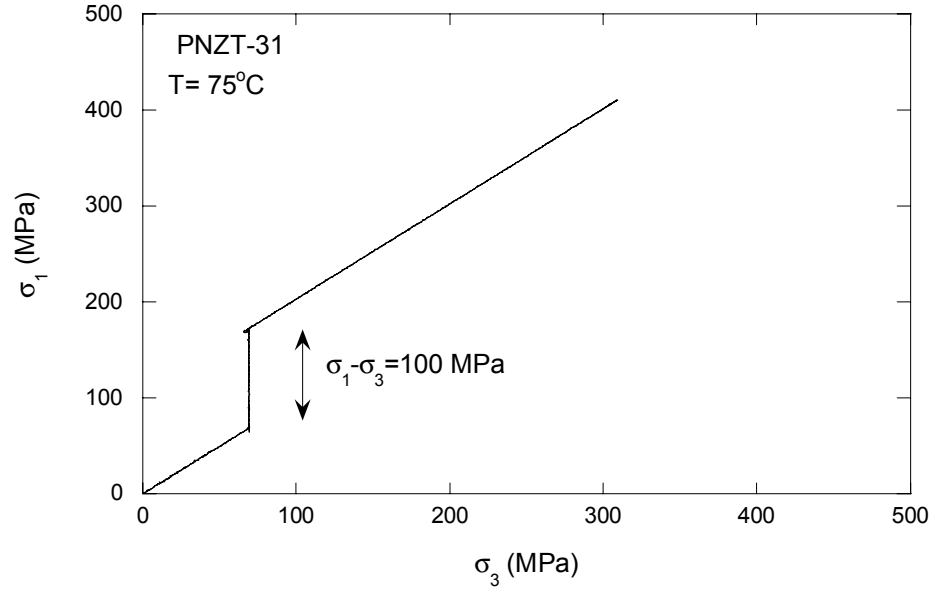
PNZT-31
T= 75°C
σ1-σ3=100 MPa
σ1 (MPa)
σ3 (MPa)
0
100
200
300
400
500

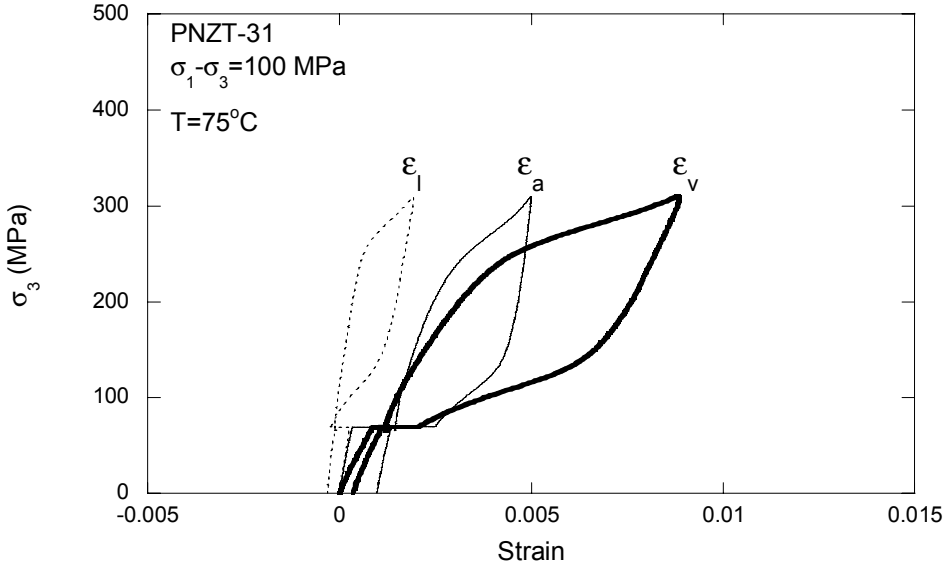
PNZT-31
σ1-σ3=100 MPa
T=75°C
εl
εa
εv
σ3 (MPa)
Strain
-0.005
0
0.005
0.01
0.015

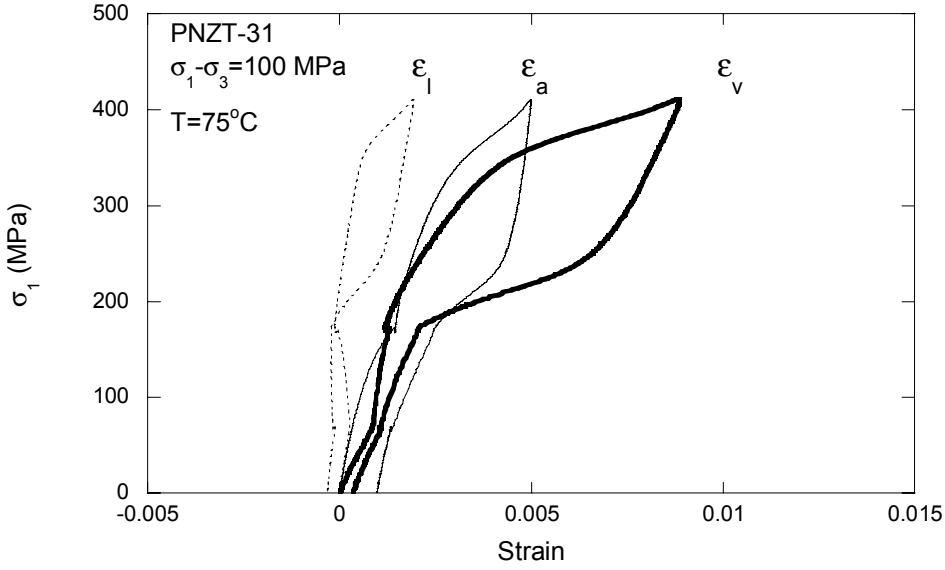
PNZT-31
σ1-σ3=100 MPa
T=75°C
εl
εa
εv
σ1 (MPa)
Strain
-0.005
0
0.005
0.01
0.015

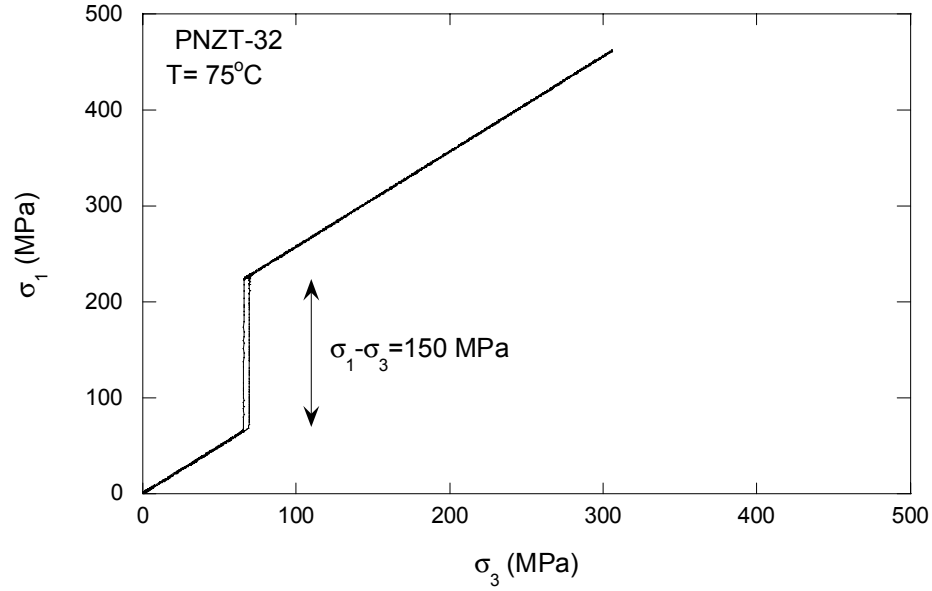
PNZT-32
T= 75°C
σ1-σ3=150 MPa
σ1 (MPa)
σ3 (MPa)
0
100
200
300
400
500

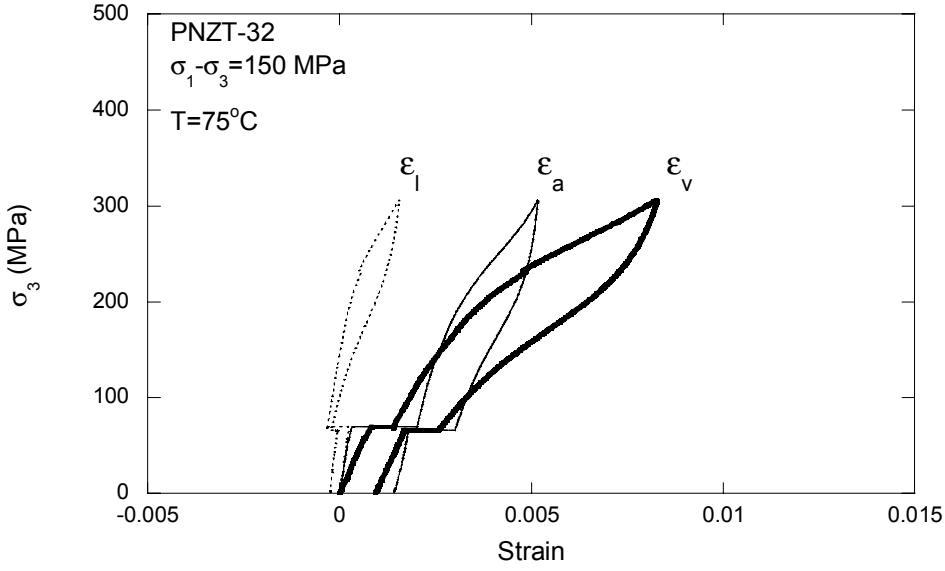
PNZT-32
σ1-σ3=150 MPa
T=75°C
εl
εa
εv
σ3 (MPa)
Strain
-0.005
0
0.005
0.01
0.015

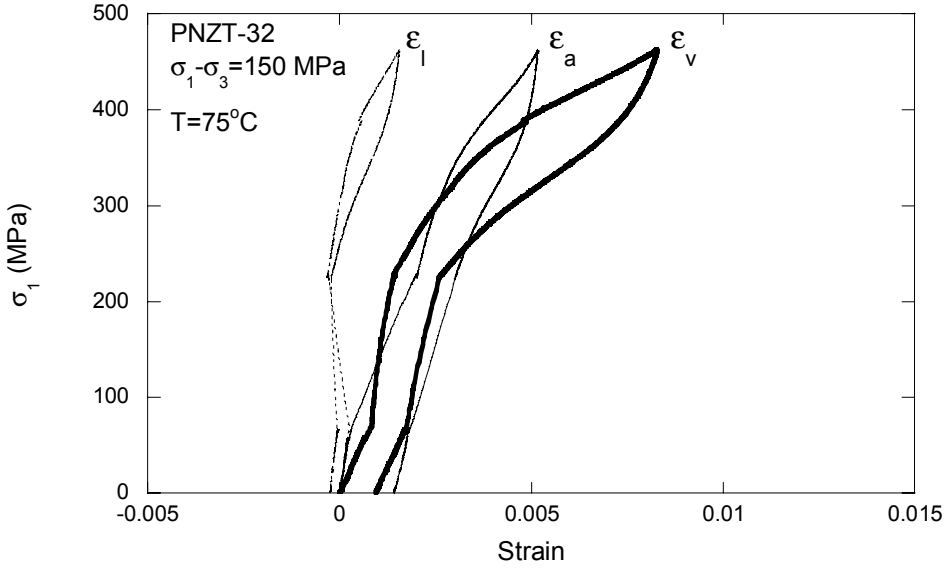
PNZT-32
σ1-σ3=150 MPa
T=75°C
εl
εa
εv
σ1 (MPa)
Strain
-0.005
0
0.005
0.01
0.015

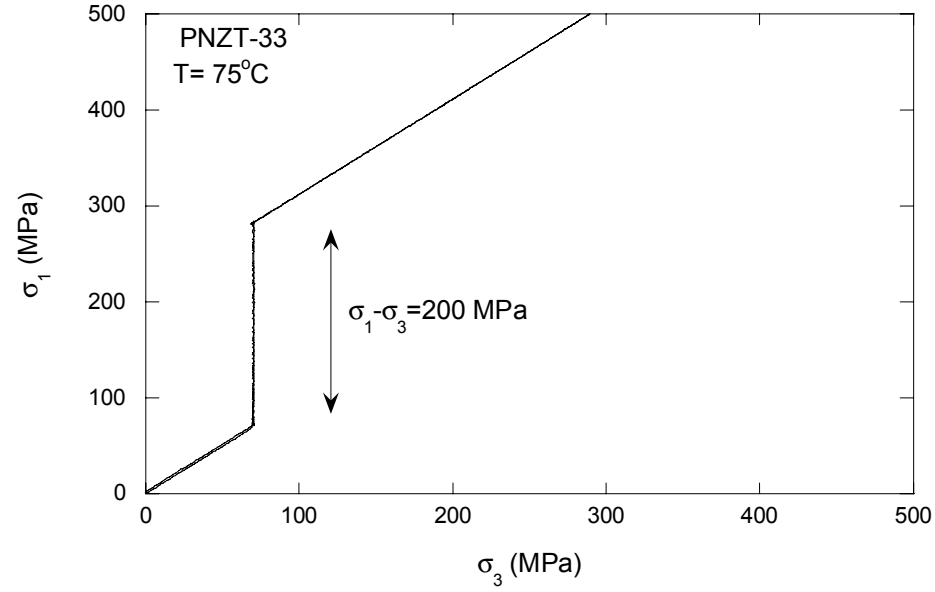
PNZT-33
T= 75°C
σ1-σ3=200 MPa
σ1 (MPa)
σ3 (MPa)
0
100
200
300
400
500

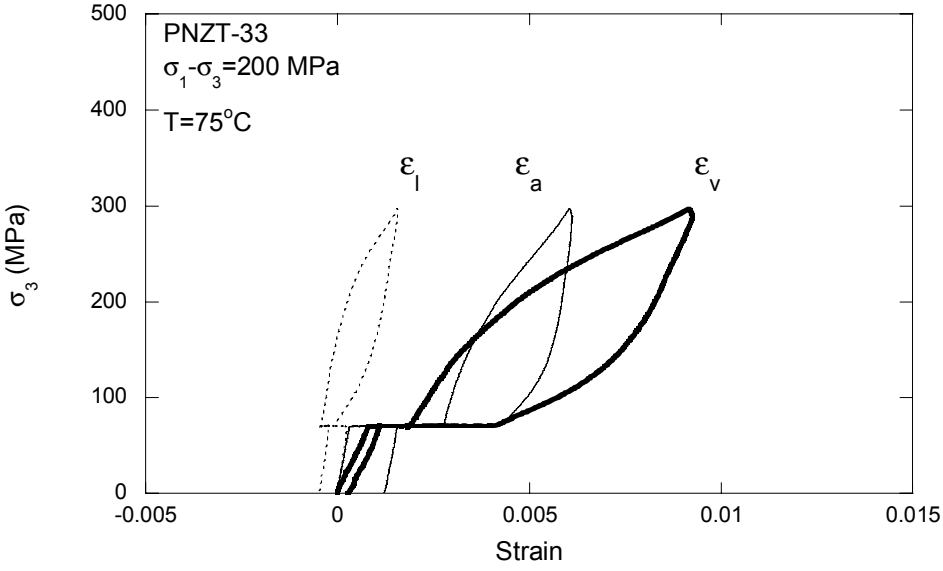
PNZT-33
σ1-σ3=200 MPa
T=75°C
εl
εa
εv
σ3 (MPa)
Strain
-0.005
0
0.005
0.01
0.015

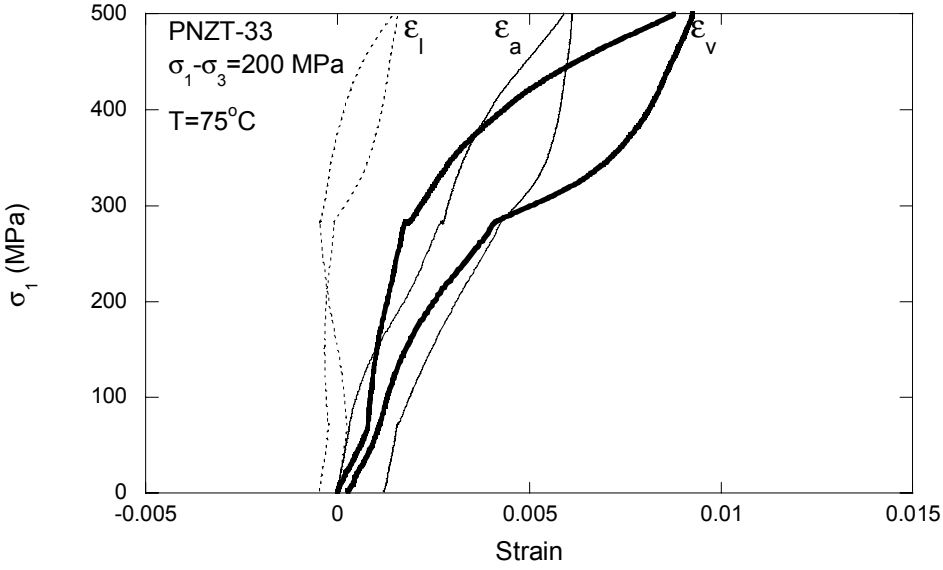
PNZT-33
σ1-σ3=200 MPa
T=75°C
εl
εa
εv
σ1 (MPa)
Strain
-0.005
0
0.005
0.01
0.015

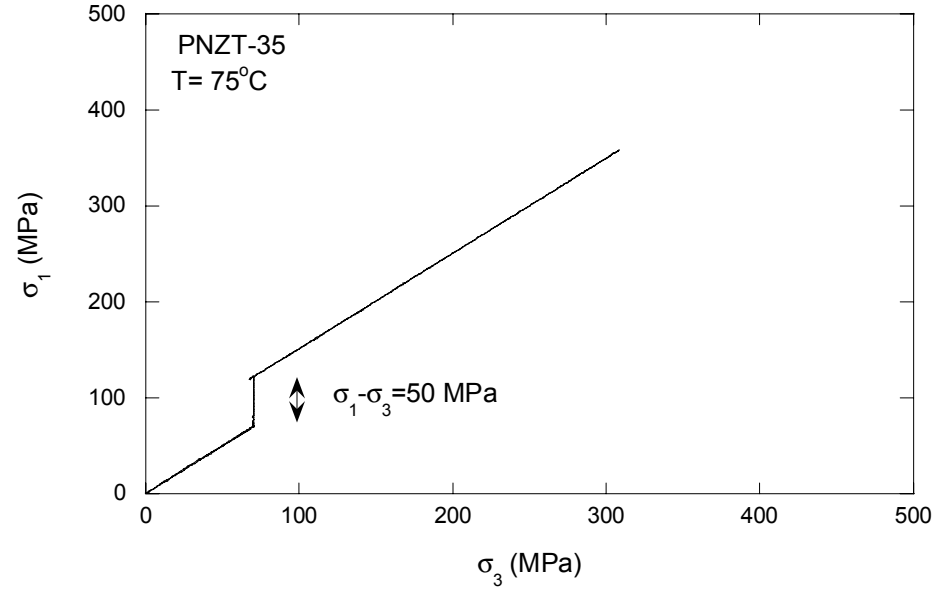
PNZT-35
T= 75°C
σ1-σ3=50 MPa
σ1 (MPa)
σ3 (MPa)
0
100
200
300
400
500

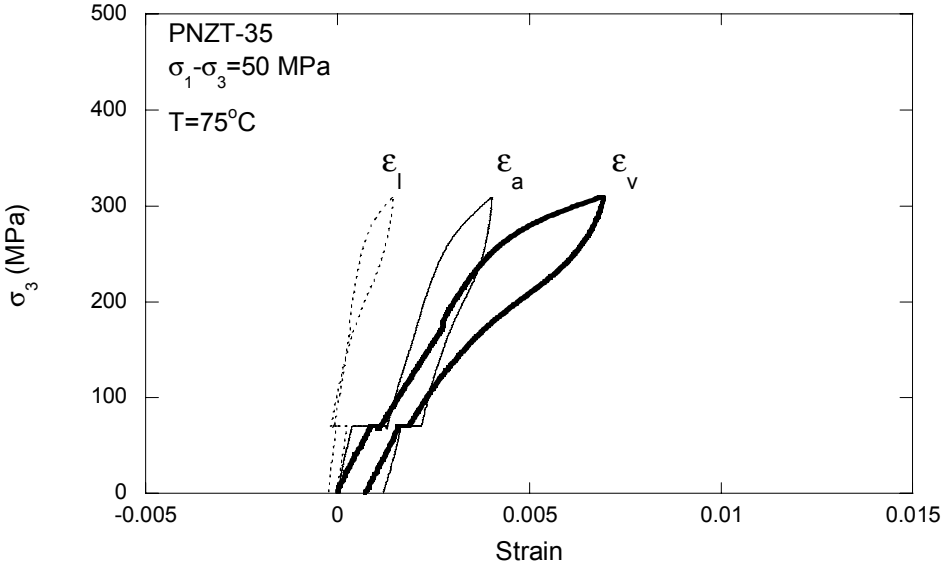
PNZT-35
σ1-σ3=50 MPa
T=75°C
εl
εa
εv
σ3 (MPa)
Strain
-0.005
0
0.005
0.01
0.015

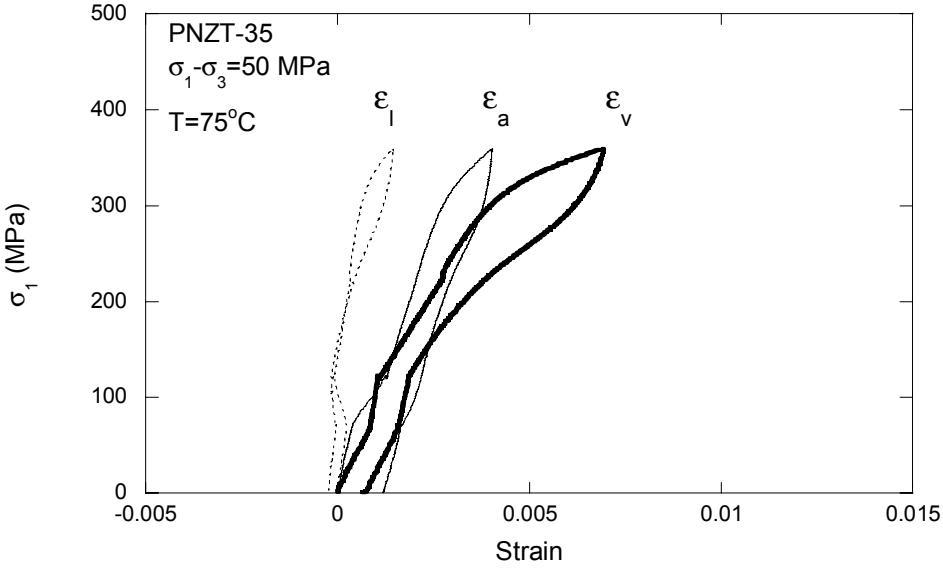
PNZT-35
σ1-σ3=50 MPa
T=75°C
εl
εa
εv
σ1 (MPa)
Strain
-0.005
0
0.005
0.01
0.015

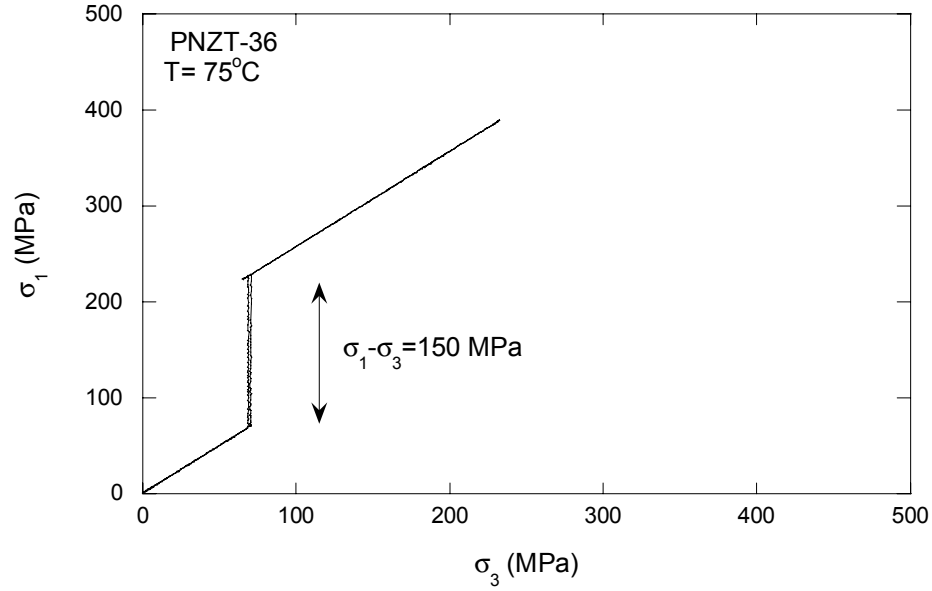
PNZT-36
T= 75°C
σ1-σ3=150 MPa
σ1 (MPa)
σ3 (MPa)
0
100
200
300
400
500

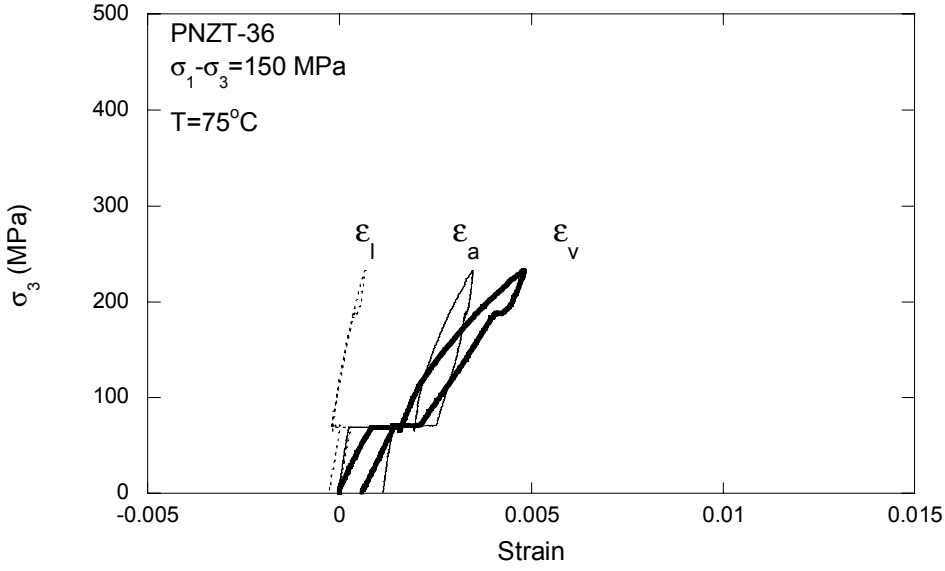
PNZT-36
σ1-σ3=150 MPa
T=75°C
εl
εa
εv
σ3 (MPa)
Strain
-0.005
0
0.005
0.01
0.015

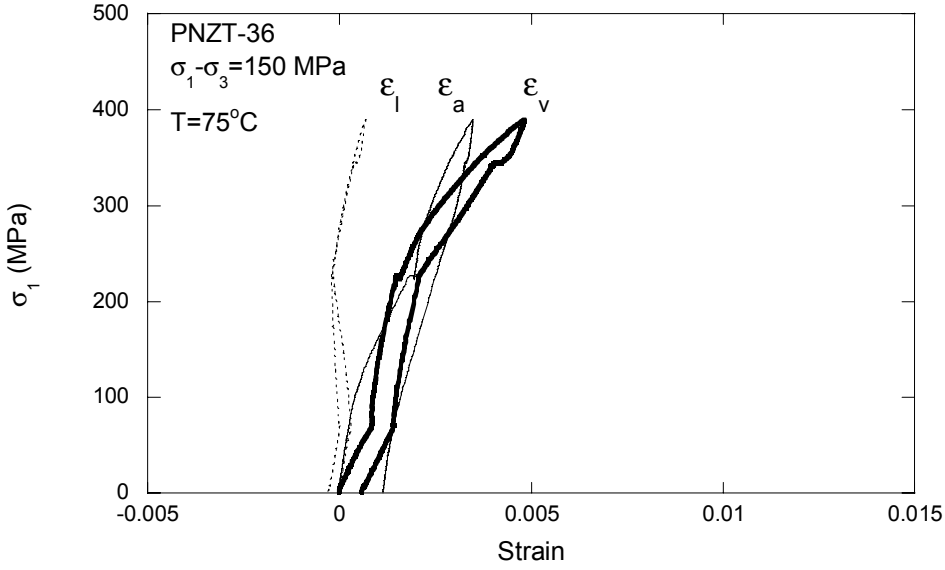
PNZT-36
σ1-σ3=150 MPa
T=75°C
εl
εa
εv
σ1 (MPa)
Strain
-0.005
0
0.005
0.01
0.015

APPENDIX D

List of Data and Supplemental Files Archived in Webfileshare System for PNZT-HF803

List of files archived in the WEBFILESHARE system (https://wfsprod01.sandia.gov).

Folder Name	File Name	Description
/TARGET/PNZT-803	PNZT-SAND03.doc	This SAND report
/TARGET/PNZT-803	PNZT-master.xls	Master data file consists of the following nine worksheets: **HF803**: HF803 lot information **Specimen**: PNZT specimen dimensions **UC-Test matrix**: Test matrix and results for Uniaxial Compression tests **HC-Test matrix**: Test matrix and results for Hydrostatic Compression tests **CSD-Test matrix**: Test matrix and results for Constant Stress Difference tests **UC-data**: Uniaxial compression test data (Time, σ_a, ε_a, ε_l, and ε_v) **UC-P velocity**: Compressive wave velocity data during uniaxial compression tests (Time, σ_a, Input, Output, and Delay time) **HC-data**: Hydrostatic Compression test data (ε_v and Pressure) **CSD-data**: Constant Stress Difference test data (Time, σ_1, σ_3, ε_a, ε_l and ε_v)
/TARGET/PNZT-803	PNZT-ds.zip	Laboratory data sheets for the following tests: PNZT-01, 02, 04, 06, 07, 08, 10, 11, 15, 17, 18, 19, 22, 23, 25, 27, 28, 30, 31, 32, 33, 34, 35, 36, 44, 45, 52, 53, 55, 57, 58, 59, 60, 63, 64, 65 and 71
/TARGET/PNZT-803	PNZT-pic.zip	Miscellaneous pictures taken during constitutive testing of PNZT.

DISTRIBUTION

Sandia National Laboratories
P.O. Box 5800
Albuquerque, NM 87185

1	MS 0512	J. K. Rice, 2500
1	MS 0515	S. G. Barnhart, 2561
1	MS 0515	T. A. Haverlock, 2561
1	MS 0515	J. D. Keck, 2561
1	MS 0515	D. K. Morgan, 2561
1	MS 0515	R. A. Pike, 2561
1	MS 0515	T. W. Scofield, 2561
1	MS 0516	B. H. Cole, 2564
1	MS 0516	S. C. Hwang, 2564
1	MS 0516	R. G. Spulak, 2564
1	MS 0521	F. M. Bacon, 2502
1	MS 0521	R. A. Damerow, 2561
5	MS 0521	S. T. Montgomery, 2561
1	MS 0701	P. J. Davies, 6100
1	MS 0751	R. M. Brannon, 6117
1	MS 0751	L. S. Costin, 6117
1	MS 0751	D. J. Holcomb, 6117
5	MS 0751	M. Y. Lee, 6117
1	MS 0819	J. Robbbins, 9231
3	MS 0824	J. L. Moya, 9130
1	MS 0828	M. Pilch, 9133
1	MS 0834	J. E. Johannes, 9114
1	MS 0841	T. C. Bickel, 9100
1	MS 0889	J. S. Glass, 1843
1	MS 0889	C. S. Watson, 1843
1	MS 0959	S. J. Lockwood, 14192
1	MS 0959	R. H. Moore, 14192
1	MS 0959	P. Yang, 14192
2	MS 1031	J. H. Hofer ,6117
1	MS 1181	L. C. Chhabildas, 1647
1	MS 1181	M. D. Furnish, 1647
1	MS 1186	R. J. Lawrence, 1674
1	MS 1411	H. E. Fang, 1834
1	MS 1411	B. A. Tuttle, 1843
1	MS 1411	V. Tikare, 1834
1	MS 1421	M. U. Anderson, 1122
1	MS 1421	G. A. Samara, 1122
1	MS 1421	R. E. Setchell, 1122

1	MS 9018	Central Tech. Files, 8945-1
2	MS 0899	Technical Library, 9616
2	MS 0731	823/Library, 6850

P.O. Box 808
Livermore, CA 94551

Roger Logan, L-25

Los Alamos National Laboratory
P.O. Box 1663
Los Alamos, NM 87545

Bill Bearden MS F602
Steve Girrens, ESA-EA, P946
Dick Macek MS P946

Kevin C. Greenaugh
Department of Energy/Defense Programs
Director, Division of System Simulation & Validation
1000Independence Ave., SW
Washington DC 20585

Bill-Roy Harrison
Department of Energy/Defense Programs
Program Manager, Weapons Systems Engineering Certification Campaign
19901 Germantown Rd
Germantown, MD 20874

Diane Bird
Weapons Assessments and Development
Supervisory General Engineer
1000 Independence Ave.
NA-115.1
Washington DC 20585